Table 1
Effect of calcination conditions on the variation of crystalline size, tetragonality factor (c/a) and mean lattice strain of PT powders milled for different times

Calcination condition $T/D/R$ (°C/h/°C min^{-1})	Crystallite size (nm)	Lattice strain (%)	Tetragonality factor (c/a)
500/2/30	21.8	0.0188	1.038
550/1/30	19.4	0.0212	1.055
550/2/30	21.6	0.0190	1.052
550/3/30	20.9	0.0197	1.054
600/2/30	21.5	0.0193	1.057

T=calcination temperature.
D=dwell time.
R=heating/cooling rates.

to wear debris from the selected milling process was observed in all calcined powders, indicating the effectiveness of the vibro-milling technique for the production of high purity $PbTiO_3$ nanopowders.

The variation of calculated crystallite size, tetragonality factor (c/a) and lattice strain of the powders milled for different times with the calcination conditions is given in Table 1. In general, it is seen that the crystallite size of lead titanate decreases slightly with increasing calcination temperature for all different milling times, while the calculated values of the tetragonality factor and mean lattice strain progressively increase. However, it should be noted that by increasing the calcination time from 1 to 3 h, these calculated values decrease to the minimum at 2 h and then grow up further after longer dwell time was applied. There is no obvious interpretation of these observations, although it is likely to correspond to the competition between the major mechanisms leading to crystallization and agglomeration [19].

In this connection, a combination of SEM and TEM techniques was also employed for the particle size measurement. The morphological evolution during various calcination conditions of PT powders milled with different times was investigated by SEM technique as shown in Fig. 4. It is seen that all powders seem to have similar morphology. In general, the particles are agglomerated and basically irregular in shape, with a substantial variation in particle sizes, particularly in powders subjected to prolong milling times or high firing temperatures (Fig. 4(c) and (d)). The powders consist of primary particles of nanometers in size. The primary particles have sizes of ~17–57 nm, and the agglomerates measured ~109–157 nm. It is also of interest to point out that averaged particle size tends to increase with calcination temperatures (Fig. 4 and Table 1), in good agreement with other works [8,18]. This observation may be attributed to the occurrence of hard agglomeration with strong inter-particle bond within each aggregates resulting from firing process. The experimental work carried out here suggests that the optimal combination of the milling time and calcination condition for the production of single-phase $PbTiO_3$ powders with smallest particle size (~17 nm) is 25 h and 600 °C for 2 h with heating/cooling rates of 30 °C min^{-1}, respectively. Moreover, the employed heating/cooling rates for $PbTiO_3$ powders observed in this work are also faster than those reported earlier [9,10].

A TEM bright field image of an agglomerated or intergrown particle of the calcined PT powders derived from milling time of 25 h is shown in Fig. 5(a). By employing the selected area electron diffraction (SAED) technique, a perovskite-like phase of tetragonal *P4/mmm* $PbTiO_3$ is identified (Fig. 5(b)), in good agreement with the XRD analysis and the data in JCPDS file no. 6-452 [13]. The reciprocal lattice pattern of this PT phase was also simulated with the Carine Crytallography 3.0 software, as demonstrated in Fig. 5(c). In addition,

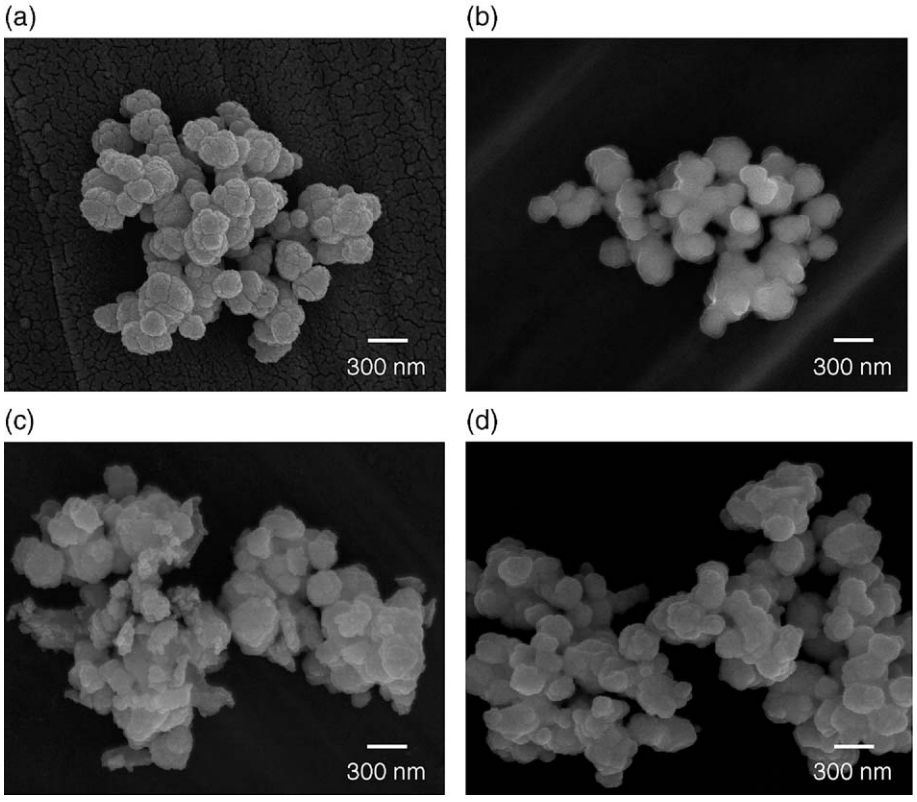

Fig. 4. SEM micrographs of PT powders milled for (a) 20 h and (b) 25 h, and calcined at 600 °C for 2h, (c) 25 h and (d) 30 h, and calcined at 550 °C for 3 h, with heating/cooling rates of 30 °C/min.

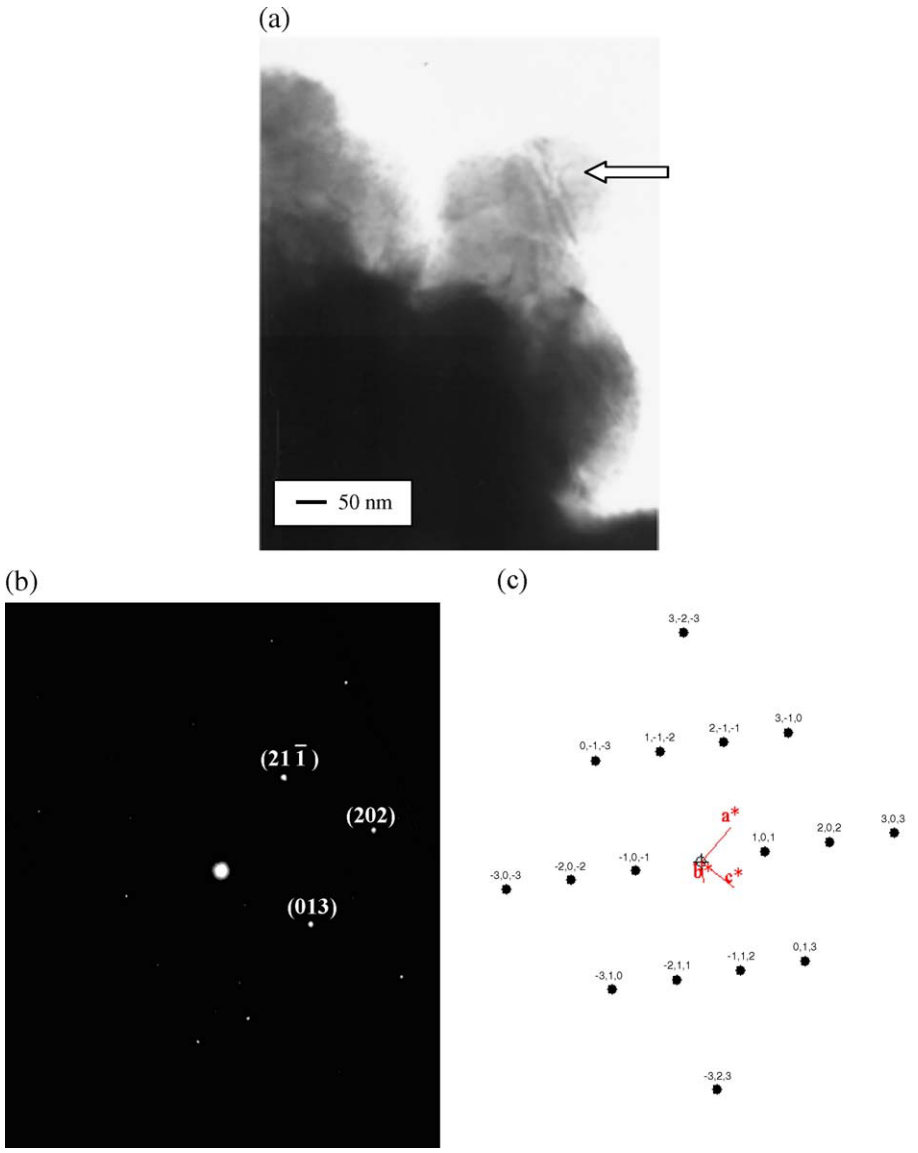

Fig. 5. (a) TEM micrograph, (b) SAED pattern ([13 $\bar{1}$] zone axis) and (c) reciprocal lattice pattern simulation of PT powders milled for 25 h and calcined at 600 °C for 2 h with heating/cooling rates of 30 °C/min.

EDX analysis using a 20 nm probe on a large number of particles of these calcined $PbTiO_3$ powders confirmed the existence of single phase perovskite, in good agreement with XRD results.

4. Conclusion

This work demonstrated that by applying an appropriate choice of the vibro-milling time, calcination temperature and dwell time, mass quantities of a high purity lead titanate nanopowders can be successfully produced by a simple solid-state mixed oxide synthetic route without the use of high purity starting precursors.

Acknowledgement

This work was supported by the Thailand Research Fund (TRF), the Faculty of Science and the Graduate School of Chiang Mai University.

References

[1] A.J. Moulson, J.M. Herbert, Electroceramics, 2nd ed., Wiley, Chichester, 2003.
[2] B. Jaffe, W.R. Cook, H. Jaffe, Piezoelectric Ceramics, Academic Press, New York, 1971.
[3] G.H. Haertling, J. Am. Ceram. Soc. 82 (1999) 797.
[4] K. Uchino, Piezoelectrics and Ultrasonic Applications, Kluwer, Deventer, 1998.
[5] J.S. Wright, L.F. Francis, J. Mater. Res. 8 (1993) 1712.
[6] G.R. Fox, J.H. Adair, R.E. Newnham, J. Mater. Sci. 25 (1990) 3634.
[7] V.V. Dabhade, T.R. Rama Mohan, P. Ramakrishman, Appl. Surf. Sci. 182 (2001) 390.
[8] S. Ananta, Mater. Lett. 58 (2004) 2781.
[9] A. Udomporn, S. Ananta, Curr. Appl. Phys. 4 (2004) 186.
[10] A. Udomporn, S. Ananta, Mater. Lett. 58 (2003) 1154.
[11] R. Wongmaneerung, R. Yimnirun, S. Ananta, Mater. Lett. (in press), doi:10.1016/j.matlet.2005.11.043.
[12] H. Klug, L. Alexander, X-ray Diffraction Procedures for Polycrystalline and Amorphous Materials, 2nd ed., Wiley, New York, 1974.

[13] JCPDS-ICDD Card no. 6-452, International Centre for Diffraction Data, Newtown Square, PA, 2000.
[14] C.G. Pillai, P.V. Ravindron, Thermochim. Acta 66 (1996) 109.
[15] J. Tartaj, C. Moure, L. Lascano, P. Duran, Mater. Res. Bull. 36 (2001) 2301.
[16] M.L. Calzada, M. Alguero, L. Pardo, J. Sol-Gel Sci. Technol. 13 (1998) 837.
[17] JCPDS-ICDD Card no. 6-452, International Centre for Diffraction Data, Newtown Square, PA, 2000.
[18] S. Ananta, R. Tipakontitikul, T. Tunkasiri, Mater. Lett. 57 (2003) 2637.
[19] S. Ananta, R. Brydson, N.W. Thomas, Mater. J. Eur. Ceram. Soc. 20 (2000) 2315.

International Journal of Modern Physics B
Vol. 20, No. 17 (2006) 2415–2424

World Scientific
www.worldscientific.com

EFFECT OF SINTERING TEMPERATURE ON DENSIFICATION AND DIELECTRIC PROPERTIES OF $Pb(Zr_{0.44}Ti_{0.56})O_3$ CERAMICS

R. YIMNIRUN*, R. TIPAKONTITIKUL and S. ANANTA

Department of Physics, Faculty of Science, Chiang Mai University, Chiang Mai, 50200, Thailand
**rattikornyimnirun@yahoo.com*

Received 31 October 2005

In this study, lead zirconate titanate ($Pb(Zr_{0.44}Ti_{0.56})O_3$) ceramics were fabricated with a mixed oxide synthetic route of lead oxide (PbO) and zirconium titanate ($ZrTiO_4$) precursors. The effects of sintering temperature on phase formation, densification and dielectric responses of the ceramics have been investigated using XRD, SEM, EDX and dielectric measurement techniques. The densification of the PZT ceramics with density of 97% theoretical density can be achieved with appropriate sintering condition without any sintering additives. The optimized sintering condition has been identified as 1225°C for 4 h. More importantly, the dielectric properties are found to improve with increasing sintering temperature and grain size. However, when sintered over 1250°C, the dielectric properties of the ceramics are seen to deteriorate as a result of PbO vaporization, ZrO_2 segregations and porosity.

Keywords: Lead zirconate titanate; PZT; sintering; densification; dielectric properties.

1. Introduction

Lead zirconate titanate ceramics, $Pb(Zr_xTi_{1-x})O_3$ or PZT, have been widely investigated on their electrical properties for several decades.[1] As a prototype of piezoelectrics, PZT ceramics exhibit good dielectric and piezoelectric properties, especially the compositions near the morphotropic phase boundary (MPB). Therefore, they have been exploited in several commercial applications such as ultrasonics, buzzers, actuators and transducers.[2,3] In addition, the compositions in the vicinity of MPB, generally identified as 52/48 for Zr/Ti ratio, have also been extensively investigated.[1,3,4] This is clearly a result of enhanced properties of the compositions, which have been attributed to the coexistence of tetragonal and rhombohedral phases.[4,5] More recently, the reports by Noheda *et al.* have also identified that the presence of the monoclinic distortion is the origin of the unusually high piezoelectric response of PZT compositions near the MPB.[6,7]

*Corresponding author.

The stoichiometry and densification behavior of the oxide ceramics, which are greatly influenced by sintering conditions, are known to be the key factors for ensuring good electrical properties.[4] PZT compositions are commonly sintered at high temperatures in the range 1100–1300°C. This creates problems with vaporization of PbO during sintering and possible lead deficiency which may cause segregation of a ZrO_2 phase or a formation of unwanted phases.[8] This may affect the electrical properties of the material. The B-site precursor method is one the techniques developed to counteract the problem.[9] In this method, the high temperature phase of $ZrTiO_4$ is first formed before reacting with PbO to form PZT at lower temperature. Furthermore, the microstructure features such as grain size, grain boundary, density, porosity, and homogeneity markedly influence the electrical characteristics of sintered piezoelectric ceramics.[10] Kakegawa *et al.*[11] reported that the dielectric constant of PZT ceramics depends on their chemical compositions. The room temperature dielectric constant of PZT ceramics was found to decrease with increasing grain size, while, on the other hand, the maximum dielectric constant of $Pb(Zr_{0.52}Ti_{0.48})O_3$ ceramics increased as the grain size decreased.[12] Generally, the grain size of PZT ceramics increases with the sintering temperature and dwell time.[13,14] Therefore, it could be intuitively expected that the electrical properties of the PZT ceramics would be greatly influenced by the sintering parameters. In this study, the effects of sintering temperature on the densification and the dielectric properties of the sintered PZT ceramics prepared by the B-site precursor method were investigated. In stead of the typical MPB composition of $Pb(Zr_{0.52}Ti_{0.48})O_3$, which have been extensively studied,[1,3,4,12] the tetragonal composition of $Pb(Zr_{0.44}Ti_{0.56})O_3$ was chosen in this study. This would extend an understanding on the processing-composition-properties relationships in PZT ceramics.

2. Materials and Methods

PZT powders were synthesized by a modified two-stage mixed oxide route. The $ZrTiO_4$ precursor powders were mixed with PbO for 24 h and calcined at 800°C for 2 h, as reported earlier.[9] Ceramic fabrication was achieved by adding 3 wt% polyvinyl alcohol (PVA) binder, then uniaxially pressed to form a green pellet of 10 mm diameter and 2 mm thick. The pellets were placed inside a closed alumina crucible covered with lead zirconate ($PbZrO_3$) powder to compensate the PbO volatilization and then sintered at various temperatures for 4 h with constant heating/cooling rates of 10°C/min. During the heating, the temperature was maintained at 500°C for 2 h to burn out the PVA binder. The pellets were subjected to bulk densities measurement with Archimedes method.

Finally, the XRD, SEM and dielectric properties measurement were carried out. X-ray diffraction analysis of the sintered samples was carried out at room temperature using CuKα radiation (40 kV) on X′ Pert X-ray diffractometer. Scanning electron microscopy (JEOL, JSM5910LV) was employed and the average grain size

(Φ_{av}) of samples was determined using the linear interception method. For electrical measurement, the as-sintered samples were polished to parallel surfaces. The major faces of the samples were coated with conductive Pt paint, and then heat cured at 700°C for 1 h to ensure that the electrodes were completely adhered to the ceramic. The dielectric properties were monitored as a function of temperatures (25–400°C) at a measuring frequency of 1 kHz using a computer controlled impedance analyzer (HP Model 4284A).

3. Results and Discussion

The densification of the PZT at various sintering temperatures is investigated. The change in density versus the sintering temperature (1100–1320°C) is shown in Fig. 1. In the sintering temperature range of 1100–1250°C, the density increases with increasing temperature. Further increase in the sintering temperature to 1320°C leads to the decrease of the density. This feature creates a maximum density value of about 97% of theoretical density which is comparable to the value reported by Wang *et al.*[15] where Li_2CO_3, Bi_2O_3 and CuO were used as sintering aids. The increasing density with rising sintering temperature up to 1250°C may be explained by the enhanced densification as the sintering of PZT is normally found at 1200°C.[16] Further increase in the sintering temperature causes a decrease in density values. This may be attributed to the loss of lead oxide at high sintering temperatures, which is similar to the results found in other Pb-based perovskite systems.[17,18]

XRD patterns of PZT ceramics sintered at various temperatures are plotted in Fig. 2. The strongest reflections in the majority of the XRD patterns can be identified as the perovskite phase of the composition $Pb(Zr_{0.44}Ti_{0.56})O_3$, which could be matched with JCPDS file 50-346. To a first approximation, this phase has a tetragonal perovskite-type structure in space group *P4mm* (No. 99), with cell

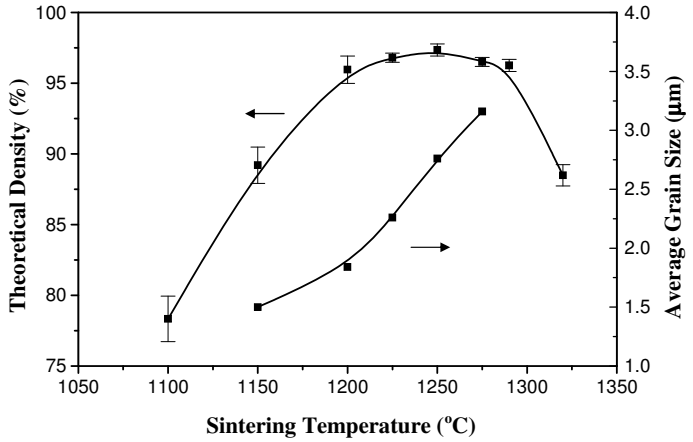

Fig. 1. Variation of density and grain size with sintering temperature for the PZT ceramics.

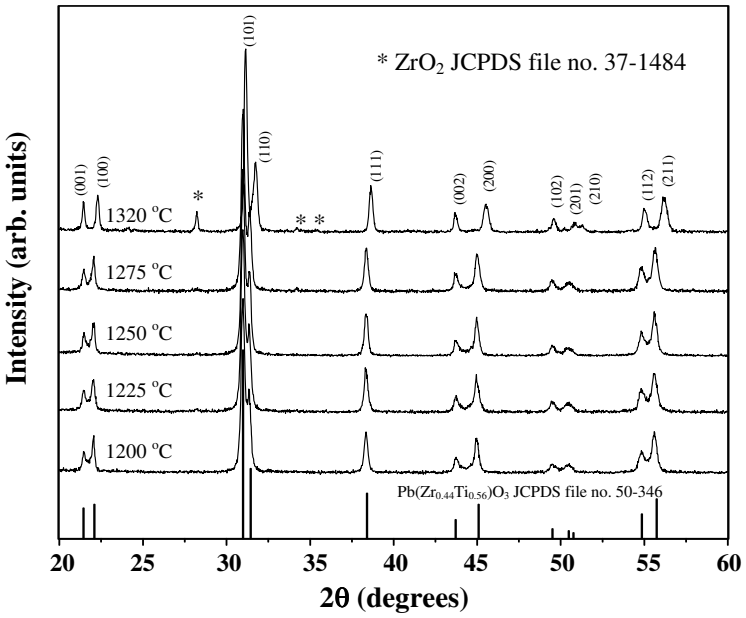

Fig. 2. XRD patterns of the PZT ceramics sintered at various temperatures.

parameters $a = 401$ pm and $c = 414$ pm, respectively.[19] However, for the sample sintered at 1320°C, some additional reflections (marked by $*$) are observed, and these can be identified as presence of ZrO_2 (JCPDS file 37-1484). This phase has a monoclinic structure with cell parameters $a = 531.2$, $b = 521.2$, $c = 514.7$ pm and $\beta = 99.218°$ in space group $P21/a$ (No. 14).[20] Due to no trace of ZrO_2 has been observed for the samples sintered at the temperatures below 1320°C, it is believed that the consequence of PbO evaporation is an apparently favorable factor in facilitating the occurrence of ZrO_2 at a higher sintering temperature.[21,22]

Microstructure development was investigated by scanning electron microscopy (SEM). Free surface micrographs of PZT ceramics sintered at various temperatures from 1150–1320°C are shown in Fig. 3. Also depicted in Fig. 1, the results indicate that grain size tends to increase with sintering temperatures in the temperature range 1150–1275°C that sees the grain size of the samples changed from 1.5 to 3.2 μm, in agreement with a previous work by Hong *et al.*[23] Similar findings were also reported in Nb-doped PZT and modified PT ceramics.[24,25] However, the average grain size of PZT sintered at 1320°C cannot be determined from SEM micrograph because of the ZrO_2 segregations that are confirmed by XRD results shown in Fig. 2, which also displays very high degree of porosity. In addition to the PbO evaporation, the presence of ZrO_2 segregations and a porous microstructure is believed to be another cause for the decrease in the ceramic density at high sintering temperature. As will be discussed later, these factors are also responsible for the dielectric behavior of the PZT ceramics.

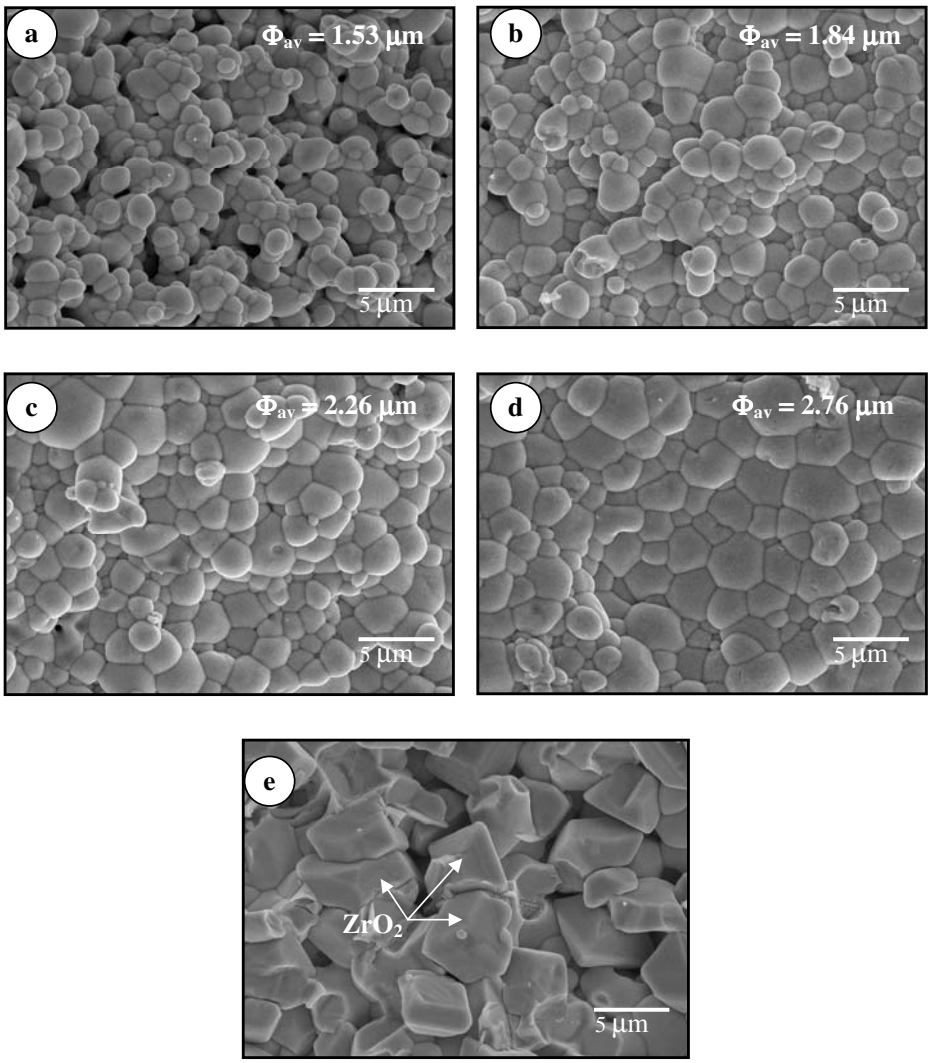

Fig. 3. SEM micrographs of the PZT ceramics sintered at (a) 1150°C, (b) 1200°C, (c) 1225°C, (d) 1250°C and (e) 1320°C.

The variations of dielectric constant (ε_r) and dissipation factor at 1 kHz with sintering temperature are shown in Fig. 4. For all samples in the present work, the Curie temperature is seen independent of the sintering temperature. Similar results have also been reported by other workers.[26,27] The results in Fig. 4 clearly indicate that the dielectric properties of the PZT ceramics depend on the sintering temperature. As listed in Table 1, the maximum value of dielectric constant ($\varepsilon_{r,\max}$) measured at T_C increases from 8250 to 18984 as the sintering temperature increases from 1150–1225°C. Further increase in the sintering temperature to 1275°C results

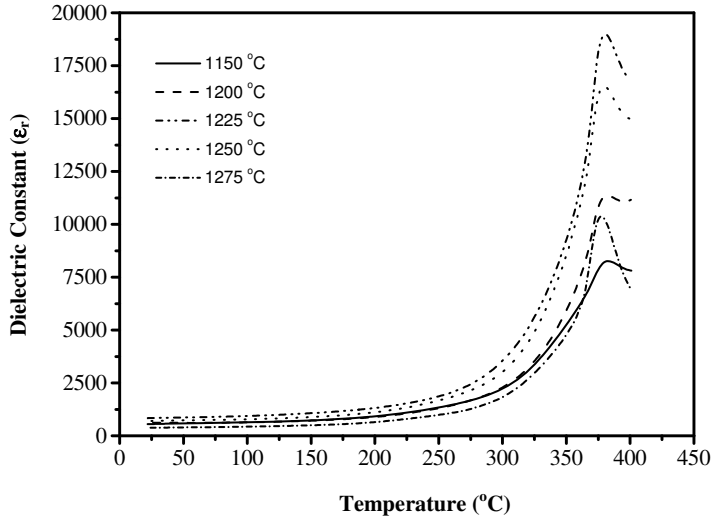

(a)

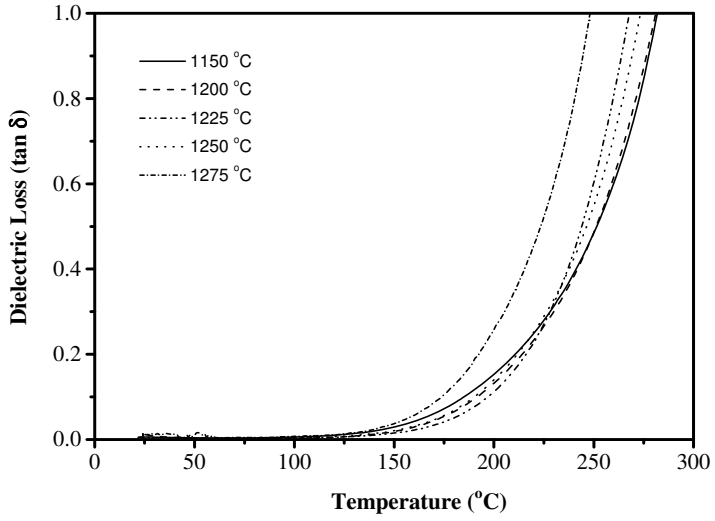

(b)

Fig. 4. Temperature dependence of (a) dielectric constant and (b) dissipation factors at 1 kHz for the PZT ceramics sintered at various temperatures.

in a drop in the values of $\varepsilon_{r,\max.}$ to 10378. The opposing trend is observed in the values of the high temperature dielectric loss (tan δ). It should also be noted here that since the dielectric loss in all ceramics increases significantly at high temperature as a result of thermally activated space charge conduction,[28] the values of the high temperature dielectric loss (tan δ) determined at 200°C are listed for comparison. As also listed in Table 1, the similar tendency is also observed for the

Table 1. Physical and dielectric properties of PZT ceramics sintered at various temperatures.

Sintering temperature (°C)	Average grain size (μm)	T_c (°C)	Dielectric Properties at 1 kHz			
			ε_r (25°C)	tan δ (25°C)	$\varepsilon_{r,\max}$ (T_C)	tan δ (200°C)
1150	1.53	381	564	0.0072	8250	0.160
1200	1.84	385	638	0.0039	11316	0.145
1225	2.26	380	697	0.0038	18984	0.120
1250	2.76	379	463	0.0042	16524	0.150
1275	3.16	377	397	0.0047	10378	0.265

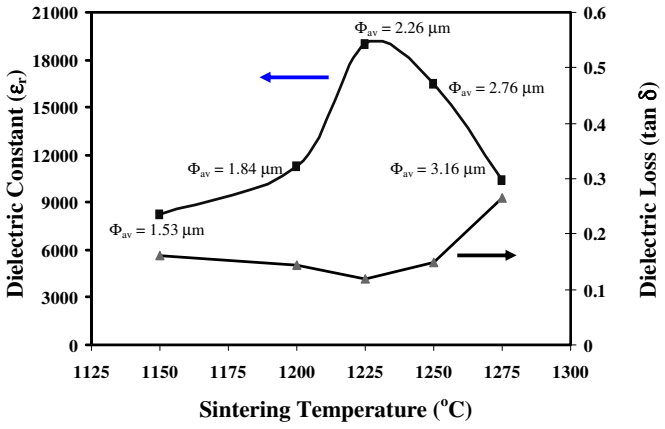

(a)

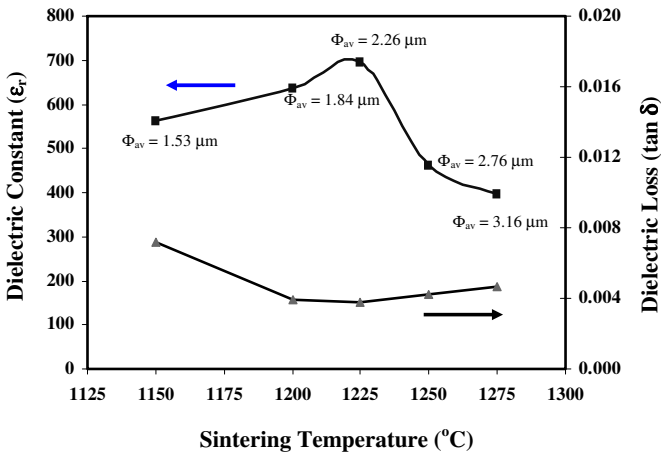

(b)

Fig. 5. Variation of (a) maximum dielectric properties and (b) room temperature dielectric properties with sintering temperature for the PZT ceramics.

room temperature dielectric properties. Figure 5 clearly depicts the relationship between the dielectric properties and the sintering temperature. In addition, it is worth noting that the measured values of the dielectric properties in the present work are in good agreement with the previous works on PZT ceramics prepared by different processing techniques.[12,29–31]

By comparing Figs. 1 and 5, the tendency of ε_r values with the sintering temperature is similar to that of density, in good agreement with the report by Kong and Ma,[31] while the average grain size also increases monotonically with sintering temperatures. Earlier report by Chu *et al.*[25] also showed similar observations in Nb-doped PZT ceramics. Clearly, the increasing dielectric constant (both at room and Curie temperatures) is due to the increasing density of the ceramics. However, the decreasing room temperature dielectric constant as sintering temperature above 1225°C can be related to the increasing grain size. Kang *et al.*[32] reported that the room temperature dielectric constant decreased with the increasing grain size. Similar results were also reported for $BaTiO_3$, modified PT and PLZT ceramics.[24,32,33] On the other hand, an earlier report by Okazaki *et al.*[34] showed that the maximum dielectric constant of PZT ceramics increased with increasing grain size. This is probably because increasing grain size results in reduction of the volume fraction of grain boundaries. The coupling effect between the grain boundaries and the domain wall, which makes domain reorientation more difficult and severely constrains the domain wall motion, is then decreased. This translates to an increase in the domain wall mobility corresponding to an increase in dielectric constant.[12,23,35] In this study, an initial increase of the maximum dielectric constant with the sintering temperature up to 1225°C, as shown in Fig. 5, can be related to the increasing grain size. However, the maximum dielectric constant values of the sintered samples then decrease from 18984 to 10378 as the sintering temperature is increased to 1275°C. This observation may be attributed to microstructure inhomogeneity of the PZT ceramics as a result of PbO deficiency, ZrO_2 precipitation, and porosity at higher sintering temperature. Thus, the higher sintering temperature and the presence of ZrO_2 impurity can significantly reduce the values of the dielectric constant of the PZT ceramics. Finally, it should be emphasized that even though many earlier studies have established a relationship between the dielectric properties and grain size in PZT as well as other perovskite ceramics, this study has shown that other factors such as the sintering conditions, the presence of pores, ZrO_2 and other secondary phases, chemical homogeneity, and Zr/Ti ratio clearly have strong influence on the dielectric properties of the PZT ceramics.

4. Conclusions

$Pb(Zr_{0.44}Ti_{0.56})O_3$ ceramics were successfully fabricated by employing the modified two-stage mixed oxide route and the effects of the sintering temperature on the densification and dielectric properties were investigated. High density PZT ceramics were obtained for the sintering temperatures about 1200–1250°C. The dielectric

properties of the PZT ceramics are dependent on sintering temperature. It is clear that the dielectric constant increases with increasing sintering temperature and grain size. However, the increasing trends between the density and dielectric properties and the sintering temperature are interrupted when the ceramics are sintered above 1250°C as a result of PbO vaporization, ZrO_2 segregation and porosity.

Acknowledgment

The authors would like to express their gratitude for financial support from the Thailand Research Fund (TRF) and Faculty of Science, Chiang Mai University.

References

1. G. H. Haertling, *J. Am. Ceram. Soc.* **82**(4), 797 (1999).
2. L. E. Cross, *Mater. Chem. Phys.* **43**, 108 (1996).
3. A. J. Moulson and J. M. Herbert, *Electroceramics*, 2nd edn. (Wiley-Interscience, New York, 2003).
4. B. Jaffe, W. R. Cook and H. Jaffe, *Piezoelectric Ceramics* (Academic Press, New York, 1971).
5. R. Guo, L. E. Cross, S.-E. Park, B. Noheda, D. E. Cox and G. Shirane, *Phys. Rev. Lett.* **84**(23), 5423 (2000).
6. B. Noheda, J. A. Gonzalo, L. E. Cross, R. Guo, S.-E. Park, D. E. Cox and G. Shirane, *Phys. Rev. B.* **61**(13), 8687 (2000).
7. B. Noheda, D. E. Cox, G. Shirane, J. A. Gonzalo, L. E. Cross and S.-E. Park, *Appl. Phys. Lett.* **74**(14), 2059 (1999).
8. B. V. Hiremath, A. I. Kingon and J. V. Biggers, *J. Am. Ceram. Soc.* **66**(11), 790 (1983).
9. R. Tipakontitikul and S. Ananta, *Mater. Lett.* **58**, 449 (2004).
10. Y. Xu, *Ferroelectric Materials and Their Applications* (Elsevier Science, Amsterdam, 1991).
11. K. Kakegawa, J. Mohri, T. Takahashi, H. Yamamura and S. Shirasaki, *Solid State Commun.* **24**, 769 (1977).
12. B. M. Jin, J. Kim and S. C. Kim, *Appl. Phys. A-Mater.* **65**, 53 (1997).
13. A. Garg and D. C. Agrawal, *Mat. Sci. Eng. B-Solid.* **56**, 46 (1999).
14. E. K. Goo, R. K. Mishra and G. Thomas, *J. Am. Ceram. Soc.* **64**(6), 517 (1981).
15. X. X. Wang, K. Murakami, O. Sugiyama and S. Kaneko, *J. Eur. Ceram. Soc.* **21**, 1367 (2001).
16. A. Megriche and M. Troccaz, *Mater. Res. Bull.* **33**, 569 (1998).
17. E. R. Nielsen, E. Ringgaard and M. Kosec, *J. Eur. Ceram. Soc.* **22**, 1847 (2002).
18. A. Boutarfaia, *Ceram. Inter.* **26**, 583 (2000).
19. Powder diffraction File no. 50-346. International Centre for Diffraction Data, Newton Square, PA, 2000.
20. Powder diffraction File no. 37-1484. International Centre for Diffraction Data, Newton Square, PA, 2000.
21. S. Fushimi and T. Ikeda, *J. Am. Ceram. Soc.* **50**, 129 (1967).
22. Z. Branković, G. Branković and J. A. Varela, *J. Mater. Sci.* **14**, 37 (2003).
23. Y.-S. Hong, H.-B. Park and S.-J. Kim, *J. Eur. Ceram. Soc.* **18**, 613 (1998).
24. T. Y. Chen, S. Y. Chu and Y. D. Juang, *Sensor. Actuat. A-Phys.* **102**, 6 (2002).
25. S. Y. Chu, T. Y. Chen and I. T. Tsai, *Integr. Ferroelectr.* **58**, 1293 (2003).

26. L. B. Kong, W. Zhu and O. K. Tan, *Mater. Lett.* **42**, 232 (2000).
27. G. Fantozzi, A. Bouzid, E. M. Bourim and M. Gabbay, *J. Eur. Ceram. Soc.* **25**(13), 3213 (2005).
28. R. Yimnirun, S. Ananta and P. Laoratanakul, *Mat. Sci. Eng. B-Solid.* **112**, 79 (2004).
29. H. Ouchi, M. Nishida and S. Hayakawa, *J. Am. Ceram. Soc.* **49**(11), 577 (1966).
30. E. R. Nielsen, E. Ringgaard and M. Kosec, *J. Eur. Ceram. Soc.* **22**, 1847 (2002).
31. L. B. Kong and J. Ma, *Mater. Lett.* **51**, 95 (2001).
32. B. S. Kang, G. C. Dong and S. K. Choi, *J. Mater. Sci. Lett.* **9**, 139 (1998).
33. K. Kinoshita and A. Yamaji, *J. Appl. Phys.* **47**(1), 371 (1976).
34. K. Okazaki and K. Nagata, *J. Electron. Commun. Soc. Jpn. C.* **53**, 815 (1970).
35. P. Ravindranathan, S. Komarneni, A. S. Bhalla and R. Roy, *J. Am. Ceram. Soc.* **74**, 2996 (1991).

ELSEVIER

Materials Science and Engineering B 132 (2006) 292–299

MATERIALS SCIENCE & ENGINEERING B

www.elsevier.com/locate/mseb

Effects of magnesium niobate precursor and calcination condition on phase formation and morphology of lead magnesium niobate powders

R. Wongmaneerung [a], T. Sarakonsri [b], R. Yimnirun [a], S. Ananta [a,*]

[a] *Department of Physics, Faculty of Science, Chiang Mai University, Chiang Mai 50200, Thailand*
[b] *Department of Chemistry, Faculty of Science, Chiang Mai University, Chiang Mai 50200, Thailand*

Received 1 March 2006; received in revised form 26 April 2006; accepted 28 April 2006

Abstract

A perovskite phase of lead magnesium niobate, $Pb(Mg_{1/3}Nb_{2/3})O_3$ or PMN, powders has been synthesized by a rapid vibro-milling technique. Both columbite $MgNb_2O_6$ and corundum $Mg_4Nb_2O_9$ have been employed as magnesium niobate precursors, with the formation of the PMN phase investigated as a function of calcination conditions by thermal gravimetric and differential thermal analysis (TG–DTA) and X-ray diffraction (XRD). The particle size distribution of the calcined powders was determined by laser diffraction technique. Morphology, crystal structure and phase composition have been determined via a combination of scanning electron microscopy (SEM), transmission electron microscopy (TEM) and energy-dispersive X-ray (EDX) techniques. The magnesium niobate precursor and calcination condition have been found to have a pronounced effect on the phase and morphology evolution of the calcined PMN powders. It is seen that optimisation of calcination conditions can lead to a single-phase PMN in both methods. However, the formation temperature and dwell time for single-phase PMN powders were lower for the synthetic method employing a columbite $MgNb_2O_6$ precursor.

Keywords: Lead magnesium niobate; Magnesium niobate; Perovskite; Powder synthesis; Calcination

1. Introduction

Lead magnesium niobate, $Pb(Mg_{1/3}Nb_{2/3})O_3$ or PMN, is one of the most widely investigated relaxor ferroelectric materials with a perovskite structure. The excellent dielectric broadening and electrostrictive properties make it a promising electroceramic material for capacitor, electrostrictive actuator, electromechanical transducer and electro-optic applications [1–3]. There has been a great deal of interest in the preparation of single-phase PMN powders as well as in the sintering and dielectric properties of PMN-based ceramics [4–6]. However, it is well documented that the formation of PMN perovskite via the solid-state reaction is often accompanied by the occurrence of unwanted pyrochlore-type phases because of the volatilisation of PbO, the low dispersion of MgO and the differences of the reactive temperature between Pb–Nb and Pb–Mg [7–9]. Hence, several innovation techniques [10–12] have been utilized to minimize the amount of pyrochlore phase formed.

The initial work of Lejeune and Boilot [10] considered the many parameters which influence the synthesis of PMN from PbO, MgO and Nb_2O_5 precursors, concluding that the formation of a pyrochlore phase could not be completely eliminated. Moreover, it was proposed that the reactivity of magnesium oxide with lead and niobium oxides was the definitive factor governing products of the reaction. These authors later proposed the use of $MgCO_3$ in place of MgO to increase the yield of perovskite PMN. Swartz and Shrout [7] developed an effective way of producing PMN powder in high yield by the introduction of a two-step process (the B-site precursor approach). In the method, an intermediate step to give columbite-type $MgNb_2O_6$ precursor is used to bypass the formation of the pyrochlore phases. Alternatively, Joy and Sreedhar [11] proposed the use of $Mg_4Nb_2O_9$ precursor in place of $MgNb_2O_6$ for the fabrication of pyrochlore-free PMN. More recently, Lu and Yang [12] adopted a two-stage synthesis method by precalcining the mixture of MgO and Nb_2O_5 at 1000 °C to form $Mg_4Nb_2O_9$. This compound was then quenched at 850–900 °C with PbO to form PMN without further soaking. This approach yielded perovskite PMN as the dominant phase, with pyrochlore impurities of less than 5% and some residual MgO. It was also claimed that the pyrochlore

* Corresponding author. Tel.: +66 53 943367; fax: +66 53 943445.
E-mail address: suponananta@yahoo.com (S. Ananta).

0921-5107/$ – see front matter © 2006 Elsevier B.V. All rights reserved.
doi:10.1016/j.mseb.2006.04.034

phases and the residual MgO could be eliminated completely with the introduction of excess PbO and nitric acid, respectively. However, the preparation of PMN using $Mg_4Nb_2O_9$ precursor, to date, has not been extensive as that of PMN using $MgNb_2O_6$ precursor. Moreover, its effect on the formation of perovskite PMN phase under various calcination conditions (especially the effects of applied dwell time and heating/cooling rates) has not been adequately characterized.

The purpose of this study was to compare the two B-site precursor synthetic routes of PMN formation and the characteristics of the resulting powders. The phase formation and morphology of the powders calcined at various conditions will be studied and discussed.

2. Experimental procedure

$Pb(Mg_{1/3}Nb_{2/3})O_3$ was synthesised by a similar methodology of B-site precursor mixed oxide synthetic route, as reported earlier [4]. Starting precursors were as follows: PbO (JCPDS file number 77-1971), MgO (periclase: JCPDS file number 71-1176) and Nb_2O_5 (JCPDS file number 80-2493) (Aldrich, 99% purity). These three oxide powders exhibited an average particle size in the range of 3.0–5.0 μm. First, two intermediate phases of magnesium niobate: $MgNb_2O_6$ and $Mg_4Nb_2O_9$ were separately prepared by the solid-state reaction method previously reported [13,14], employing an optimised calcination conditions of 1000 °C for 4 h with heating/cooling rates of 30 °C/min and 950 °C for 2 h with heating/cooling rates of 25 °C/min, respectively. The following reaction sequences were then proposed for the formation of PMN:

1. The columbite route:

$$3PbO(s) + MgNb_2O_6(s) \rightarrow 3Pb(Mg_{1/3}Nb_{2/3})O_3(s) \quad (1)$$

2. The corundum route:

$$12PbO(s) + Mg_4Nb_2O_9(s) + 3Nb_2O_5(s) \rightarrow 12Pb(Mg_{1/3}Nb_{2/3})O_3(s) \quad (2)$$

Instead of employing a ball-milling procedure (ZrO_2 media under acetone for 24 h [7]), a McCrone vibro-milling was used. In order to improve the reactivity of the constituents, the milling process was carried for 2 h (instead of 30 min [4]) with corundum media in isoproponal. After drying at 120 °C for 2 h, various calcination conditions were applied in order to investigate the formation of PMN phase in each calcined powders.

The reactions of the uncalcined powders taking place during heat treatment were investigated by thermal gravimetric and differential thermal analysis (TG–DTA, Shimadzu) using a heating rate of 10 °C/min in air from room temperature up to 900 °C. Calcined powders were subsequently examined by room temperature X-ray diffraction (XRD; Philips PW 1729 diffractometer) using Ni-filtered Cu Kα radiation, to identify the phases formed and optimum calcination conditions for the manufacture of PMN powders. The mean crystallite size was determined using the diffraction peak (1 1 0) of the perovskite pattern by using Scherrer equation [15]. Particle size distributions of powders were determined by laser diffraction technique (DIAS 1640 laser diffraction spectrometer), with the grain size and morphologies of powders observed by scanning electron microscopy (SEM; JEOL JSM-840A). The chemical composition and structure of the phases formed were elucidated by transmission electron microscopy (CM 20 TEM/STEM) operated at 200 keV and fitted with an energy-dispersive X-ray (EDX) analyser with an ultra-thin window. EDX spectra were quantified with the virtual standard peaks supplied with the Oxford Instruments eXL software. Powder samples were dispersed in solvent and deposited by pipette on to 3 mm holey copper grids for observation by TEM. In addition, attempt was made to evaluate the crystal structures of the observed compositions/phases by correcting the XRD and TEM diffraction data.

3. Results and discussion

TGA and DTA results for the mixtures synthesized by both B-site precursor methods are shown in Figs. 1 and 2, respectively. In general, similar trend of thermal characteristics is observed in both precursors. As shown in Fig. 1, the powders prepared via both B-site precursor mixed oxide methods demonstrate three distinct weight losses. The first weight loss occurs below 200 °C, the second one between 200–300 °C and the final one after 750 °C. In the temperature range from room temperature to ~150 °C, both samples show small thermal peaks in the DTA curves, Fig. 2, which are related to the first weight loss. These DTA peaks can be attributed to the decomposition of the organic species such as rubber lining from the milling process similar to our earlier reports [13,16]. In comparison between the two B-site precursor routes, after the first weight loss, the columbite route shows a slightly higher weight loss over the temperature range of ~50–220 °C, followed by a much sharper fall in specimen weight with increasing temperature from ~250 to 350 °C. This columbite-precursor method also exhibits larger overall weight loss (~1.25%) than that of the corundum route (~1.00%).

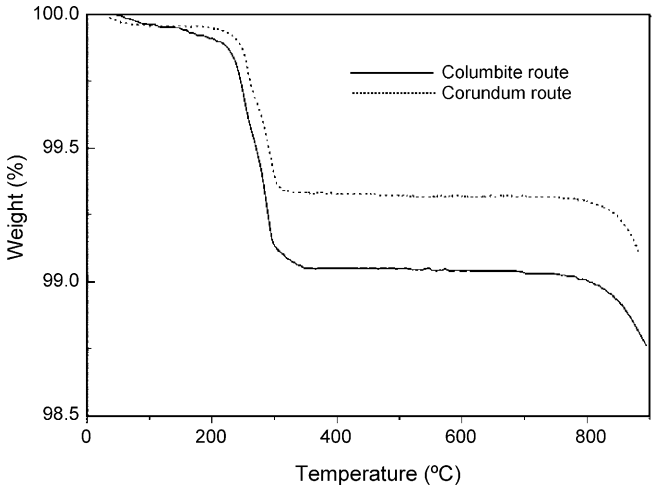

Fig. 1. TGA curves of the mixtures derived from columbite- and corundum-route.

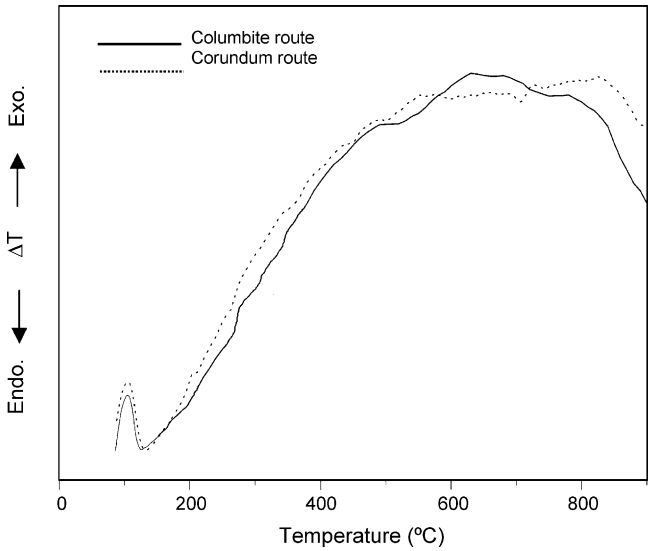

Fig. 2. DTA curves of the mixtures derived from columbite- and corundum-route.

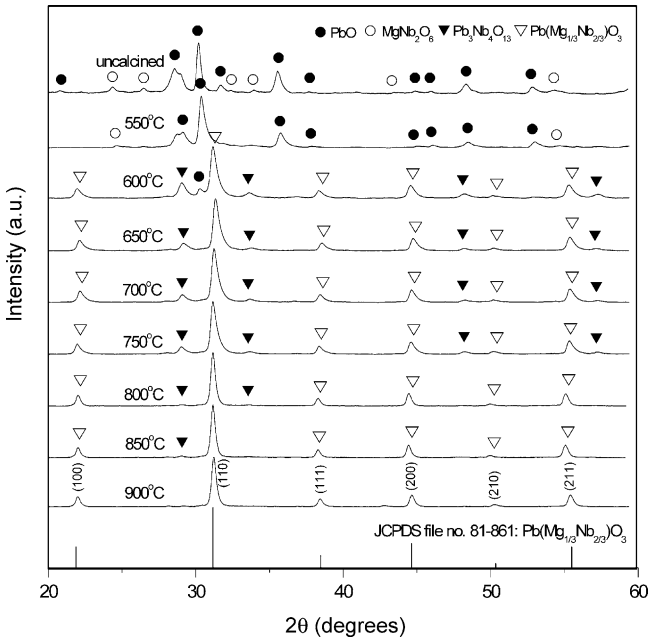

Fig. 3. XRD patterns of the columbite-route powders calcined at various conditions for 1 h with constant heating/cooling rates of 10 °C/min.

Corresponding to the second fall in specimen weight, by increasing the temperature up to ~700 °C, the solid-state reaction occurs between oxide precursors. The broad exothermic characteristic in both DTA curves represents that reaction, which has a maximum at ~600 and 800 °C for columbite- and corundum-routes, respectively. However, it is to be noted that there is no obvious interpretation of these peaks, although it is likely to correspond to a phase transition reported by a number of workers [4–8]. The different temperature, intensities and shapes of the thermal peaks for the two precursors here probably are related to the different starting materials especially magnesium niobate and consequently, caused by the removal of species differently bonded in the network, reactivity of different species (difference in type and dispersion of MgO) in the powders. These data were used to define the range of temperatures for XRD investigation between 550 and 1000 °C. It is to be noted that a significant weight loss in TG curves associated with large thermal change in DTA curves observed at temperatures above 750 °C (Figs. 1 and 2) may be attributed to the PbO volatilisation typically found in lead-based ferroelectrics, consistent with other investigators [17–19].

To study the phase development with increasing calcination temperature in each synthetic route, they were calcined at various temperatures for 1 h in air with constant heating/cooling rates of 10 °C/min, followed by phase analysis using XRD technique. As shown in Fig. 3, for the uncalcined powder and the powder calcined at 550 °C (columbite route), only X-ray peaks of PbO and $MgNb_2O_6$ precursors are present. Similarly, it is seen that unreacted precursors of PbO and $Mg_4Nb_2O_9$ are detected from the original mixture up to 650 °C for the corundum route (Fig. 4). These observations indicate that no reaction was yet triggered during the vibro-milling or low firing processes, in agreement with literature [4,13,16]. It is seen that PMN crystallites were developed in the powder at a calcination temperature as low as 600 and 650 °C for columbite- and corundum-routes, respectively. The results of X-ray diffraction measurement supported the DTA observation (Fig. 2) that PMN phase is formed at approximately 600–800 °C. In general, the strongest reflections apparent in the majority of these XRD patterns indicate the formation of the lead magnesium niobate, PMN (▽). These can be matched with JCPDS file number 81-0861 for the cubic phase, in space group $Pm\bar{3}m$ (no. 221) with cell parameters $a = 404$ pm [20] consistent with other workers [4,5]. According to Fig. 3, the formation of $Pb_3Nb_4O_{13}$ (▼) earlier reported by many researchers [4,21–23] has been found at 600 °C, which

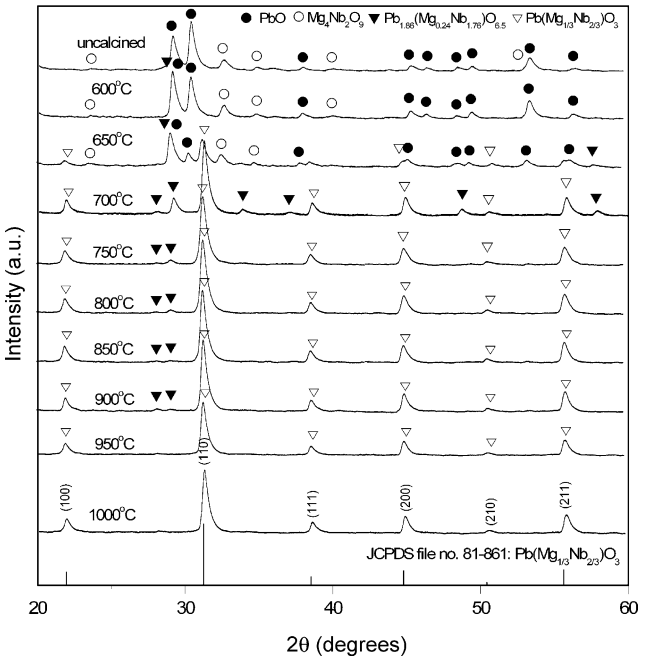

Fig. 4. XRD patterns of the corundum-route powders calcined at various conditions for 1 h with constant heating/cooling rates of 10 °C/min.

is associated to the second TG–DTA response in Figs. 1 and 2. This pyrochlore phase has a cubic structure with cell parameter $a = 1.056$ nm in space group *Fd3m* (no. 227) (JCPDS file number 25-0443) [24]. Upon calcination at 650 °C, the peak corresponding to PbO disappeared (not detectable by XRD). By increasing the calcination temperature from 650 to 850 °C, the yield of the cubic PMN phase increases significantly until at 900 °C, a single-phase of perovskite PMN is formed for the columbite route.

From Fig. 4, it is seen that calcination at 600 °C resulted in some new peak (▼) of the $Pb_{1.86}(Mg_{0.24}Nb_{1.76})O_{6.5}$ phase (JCPDS file number 82-0338) [25] mixing with the unreacted PbO and $Mg_4Nb_2O_9$ phases. To a first approximation, this $Pb_{1.86}(Mg_{0.24}Nb_{1.76})O_{6.5}$ phase earlier reported by many researchers [23,26,27] has a pyrochlore-type structure with a cubic unit cell $a = 1.060$ nm, space group *Fd3m* (no. 227). This pyrochlore phase was found at 600 °C and totally disappeared at 950 °C. As the temperature increased to 900 °C, the intensity of the PMN peaks was further enhanced and PMN becomes the predominant phase, in good agreement with the earlier TG–DTA results. This study also shows that PMN is the only detectable phase in the corundum-route powders after calcination in the range 950–1000 °C.

In the present study, an attempt was also made to calcine both precursors under various dwell times and heating/cooling rates (Figs. 5 and 6). In this connection, it is seen that the single-phase of PMN (yield of 100% within the limitation of the XRD technique) was also found to be possible in columbite-precursor powders calcined at 850 °C for 3 h with heating/cooling rates as fast as 30 °C/min (Fig. 5). The appearance of Nb_2O_5 and $Pb_3Nb_4O_{13}$ phases indicated that chemical decomposition probably caused by PbO volatilisation has occurred at relatively high firing temperatures (>850 °C) with long dwell times, consistent with other workers [4–8]. It is also interesting to note that in this

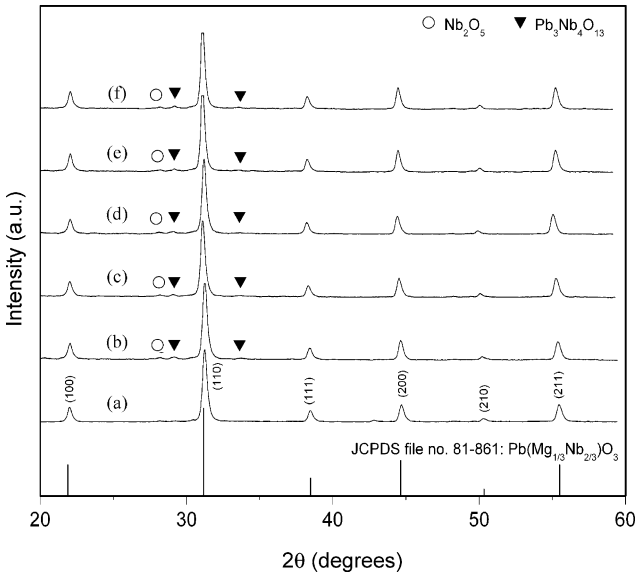

Fig. 5. XRD patterns of the columbite-route powders calcined at 850 °C, for 3 h with heating/cooling rates of (a) 30 °C/min, (b) 20 °C/min and (c) 10 °C/min, (d) for 2 h with heating/cooling rates of 10 °C/min and for 1 h with heating/cooling rates of (e) 30 °C/min and (f) 20 °C/min.

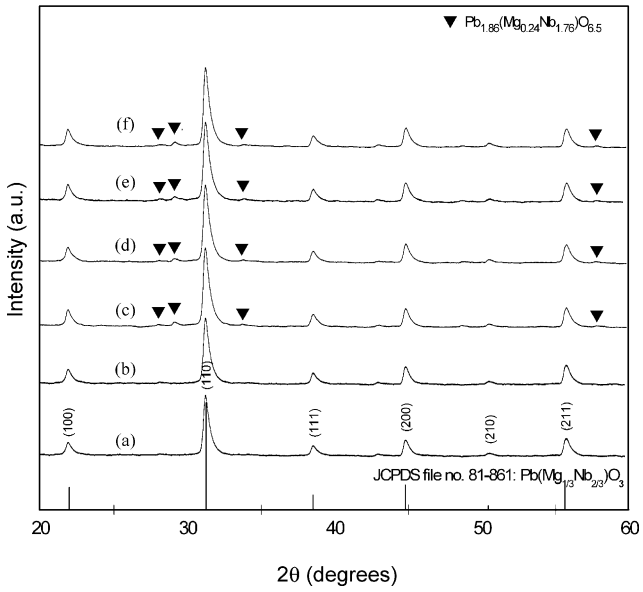

Fig. 6. XRD patterns of the corumdum-route powders calcined at 950 °C for 1 h with heating/cooling rates of (a) 30 °C/min and (b) 20 °C/min, at 900 °C for (c) 2 h (d) 3 h and (e) 4 h, with heating/cooling rates of 10 °C/min, and (f) at 950 °C, for 4 h with heating/cooling rates of 30 °C/min.

work the effects of both dwell time and heating/cooling rates were also found to be significant for the formation of perovskite PMN by using a corundum route (Fig. 6). It is seen that single-phase of PMN powders was also successfully obtained for a calcination temperature of 950 °C for 1 h with heating/cooling rates of 20 or 30 °C/min applied. The observation that the dwell time or heating/cooling rates may also play an important role in obtaining a single-phase of lead-based perovskite ferroelectrics is also consistent with other investigators [4,19,28]. However, some additional peaks at $2\theta \sim 43°$ are found in the Figs. 5(a) and 6(a). It is to be noted that there is no obvious interpretation of these peaks, although it is likely to correspond to a trace of MgO precursor. Nonetheless, with the limitation of X-ray technique and the inherent only single peak with very low intensity comparable to noise originated from the diffractometer, an accurate evaluation of the phase is not possible [15].

It is well established that the perovskite-type PMN tend to form together with the pyrochlore-type PbO–Nb_2O_5 compounds, depending on calcination conditions [7,8,23]. In the work reported here, evidence for the formation of PMN phase, which coexists with the cubic pyrochlore phase, is found after calcination at temperature ~650–900 °C, in agreement with literature [4,7,12,22]. No evidence of $Pb_{1.83}Mg_{0.29}Nb_{1.71}O_{6.39}$ was found, nor was there any indication of the pyrochlore phase of $Pb_3Nb_2O_8$ and $Pb_5Nb_4O_{15}$ [21–23] being present. In general, the formation temperature and dwell times for high purity PMN observed in the powders derived from a combination of a mixed oxide synthetic route and a carefully determined calcination condition (especially with a rapid vibro-milling technique) are slightly lower than those reported for the powders prepared via many other conventional mixed oxide methods [7–11].

Based on the TG–DTA and XRD data, it may be concluded that, over a wide range of calcination conditions, single-

phase perovskite PMN cannot be straightforwardly formed via a two-step B-site precursor method, as verified by a number of researchers [4,7,8]. The experimental work carried out here suggests that the optimal calcination conditions for single-phase PMN are 900 °C for 1 h or 850 °C for 3 h (columbite route) and 950 °C for 1 h (corundum route), with heating/cooling rates as fast as 30 °C/min. The optimised formation temperature of single-phase PMN was lower for the columbite route probably due to the higher degree of reactivity with less reacting species involved [7,8]. As suggested by several workers [8,17], the degree of cation mixing in precursors significantly affects the phase formation behavior in the B-site synthesis of PMN. This observation may be accounted for by the fact that the columbite route possibly provides faster chemical reaction rate (only the reaction between PbO and $MgNb_2O_6$) and is able to enhance the formation of perovskite PMN phase by increasing the reactivity of MgO [8]. However, the minimum firing temperature required for the manufacturing of single-phase corundum $Mg_4Nb_2O_9$ (∼950 °C [14]) is lower than that of columbite $MgNb_2O_6$ (∼1000 °C [13]).

Therefore, in general, the methodology presented in this work provides a simple method for preparing perovskite PMN powders via a solid-state mixed oxide synthetic route. It is interesting to note that, by using either columbite- or corundum-routes, with an optimal calcination condition, the reproducible, low cost and flexible process involving simple solid-state reaction synthetic route can produce high purity perovskite PMN (with impurities undetected by XRD technique) from relatively impure and inexpensive commercially available raw materials.

To further study the influence of precursor on the characteristics of the resulting PMN powders, a combination of particle size analysis, SEM, TEM and EDX is used to examine the powders obtained, as shown in Figs. 7–10 and Table 1. Fig. 7 compares the particle size distribution curves of calcined PMN powders derived from both B-site precursor methods, which indicate an appreciable size fractions at approximately 0.75–1.08 μm diameters, as also listed in Table 1 (averaged sizes). Even taking in account that the analysis does not reveal the real dimension of single particles (due to agglomeration effects as expected from the SEM results in Fig. 8), a uniform frequency distribution curve was observed for the columbite route whilst narrow distribution curve with tiny kink at front covering the range of 0.32–1.65 μm in sizes was found for the corundum route,

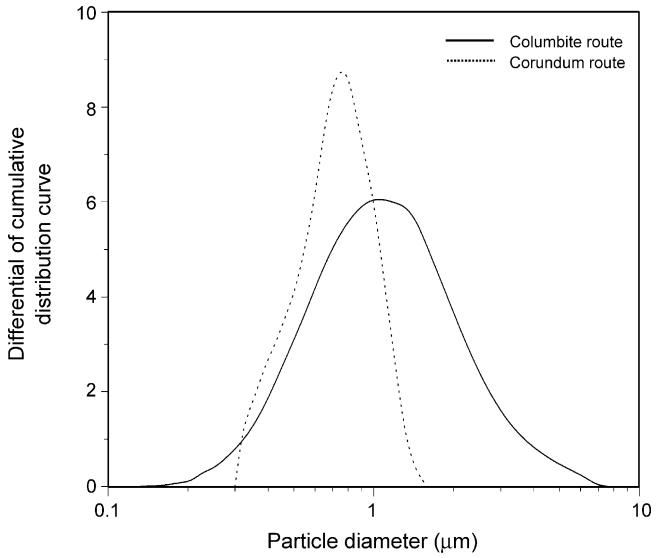

Fig. 7. The particle size curves of the columbite- and corundum-route PMN powders after calcined at their optimised conditions.

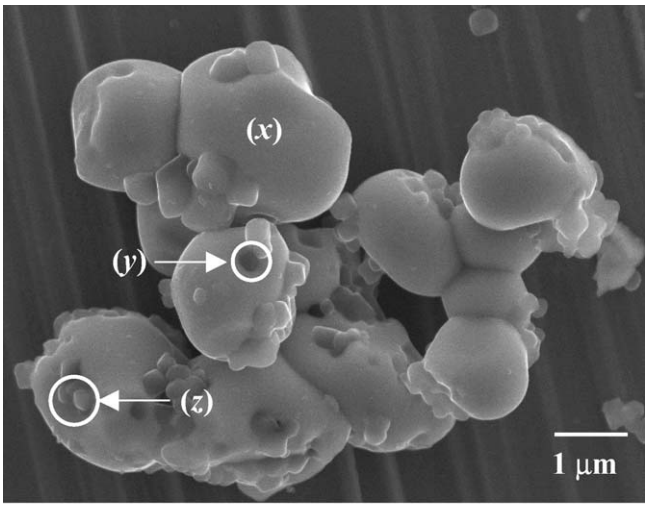

(a)

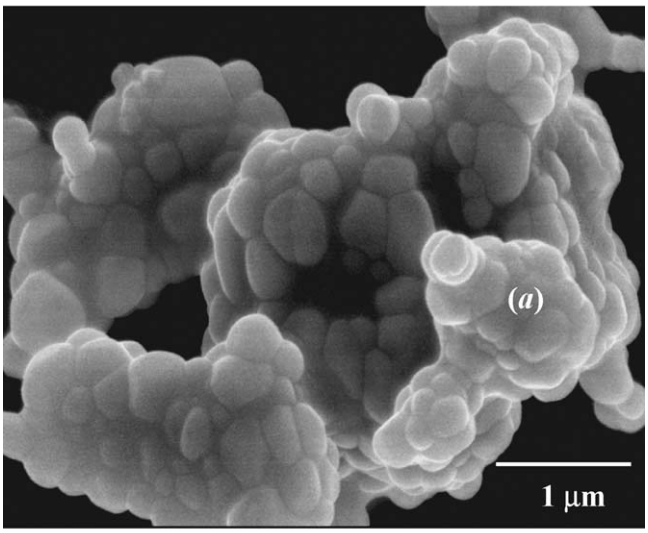

(b)

Fig. 8. SEM micrographs of the: (a) columbite- and (b) corundum-route PMN powders after calcined at their optimised conditions.

Table 1
Particle size data of both PMN powders measured by different techniques

Measurement techniques	Particle size range (average)	
	Columbite route	Corundum route
XRD[a] (nm, ±2.0)	26.60	22.50
Laser diffraction (μm, ±0.2)	0.15–7.50 (1.08)	0.32–1.65 (0.75)
SEM (μm, ±0.1)	0.25–3.00 (1.63)	0.20–1.25 (0.73)
TEM (μm, ±0.01)	0.25–0.65 (0.45)	0.10–0.55 (0.33)

[a] Crystallite size.

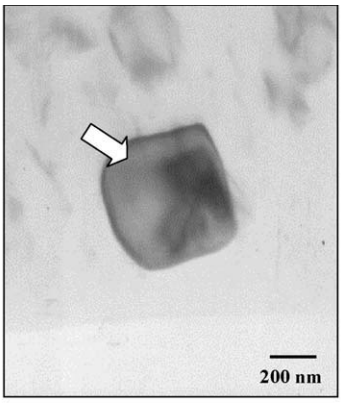

(a)

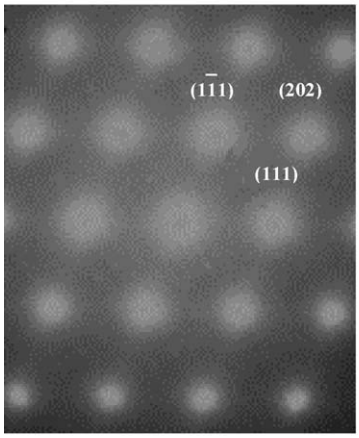

(b)

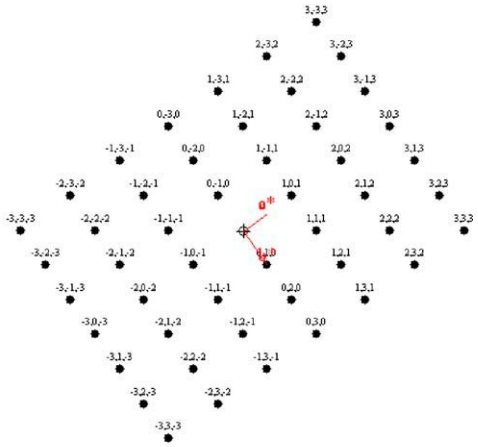

(c)

Fig. 9. (a) TEM micrograph with arrow indicates (b) SAED pattern ([$\bar{1}\,\bar{1}$ 0] zone axes) and (c) reciprocal lattice pattern simulation of the columbite-route PMN particles.

reflecting more the size of agglomerates than the real size of particles.

SEM micrographs of the calcined PMN powders derived from columbite- and corundum-precursor methods are shown in Fig. 8(a and b), respectively. In general, the particles are agglomerated and basically irregular in shape, with a substantial variation in particle size. Observed diameters range from 0.25 to 3.00 and 0.20 to 1.25 μm for columbite- and corundum-routes, respectively, in good agreement with the particle size distribution previously determined (Table 1). The primary particles in the agglomerates are, however, submicron in size. This is confirmed by TEM micrographs shown in Figs. 9 and 10. Additionally, the observed morphology reveals considerable difference in homogeneity, uniformity, size and shape between the two PMN powders. It is obviously evident that the columbite-route powders exhibit more heterogeneous morphology than the corundum-route powders. The columbite-route powders consist mainly of irregular round shape primary particles with a diameter of ∼1 μm or less (Fig. 8(a)). In addition to the primary particles, the powders have another kind of very fine particle (darker particles) with diameter of about 200 nm. A combination of SEM and EDX techniques has demonstrated that pyrochlore and unreacted precursor phases (marked as "*y*" and "*z*" in the micrograph in Fig. 8(a)) exist neighbouring the parent PMN phase (marked as "*x*") (see also Table 2). In general, EDX analysis using a 20 nm probe from a large number of particles of the two calcined powders confirmed the parent composition to be PMN. It is interesting to note that nano-scale MgO and PbO inclusions were also found in the SEM–EDX investigation for the columbite route, in agreement with earlier works [9,29], even though this could not be detected by XRD. It is, therefore, intriguing to note the advantage of a combination between SEM and EDX techniques, which lies in its ability to reveal microstructural features often missed by the XRD method which requires at least 5 wt% of the component [15].

However, it is seen that higher degree of agglomeration with more rounded particle morphology is observed in the powders produced by the corundum route (Fig. 8(b)). The strong inter-particle bond within each aggregate is evident by the formation of a well-established necking between neighbouring particles.

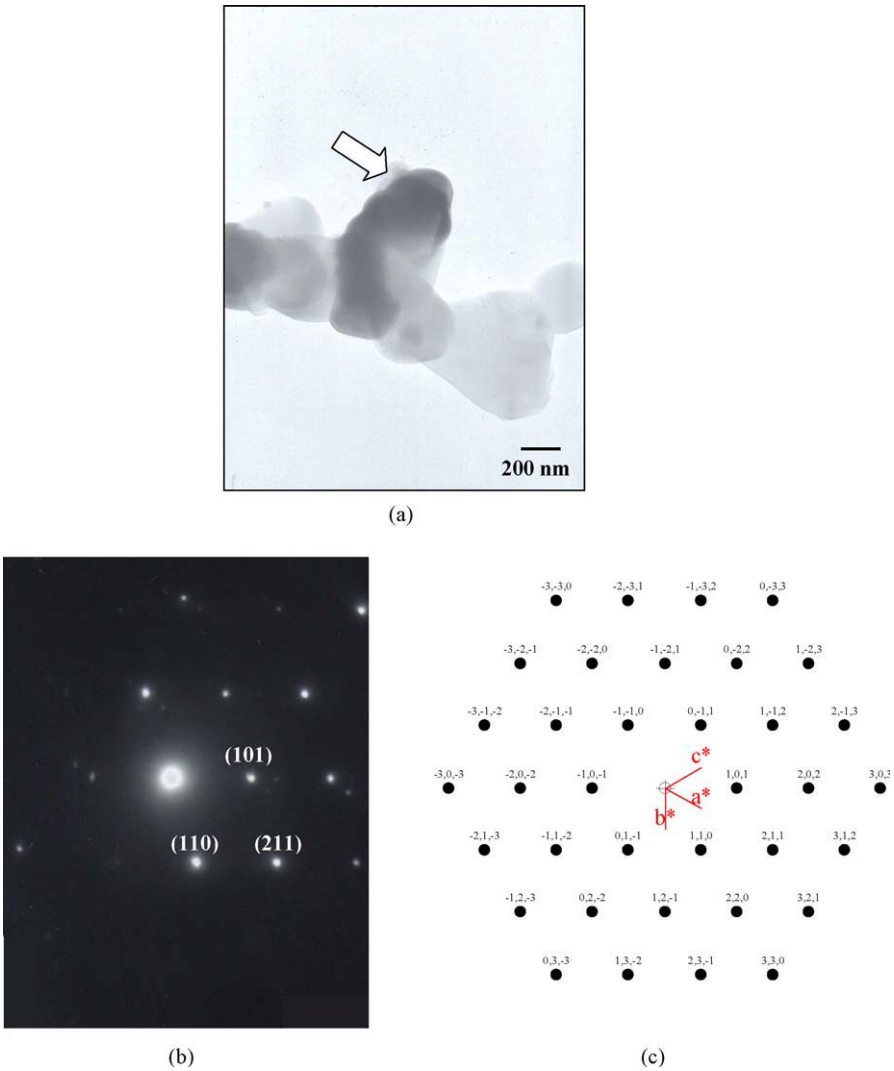

Fig. 10. (a) TEM micrograph with arrow indicates (b) SAED pattern ([$\bar{1}$ 1 1] zone axes) and (c) reciprocal lattice pattern simulation of the corundum-route PMN particles.

This observation could be attributed to the mechanism of surface energy reduction of the ultrafine powders, i.e. the smaller the powder the higher the specific surface area [30]. In general, it is seen that primary particle in corundum-route powders is clearly smaller in size than the columbite-route powders. The averaged particle size of corundum-precursor PMN powders with finer particle size is regarded as advantage for better reactivity.

Bright field TEM images of discrete particles of the calcined PMN powders are shown in Figs. 9(a) and 10(a) for the columbite- and corundum-routes, respectively, indicating the particle sizes and shapes at higher magnifications. The observed morphology reveals the considerable difference in both size and shapes between the two particles. Primary particle in the columbite-route PMN powders is clearly larger in size and also higher in angularity than the corundum-route powders. By employing a combination of both selected area electron diffraction (SAED) and crystallographic analysis, the perovskite phase of cubic PMN was identified for the columbite- and corundum-

Table 2
EDX analysis on PMN powders derived from columbite- and corundum-routes

EDX positions	Composition (at.%)			Possible phase(s)
	Pb (M)	Mg (K)	Nb (L)	
x	43.12	18.87	38.01	$Pb(Mg_{1/3}Nb_{2/3})O_3$
y	8.45	84.10	7.45	$Pb_{1.86}(Mg_{0.24}Nb_{1.76})O_{6.5}$ (M), $Pb_{1.83}(Mg_{0.29}Nb_{1.71})O_{6.39}$ (m), MgO (m)
z	5.75	89.85	4.40	$Pb_{1.86}(Mg_{0.24}Nb_{1.76})O_{6.5}$ (M), $Pb_{1.83}(Mg_{0.29}Nb_{1.71})O_{6.39}$ (m), MgO (m), PbO (m)
a	45.04	17.75	37.21	$Pb(Mg_{1/3}Nb_{2/3})O_3$

M, Majority; m, Minority.

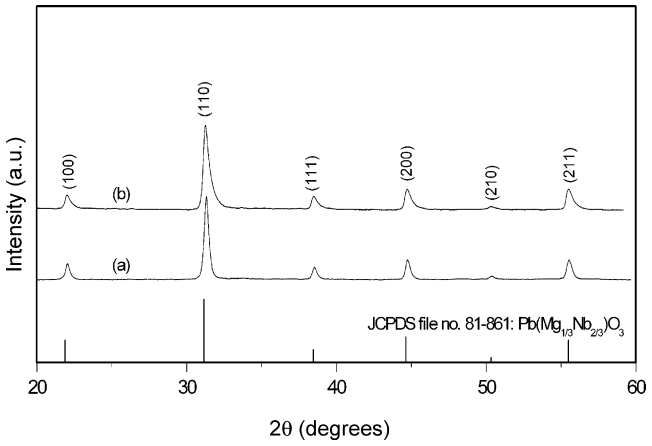

Fig. 11. XRD patterns of PMN ceramics derived from: (a) columbite- and (b) corundum-routes after sintering at 1225 °C for 2 h.

routes as shown in Figs. 9(b and c) and 10(b and c), respectively, in good agreement with the XRD results.

Preliminary study on the ceramic production from the powders prepared from both routes was also conducted. As shown in Fig. 11, it can be seen that the single-phase perovskite PMN ceramics can be prepared by sintering both PMN powders at 1225 °C for 2 h based upon the firing condition advocated by Ananta and Thomas [5].

4. Conclusions

It has been shown that single-phase perovskite PMN powders can be successfully formed by employing either columbite or corundum B-site precursor method via a rapid vibro-milling. Evidence for the formation of a cubic pyrochlore phase, which coexists with the perovskite PMN parent phase, is found at calcination temperture ranging from 800 to 1050 °C. Amongst the two B-site precursor methods, it is seen that lower optimised calcination temperature for the production of pure PMN powders can be obtained by using the columbite route, whereas the smallest obtainable particle size was found in the corundum-route PMN powders.

Acknowledgements

The authors gratefully acknowledge the Thailand Research Fund (TRF), the Faculty of Science and the Graduate School, Chiang Mai University for all support.

References

[1] A.J. Moulson, J.M. Herbert, Electroceramics, second ed., Wiley, Chichester, 2003.
[2] G. Haertling, J. Am. Ceram. Soc. 82 (1999) 797.
[3] K. Uchino, Piezoelectrics and Ultrasonic Applications, Kluwer, 1998.
[4] S. Ananta, N.W. Thomas, J. Eur. Ceram. Soc. 19 (1999) 155–163.
[5] S. Ananta, N.W. Thomas, J. Eur. Ceram. Soc. 19 (1999) 629–635.
[6] Y.-C. Liou, J.H. Chen, Ceram. Int. 30 (2004) 17–22.
[7] S.L. Swartz, T.R. Shrout, Mater. Res. Bull. 17 (1982) 1245–1250.
[8] T.R. Shrout, A. Halliyal, Am. Ceram. Soc. Bull. 66 (1987) 704–711.
[9] E. Goo, K. Okazaki, J. Am. Ceram. Soc. 69 (1986) C188–C190.
[10] M. Lejeune, J.P. Boilot, Mater. Res. Bull. 20 (1985) 493–499.
[11] P.A. Joy, K. Sreedhar, J. Am. Ceram. Soc. 80 (1997) 770.
[12] C.H. Lu, H.S. Yang, Mater. Sci. Eng. B84 (2001) 159.
[13] S. Ananta, Mater. Lett. 58 (2004) 2781–2786.
[14] S. Ananta, Mater. Lett. 58 (2004) 2530–2536.
[15] H.P. Klug, L.E. Alexander, X-ray Diffraction Procedures, second ed., Wiley, New York, 1974.
[16] R. Wongmaneerung, R. Yimnirun, S. Ananta, Mater. Lett. 60 (2006) 1447–1452.
[17] J.P. Guha, J. Mater. Sci. 36 (2001) 5219–5226.
[18] J. Ryu, J.J. Choi, H.E. Kim, J. Am. Ceram. Soc. 84 (2001) 902.
[19] A. Udomporn, S. Ananta, Mater. Lett. 58 (2004) 1154–1159.
[20] Powder Diffraction File No. 81-0861, International Centre for Diffraction Data, Newton Square, PA, 2000.
[21] M.M.A. Sekar, A. Halliyal, J. Am. Ceram. Soc. 81 (1998) 380–388.
[22] N.K. Kim, Mater. Lett. 32 (1997) 127–130.
[23] M. Dambekalne, I. Brante, A. Sternberg, Ferroelectrics 90 (1989) 1–14.
[24] Powder Diffraction File No. 25-0443, International Centre for Diffraction Data, Newton Square, PA, 2000.
[25] Powder Diffraction File No. 82-0338, International Centre for Diffraction Data, Newton Square, PA, 2000.
[26] J.P. Guha, J. Mater. Sci. 34 (1999) 4985–4994.
[27] L.P. Cruz, A.M. Segadães, J. Rocha, J.D. Pedrosa de Jesus, Mater. Res. Bull. 37 (2002) 1163–1173.
[28] R. Tipakontitikul, S. Ananta, Mater. Lett. 58 (2004) 449.
[29] A.L. Costa, G. Fabbri, E. Roncari, C. Capiani, C. Galassi, J. Eur. Ceram. Soc. 21 (2001) 1165–1170.
[30] J.S. Reeds, Principles of Ceramic Processing, second ed., Wiley, New York, 1995.

ELSEVIER

Materials Science and Engineering B 132 (2006) 300–306

MATERIALS SCIENCE & ENGINEERING B

www.elsevier.com/locate/mseb

Phase development and dielectric properties of $(1-x)Pb(Zr_{0.52}Ti_{0.48})O_3$–$xBaTiO_3$ ceramics

Wanwilai Chaisan [a,*], Rattikorn Yimnirun [a], Supon Ananta [a], David P. Cann [b]

[a] *Department of Physics, Faculty of Science, Chiang Mai University, Chiang Mai, Thailand*
[b] *Department of Mechanical Engineering, Oregon State University, Corvallis, OR, USA*

Received 8 February 2006; received in revised form 27 April 2006; accepted 28 April 2006

Abstract

$(1-x)Pb(Zr_{0.52}Ti_{0.48})O_3$–$xBaTiO_3$ ceramics were prepared by a modified mixed-oxide method. The phase formation was studied by XRD analysis. All compositions exhibit complete solid solutions of perovskite-like phase in the $(1-x)$PZT–xBT system. The (2 0 0)/(0 0 2) peak was found to split at the composition $x = 0.6$ and the co-existence of tetragonal–rhombohedral phases occurs with $x \leq 0.6$. The possible range of compositions which correspond to a phase transition is $0.6 < x < 0.7$. While pure BT ceramics exhibited a sharp phase transformation expected for normal ferroelectrics, phase transformation behavior of the $(1-x)$PZT–xBT solid solutions became more diffuse with increasing BT contents. This was primarily evidenced by an increased broadness in the dielectric peak, with a maximum peak width occurring at $x = 0.5$.

Keywords: Phase development; Dielectric properties; Barium titanate (BT); Lead zirconate titanate (PZT)

1. Introduction

Nowadays, many researches have been carried out on the phase development and dielectric behavior of various perovskite ferroelectric ceramics, which can be applied to several micro- and nano-electronic devices such as multilayer capacitors, microactuators and miniaturized transducers [1,2]. Among the many ferroelectric materials, barium titanate ($BaTiO_3$ or BT) and lead zirconate titanate ($Pb(Zr,Ti)O_3$ or PZT) are representative perovskite ferroelectric and piezoelectric prototypes because of their excellent electrical properties [3,4]. While, barium titanate is a normal ferroelectric with a high dielectric constant and a relatively low T_C (~120 °C), lead zirconate titanate has a higher T_C of 390 °C which allows PZT-based piezoelectric devices to be operated at relatively higher temperatures [2,5]. Although BT ceramic has better mechanical properties than PZT, the sintering temperature is also higher [1,3,5]. Thus, mixing PZT with BT is expected to decrease the sintering temperature of BT-based ceramics, a desirable move towards electrode of lower cost [6]. Moreover, since PZT–BT is not a pure-lead system, it is easier to prepare single phase ceramics with lower amount of undesirable pyrochlore phases [7,8]. With their complimentary characteristics, it is expected that excellent properties can be obtained from ceramics in PZT–BT system.

So far, there have been only a few studies on PZT–BT system [7–9]. These studies have focused mainly on powder preparation and some electrical properties. However, there have been no systematic studies on the phase development and dielectric properties of the whole series of PZT–BT compositions, which would help in identifying excellent electrical properties within this system. In the present study, PZT and BT were chosen as end components to prepare solid solutions via a modified mixed-oxide method. Phase development and lattice parameter changes of the whole series are investigated by XRD analysis. Finally, the dielectric properties of PZT–BT ceramics are determined as a function of temperature and frequency to establish structure–property relationships.

2. Experimental procedure

The $(1-x)$PZT–xBT compositions with $0.0 \leq x \leq 1.0$ were prepared by a modified mixed-oxide method [7]. The starting raw materials were reagent grade PbO, ZrO_2, TiO_2 and $BaCO_3$ powders (Fluka, >99% purity). For BT powder, $BaCO_3$ and TiO_2 were homogeneously mixed via ball-milling with zirconia media in ethanol for 24 h. The mixture was dried and

* Corresponding author. Tel.: +66 53 943 376; fax: +66 53 943 445.
E-mail address: wanwilai_chaisan@yahoo.com (W. Chaisan).

0921-5107/$ – see front matter © 2006 Elsevier B.V. All rights reserved.
doi:10.1016/j.mseb.2006.04.033

then calcined at 1300 °C for 2 h to form $BaTiO_3$. The PZT powders were synthesized through the modified mixed-oxide method, in which lead zirconate ($PbZrO_3$) was first prepared and then used as precursor in order to reduce the occurrence of undesirable pyrochlore phase, as well as very high melting temperature $ZrTiO_4$ phase, which is difficult to eliminate [7]. Pure $PbZrO_3$ phase was formed by reacting PbO with ZrO_2 at 800 °C for 2 h. $PbZrO_3$ powder was then mixed with PbO and TiO_2 and calcined at 900 °C for 2 h to form single phase PZT. The (1−*x*)PZT–*x*BT powders were then formulated from the BT and PZT components by employing the similar mixed-oxide procedure and calcining at various temperatures between 900 and 1300 °C for 2 h in order to obtain single phase (1−*x*)PZT–*x*BT powders. The phase formation process was followed by XRD analysis. The lattice parameters *a* and *c* were determined by using a non-linear least squares method [10]. The (1−*x*)PZT–*x*BT powders were then isostatically cold-pressed at 4 MPa into pellets, which were consequently sintered between 1050 to 1350 °C for 2 h in air. The grain morphology and size were directly imaged using scanning electron microscopy (SEM) and the average grain size was determined by using a mean linear intercept method [11]. For dielectric measurements, silver paste was fired on both sides of the polished samples at 550 °C for 30 min as the electrodes. Dielectric properties of the sintered ceramics were studied as a function of both temperature and frequency. The capacitance was measured with a HP4284A LCR meter in connection with a Delta Design 9023 temperature chamber and a sample holder (Norwegian Electroceramics) capable of high temperature measurement. Relative permittivity (ε_r) was calculated using the geometric area and thickness of discs.

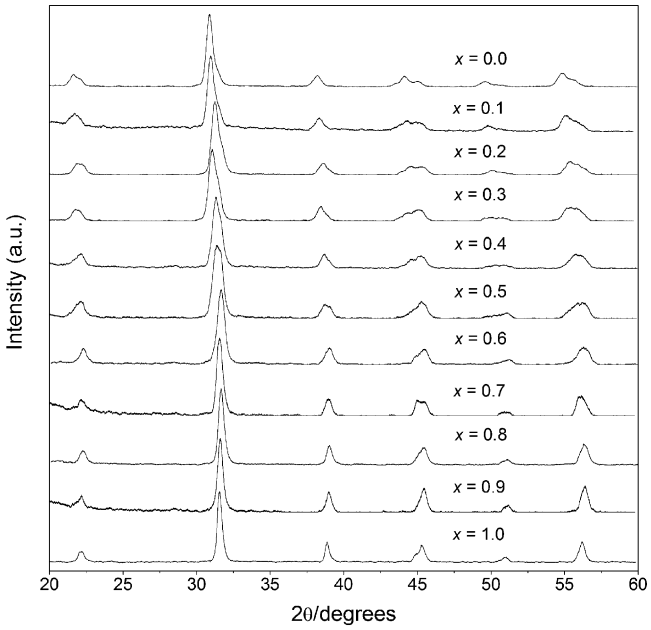

Fig. 1. XRD diffraction patterns of (1−*x*)PZT–*x*BT powders.

3. Results and discussion

The phase formation behavior of the (1−*x*)PZT–*x*BT powders is revealed by XRD as shown in Fig. 1. The diffraction pattern of powders with $x = 1.0$ match exactly that of perovskite $BaTiO_3$ (JCPDS no. 75-0460), whereas that of $x = 0.0$ is of a perovskite structure of $Pb(Zr_{0.52}Ti_{0.48})O_3$ with co-existence of both tetragonal and rhombohedral phases, matching with the

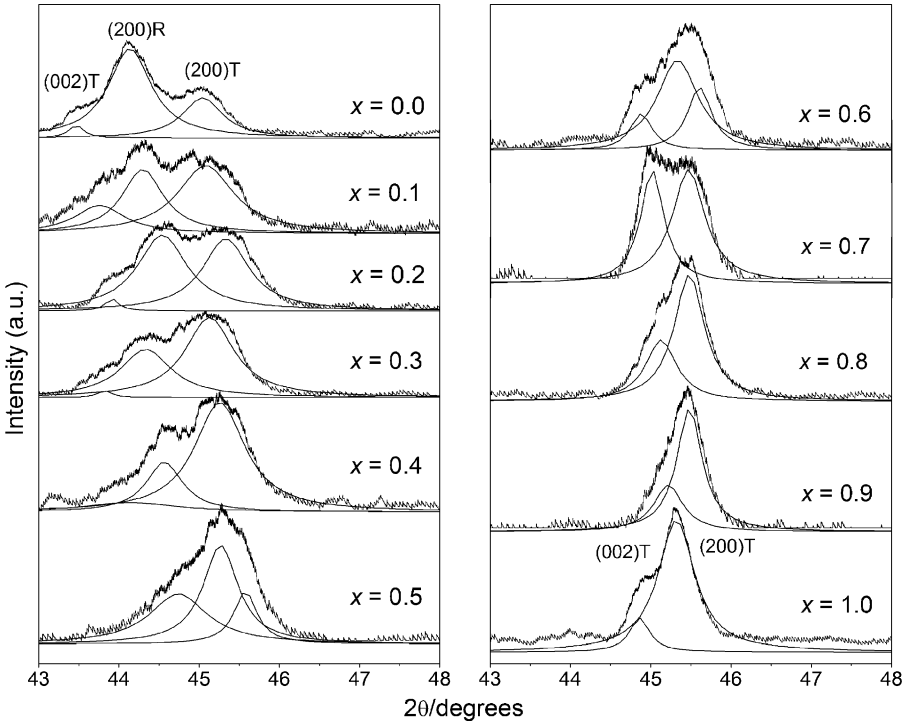

Fig. 2. XRD diffraction patterns for the (2 0 0) peaks of (1−*x*)PZT–*x*BT powders. Deconvolution of data shows the relative proportions of the rhombohedral and tetragonal phases.

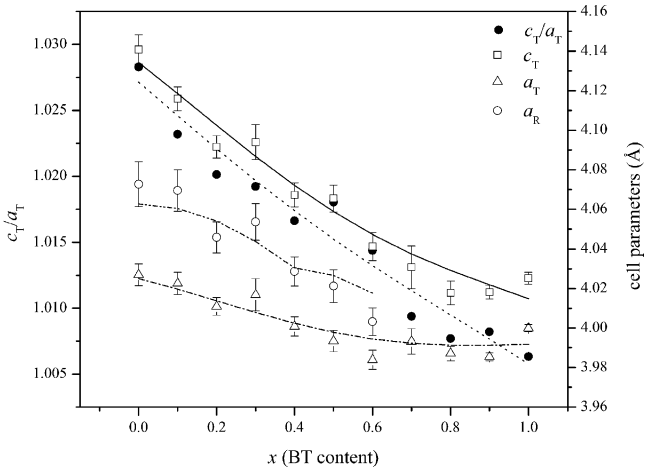

Fig. 3. Variation of cell parameters in the (1−x)PZT–xBT system. The solid and dashed lines are guides for the eyes.

JCPDS file no. 33-0784 and 73-2022, respectively. In the ladder pattern, a series of continuous solid solutions of PZT–BT with perovskite structure without any trace of pyrocholre phase normally forms. With increasing PZT content, the diffraction peaks shifted towards lower angle and the diffraction peak around 2θ of 43–46° was found to split at composition $x = 0.6$ (as shown in Fig. 2). This observation suggests that 0.4PZT–0.6BT composition may lead to a diffuse morphotropic phase boundary (MPB) between the tetragonal and rhombohedral PZT phases [12]. This is further evidenced in Fig. 2, which shows the evolution of the (2 0 0)/(0 0 2) peak as a function of composition over the range $2\theta = 43$–48. The data indicate the appearance of a triplet peak due to the superposition of the tetragonal and rhombohedral (2 0 0) peaks. With increasing PZT content, the intensity ratio of the (2 0 0)/(0 0 2) peak tends to decrease down to $x = 0.6$, where the rhombohedral peak is first observed. The XRD patterns with high degree of PZT content ($x \leq 0.6$) showed in all cases the co-existence of both tetragonal and rhombohedral phases as clearly shown in Fig. 2. The variation of these triplet-diffraction lines could be explained by microscopic compositional fluctuations occurring in these perovskite materials, which cannot provide real homogeneity in the solid solutions, and also by the different stresses induced in the particles, which determine the co-existence of tetragonal–rhombohedral phases [13,14].

The lattice parameters were then determined from the triplets (2 0 0) by using a non-linear least squares method [10]. The a-parameter, c-parameter and tetragonality (c/a) of (1−x)PZT–xBT ceramics are plotted as a function of BT content in Fig. 3. The results show that cell parameters of all compositions gradually decrease with increasing BT content as expected from the steady increase in 2θ of diffraction peaks (Fig. 2) and agreed with Vegard's law [15]. Thus, the perovskite PZT–BT system is confirmed to develop a complete solid solubility, as also observed in similar solid solutions [14]. However, the composition boundary between the real tetragonal and rhombohedral

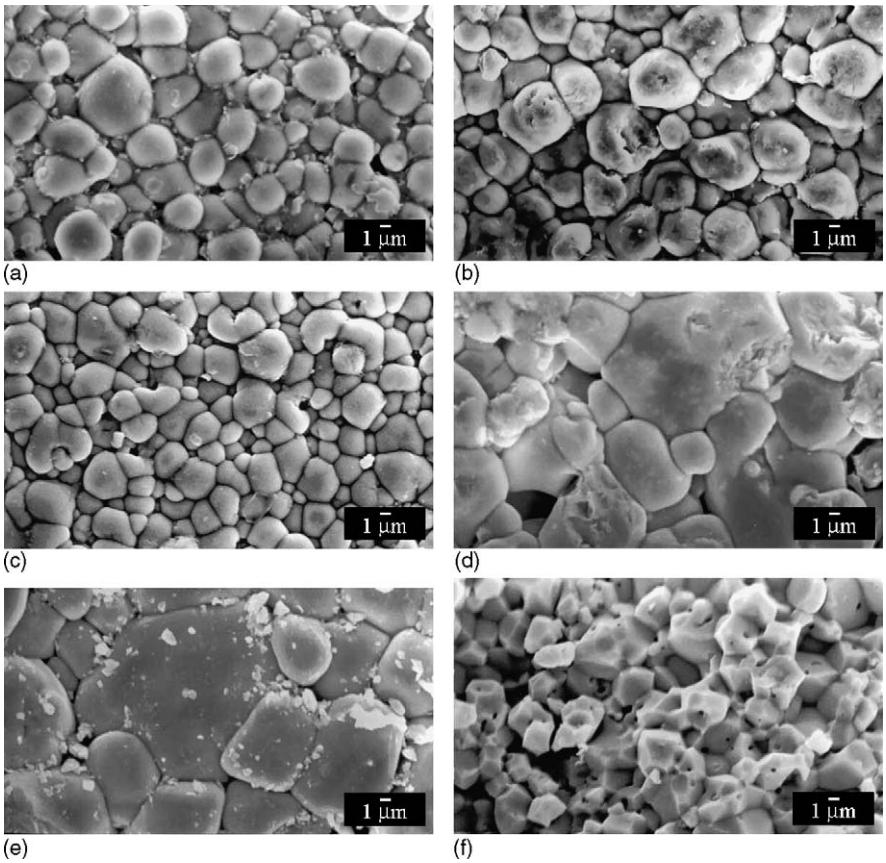

Fig. 4. The microstructure of (1−x)PZT–xBT ceramics: (a) $x = 0.0$, (b) $x = 0.1$, (c) $x = 0.3$, (d) $x = 0.7$, (e) $x = 0.9$ and (f) $x = 1.0$.

Table 1
Characteristics of (1−x)PZT–xBT ceramics with optimized processing conditions

Compositions	Sintering temperature (°C)	Density (g/cm^3)	Average grain size (μm)
PZT	1100	7.7	2.36
0.9PZT–0.1BT	1200	7.6	2.86
0.7PZT–0.3BT	1200	7.2	1.97
0.6PZT–0.4BT	1250	6.9	2.31
0.5PZT–0.5BT	1250	6.6	3.87
0.4PZT–0.6BT	1250	6.3	4.19
0.3PZT–0.7BT	1250	5.7	3.71
0.1PZT–0.9BT	1300	5.3	5.72
BT	1350	5.8	2.42

phases could not be delimited under the present experimental limit of accuracy. The possible range of compositions which corresponds to a phase transition is $0.6 < x < 0.7$ and high resolution XRD analysis is clearly necessary to detect the possible superposition of phases in further studies.

The optimized sintering temperatures, densities, and average grain sizes of the sintered (1−x)PZT–xBT ceramics are listed in Table 1. Higher firing temperatures were necessary for compositions containing a large fraction of BT. The microstructure of (1−x)PZT–xBT ceramics is shown in Fig. 4. Compositions with $x = 0.7$ and 0.9 could not be sintered to sufficient densities and the theoretical densities of ceramics in this range were about 86–89%. It is possible that volatilization of PbO during firing is the main reason for the failure in preparing dense ceramics over this composition range [16,17]. It should be noted that the grain size and density can influence dielectric properties [4] but in the present work average grain size varies between 2 and 5 μm, as shown in Table 1, which should not play significant role in variation of dielectric properties. The variation of the dielectric constant with temperature for ceramics with $x = 0.0$–0.6 is displayed in Fig. 5. The Curie temperatures and maximum dielectric constants of the pure PZT ceramics in this work was 390 °C and 14,900, respectively. With increasing BT content, the transition temperature shifts monotonously to lower temperatures and dielectric peak becomes broader, indicating the increasing of diffused phase transition. The frequency dependence of dielectric properties for $x = 0.0$ and 0.5 ceramics is shown in Fig. 6. For $x = 0.0$ (pure PZT) (Fig. 6a), the ε_r peak is sharp and approaches 15,000. A normal ferroelectric behavior is observed in PZT as evident by a relatively weak frequency dependence of dielectric properties, except at low frequencies as a result of high temperature space charge conduction. Similar observation is also found for pure BT. On the other hand, a diffuse phase transition and small frequency dispersion of the dielectric maxima are observed in $x = 0.5$ ceramic (Fig. 6b). Moreover, it should also be noted here that the dielectric constant rises and dielectric loss significantly increases at high temperature as a result of thermally activated space charge conduction [18]. For PZT ceramic (Fig. 6a), a dielectric constant at the lower frequencies seems to increase continuously. It can be assumed that polar defect pairs created under these conditions and may be related to such dielectric anomaly [19].

As described above, a combination of PZT with BT introduces dielectric peak broadening. For better understanding of the interesting dielectric behaviors of PZT–BT system, we look at these behaviors through Curie–Weiss law. For a normal ferroelectric such as PZT and BT, above the Curie temperature the

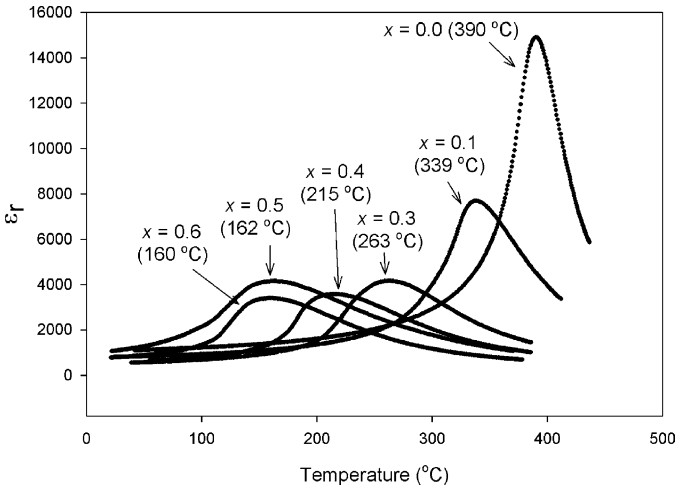

Fig. 5. Variation of dielectric constant (ε_r) with temperature for (1−x)PZT–xBT ceramics at 500 kHz (T_C of each composition is indicated in parenthesis).

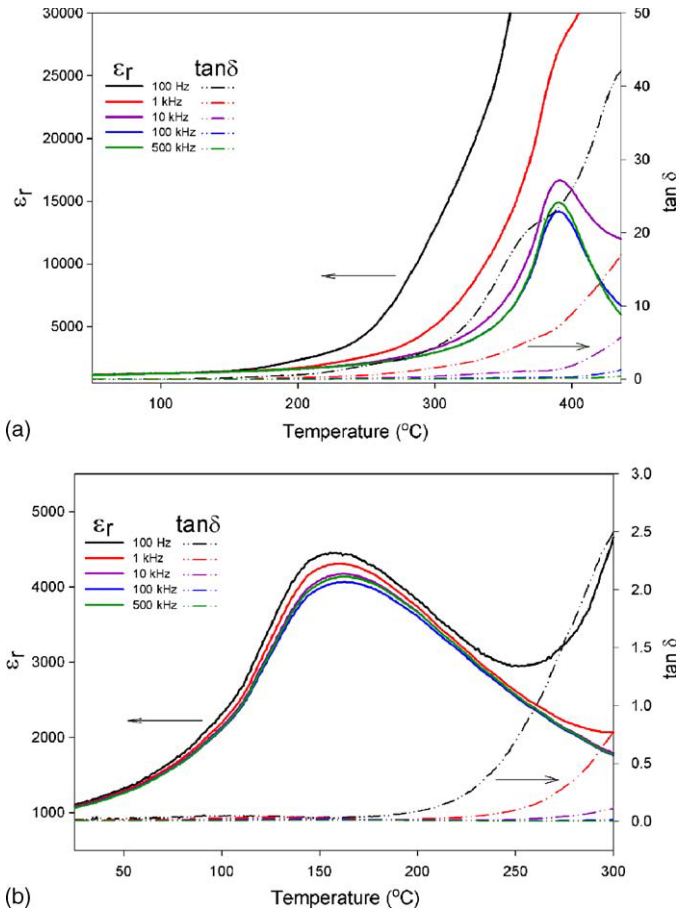

Fig. 6. Temperature and frequency dependence of the dielectric properties for: (a) $x = 0.0$ and (b) $x = 0.5$ ceramics.

dielectric constant follows the Curie–Weiss law:

$$\varepsilon = \frac{c}{T - T_0} \tag{1}$$

where c is the Curie constant and T_0 is the Curie–Weiss temperature [1,20,21]. For a ferroelectric with a diffuse phase transition (broad peak), the following equation:

$$\frac{1}{\varepsilon} = (T - T_m)^2 \tag{2}$$

has been shown to be valid over a wide temperature range instead of the normal Curie–Weiss law (Eq. (1)) [22,23]. In Eq. (2), T_m is the temperature at which the dielectric constant is maximum.

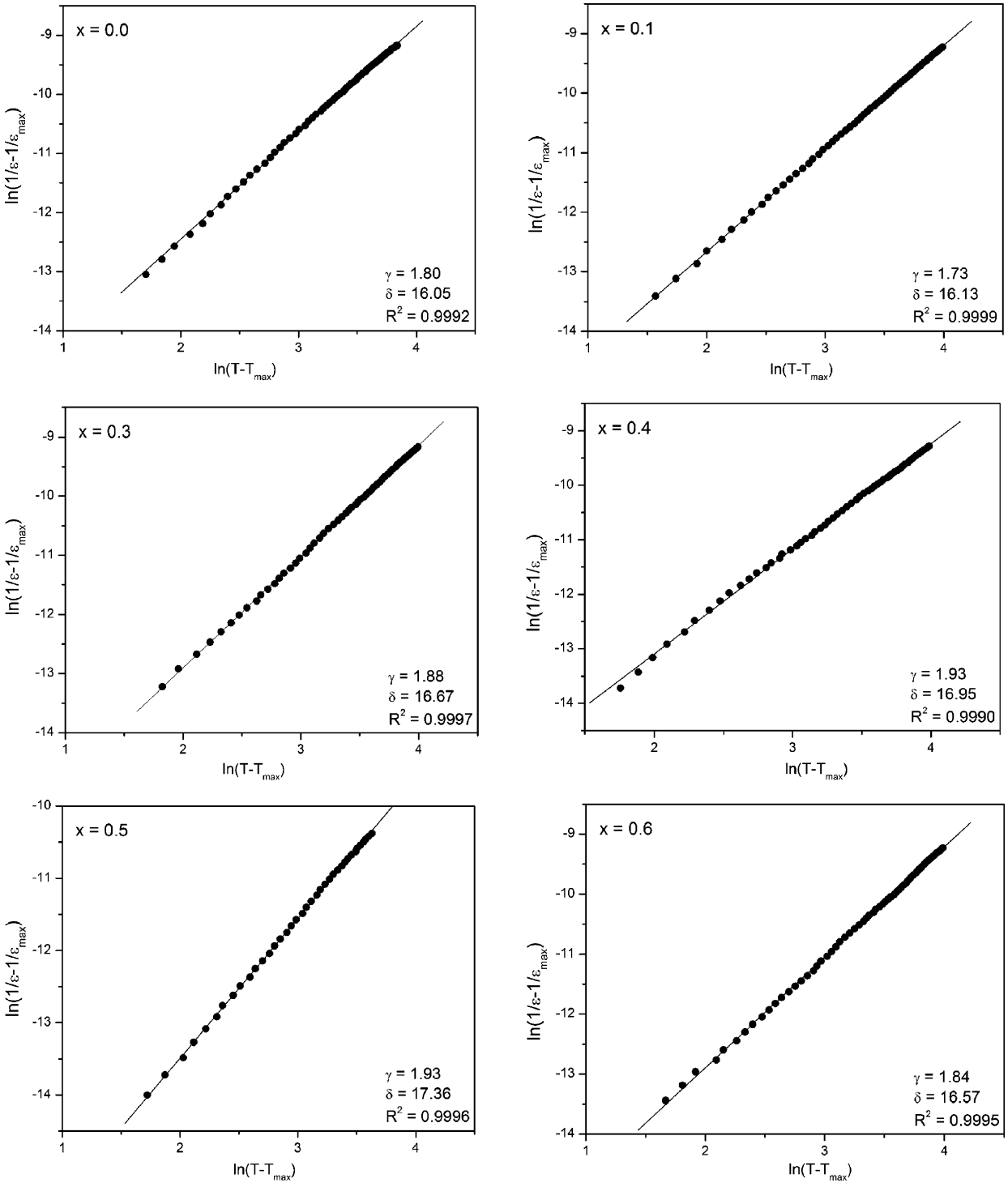

Fig. 7. Plots of $\ln((1/\varepsilon)-(1/\varepsilon_m))$ vs. $\ln(T-T_m)$ for $(1-x)$PZT–xBT ceramics. The solid lines are fits to Eq. (3). γ, δ and R^2 indicate fitting parameters (γ and δ) and correlation of the fit (R^2).

If the local Curie temperature distribution is Gaussian, the reciprocal permittivity can be written in the form [23,24]:

$$\frac{1}{\varepsilon} = \frac{1}{\varepsilon_m} + \frac{(T - T_m)^\gamma}{2\varepsilon_m \delta^2} \quad (3)$$

where ε_m is maximum permittivity, γ the diffusivity and δ is diffuseness parameter. For $(1-x)$PZT–xBT compositions, the diffusivity (γ) and diffuseness parameter (δ) can be estimated from the slope and intercept of the dielectric data shown in Fig. 7, which should be linear. The values of γ and δ are both materials constants depending on the composition and structure of materials [24]. The value of γ is the expression of the degree of dielectric relaxation, while the parameter δ is used to measure the degree of diffuseness of the phase transition. In a material with the "pure" diffuse phase transition described by the Smolenskii–Isutov relation (Eq. (2)), the value of γ is expected to be 2 [18]. The plots shown in Fig. 7 show that the variation is very linear with the correlation of all the fits $\geq$0.999. The mean value of the diffusivity (γ) is extracted from these plots by fitting a linear equation. The values of γ illustrated in Fig. 8 vary between 1.73 and 1.93, which confirms that diffuse phase transition occur in PZT–BT system. However, the phase transition in this system can be considered as "no purely" diffuse as the γ value is not equal to 2 [18]. Since for a perovskite ferroelectric it is established that the values of γ and δ could be caused by microstructure feature, density and grain size [18,25]. However, the relationship between these values, density and grain size in this work has not shown a very clear tendency. Nevertheless, this density and grain size effect can partly be the cause of increasing of the diffusivity when BT is added to PZT since the average grain size ranges from 2.4 μm in PZT to 4.2 μm in 0.4PZT–0.6BT, while the density decreases from 7.7 g/cm^3 in PZT to 6.3 g/cm^3 in 0.4PZT–0.6BT. With increasing BT content, the values of γ and δ seem to increase linearly over the wide composition range (as plotted in Fig. 8), which indicates more diffuse phase behavior in PZT–BT system with increasing BT content (up to $x = 0.5$). It should be noted the value of γ for PZT is nearly 2 (theoretical is 1 for normal ferroelectric with sharp phase transition). This is probably because the mixing of rhombohedral and tetragonal phases in PZT compound (verified by XRD in Fig. 2) and a formation of pyrochlore phase in pure PZT (though not detected by XRD) induced the occurrence of the chemical disorder and composition heterogeneity, which in turn lead to more diffuse phase transition behavior in PZT. As adding 10 mol% BT to PZT, the value of γ slightly drops from 1.78 to 1.73, it can be assumed that small amount of BT helps stabilize perovskite phase in PZT, as observed earlier by Halliyal et al. [23] in case of PZN. However, with further increase in BT content, γ value increases and reaches the highest value at $x = 0.5$. The appearance of diffuseness has been normally argued in terms of variations in local composition giving rise to distinct microregions, each of which has slightly different Curie point for its ferro-paraelectric phase transition resulting in a broad dielectric peak [18,26,27]. In this study, the variation in the diffuseness (Fig. 8) appears to coincide with the XRD results in Fig. 2, which indicate the co-existence of both tetragonal and rhombohedral phases and the microscopic composition fluctuations as a result of incomplete homogeneity in the PZT–BT solid solution. In addition, it is believed that there is an incomplete solubility of BT phase in PZT, little amount of BT (not detected by XRD) could remain as a secondary phase, leading to heterogeneous compositions. This composition heterogeneity also gives rise to random fields, which tend to make the phase transition "diffuse" instead of sharp as in normal ferroelectric [26,27]. For the compositions with $x > 0.5$, BT is now a dominant phase and the situation is reversed, hence the values of γ and δ then decrease with increasing BT content.

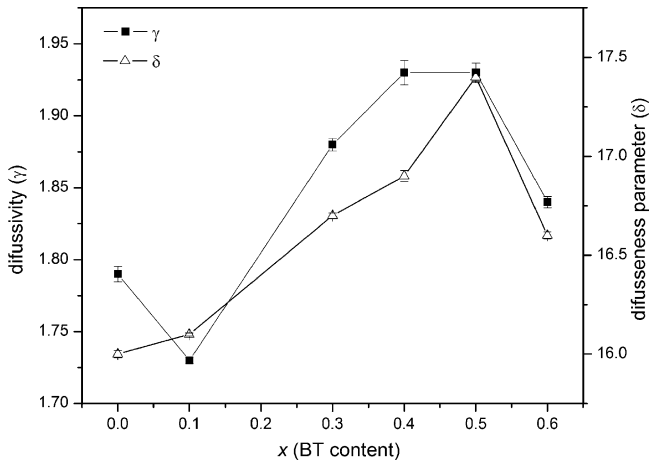

Fig. 8. Plots of diffusivity (γ) and diffuseness parameter (δ) for $(1-x)$PZT–xBT ceramics.

4. Conclusion

Phase formation characteristics of perovskite PZT–BT ceramics have been investigated for the whole series of compositions with XRD analysis. All compositions show complete solid solutions without unwanted phase. The crystal structure of $(1-x)$PZT–xBT system changes gradually from only tetragonal phase in BT to co-existence of tetragonal and rhombohedal phases with increasing PZT content. The (2 0 0)/(0 0 2) peak was found to split at $x = 0.6$ and the triplet peak appears with increasing PZT content. From XRD data, it can be seen that the possible range of compositions which corresponds to a phase transition is $0.6 < x < 0.7$. Lattice parameters and degree of tetragonality were found to vary with chemical composition and increase with decreasing PZT contents. The dielectric studies indicated that the phase transition behavior of the ceramic compositions becomes more diffuse with increasing BT content up to 50 mol%.

Acknowledgements

The authors would like to thank the financial support from the Thailand Research Fund (TRF), Faculty of Science and Graduate School of Chiang Mai University and the Ministry of University Affairs.

References

[1] G.H. Haertling, J. Am. Ceram. Soc. 82 (1999) 797–818.
[2] K. Uchino, Ferroelectric Devices, Marcel Dekker, New York, 2000, p. 308.
[3] B. Jaffe, W.R. Cook, Piezoelectric Ceramics, R.A.N. Publishers, 1971, p. 317.
[4] Y. Xu, Ferroelectric Materials and Their Applications, Elsevier Science Publishers B.V., 1991, p. 391.
[5] A.J. Moulson, J.M. Herbert, Electroceramics: Materials, Properties, Applications, John Wiley & Sons Ltd., Chichester, 2003, p. 500.
[6] J. Chen, Z. Shen, F. Liu, X. Liu, J. Yun, Scripta Mater. 49 (2003) 509–514.
[7] W. Chaisan, S. Ananta, T. Tunkasiri, Cur. Appl. Phys. 4 (2004) 182–185.
[8] B.K. Gan, J.M. Xue, D.M. Wan, J. Wang, Appl. Phys. A 69 (1999) 433–436.
[9] F. Xia, X. Yao, J. Mater. Sci. 34 (1999) 3341–3343.
[10] B.D. Cullity, Elements of X-ray Diffraction, Addison-Wesley Publishing Company, Inc., 1978, p. 32.
[11] D.G. Brandon, W.D. Kaplan, Microstructural Characterization of Materials, John Wiley & Sons, Ltd., 1999, p. 409.
[12] A.K. Arora, R.P. Tandon, A. Mansingh, Ferroelectrics 132 (1992) 9.
[13] P.G.R. Lucuta, F.L. Constantinescu, D. Barb, J. Am. Ceram. Soc. 68 (1985) 533–537.
[14] A. Boutarfaia, S.E. Bouaoud, Ceram. Int. 22 (1996) 281–286.
[15] L. Vegard, Z. Phys. 5 (1921) 17–26.
[16] A. Garg, D.C. Agrawal, Mater. Sci. Eng. B 56 (1999) 46–50.
[17] C.H. Wang, S.J. Chang, P.C. Chang, Mater. Sci. Eng. B 111 (2004) 124–130.
[18] J.-C. M'Peko, A.G. Peixoto, E. Jimenez, L.M. Gaggero-Sager, J. Electroceram. 15 (2005) 167–176.
[19] Z.R. Li, L.Y. Zhang, X. Yao, J. Mater. Res. 16 (2001) 834–836.
[20] L.E. Cross, Mater. Chem. Phys. 43 (1996) 108–115.
[21] R. Yimnirun, S. Ananta, P. Laoratanakul, Mater. Sci. Eng. B 112 (2004) 79–86.
[22] R.D. Shannon, C.T. Prewitt, Acta Crystallogr. B. Struct. Crystallogr. Cryst. Chem. 25 (1969) 925–945.
[23] A. Halliyal, U. Kumar, R.E. Newnham, L.E. Cross, Am. Ceram. Soc. Bull. 66 (1987) 671–676.
[24] N. Vittayakorn, G. Rujijanagul, X. Tan, M.A. Marquardt, D.P. Cann, J. Appl. Phys. 96 (2004) 5103–5109.
[25] R. Yimnirun, S. Ananta, P. Laoratanakul, J. Eur. Ceram. Soc. 25 (2005) 3235–3242.
[26] C.H. Tu, L.F. Chen, V.H. Schmidt, C.L. Tsai, Jpn. J. Appl. Phys. 40 (2001) 4118–4125.
[27] Z.Y. Cheng, R.S. Katiyar, X. Yao, A. Guo, Phys. Rev. B 55 (1997) 8165–8174.

Available online at www.sciencedirect.com
SCIENCE DIRECT®
Materials Letters 60 (2006) 2867–2872
materials letters
www.elsevier.com/locate/matlet

Effect of calcination conditions on phase formation and particle size of zinc niobate powders synthesized by solid-state reaction

A. Ngamjarurojana, O. Khamman, R. Yimnirun, S. Ananta *

Department of Physics, Faculty of Science, Chiang Mai University, Chiang Mai 50200, Thailand

Received 26 August 2005; accepted 2 February 2006
Available online 21 February 2006

Abstract

A columbite-like phase of zinc niobate, $ZnNb_2O_6$, has been synthesized by a solid-state reaction via a rapid vibro-milling technique. The formation of the $ZnNb_2O_6$ phase in the calcined powders has been investigated as a function of calcination conditions by TG–DTA and XRD techniques. Morphology, particle size and chemical composition have been determined via a combination of SEM and EDX techniques. It has been found that single-phase $ZnNb_2O_6$ powders were successfully obtained for calcination condition of 600 °C for 2 h or 550 °C for 6 h with heating/cooling rates of 30 °C/min. Clearly, this study has demonstrated the potentiality of a vibro-milling technique as a significant time-saving method to obtain single-phase $ZnNb_2O_6$ nanopowders (~50–300 nm) at low calcination temperature.

Keywords: Zinc niobate; $ZnNb_2O_6$; Columbite; Calcination; Phase formation; Powders; Solid-state reaction

1. Introduction

Zinc niobate ($ZnNb_2O_6$, ZN) is one of the binary niobate compounds with excellent dielectric properties at microwave frequencies [1–3]. It has very low loss and high dielectric constant and is a promising candidate for applications in microwave devices [4–6]. This compound with a columbite crystal structure is also a suitable reference material for investigating the defect induced in $LiNbO_3$ substrates for waveguide fabrication [6,7]. Moreover, recently, it is well established as the key precursor for the successful preparation of single-phase ferroelectric perovskite $Pb(Zn_{1/3}Nb_{2/3})O_3$ (PZN)-based ceramics, which is becoming increasingly important for actuator, transducer and ultrasonic motor applications [8,9].

There has been a great deal of interest in the preparation of single-phase PZN powders as well as in the sintering and piezoelectric properties of PZN-based ceramics [10–14]. In general, the constituents ZnO and Nb_2O_5 are first mixed and reacted together to form zinc niobate ($ZnNb_2O_6$), prior to mixing and reacting with PbO in the second step of calcination at elevated temperature. Interestingly, this mixed oxide route has been employed with minor modifications in the synthesis of $ZnNb_2O_6$ itself [10–12]. However, powders prepared by a mixed oxide route have spatial fluctuations in their compositions. The extent of the fluctuation depends on the characteristics of the starting powders as well as on the processing schedule. Generally, the mixed oxide method involves the heating of a mixture of zinc oxide and niobium oxide above 900 °C for long times i.e. 2 h [2,5,13], 4 h [12,14], 6 h [15] and 8 h [16]. The optimization of calcination conditions used in the mixed oxide process, however, has not received detailed attention, and the effects of applied dwell time and heating/cooling rates have not yet been studied extensively.

Therefore, the main purpose of this work was to explore a simple mixed oxide synthetic route for the production of $ZnNb_2O_6$ (ZN) powders via a rapid vibro-milling technique and to perform a systematic study of the reaction between the starting zinc oxide and niobium oxide precursors. The phase formation and morphology of the powder calcined at various conditions will be studied and discussed. The rapid vibro-milling technique was employed to explore the potentiality in obtaining nano-sized powders, which would in turn lead to lower required firing temperature.

* Corresponding author. Tel.: +66 53 943367; fax: +66 53 943445.
E-mail address: Supon@chiangmai.ac.th (S. Ananta).

0167-577X/$ - see front matter © 2006 Elsevier B.V. All rights reserved.
doi:10.1016/j.matlet.2006.02.004

2. Experimental procedure

The starting materials were commercially available zinc oxide, ZnO (Fluka Chemical, 99.9% purity) (JCPDS file number 89-1397) and niobium oxide, Nb_2O_5 (JCPDS file number 30-873) (Aldrich, 99.9% purity). The two oxide powders exhibited an average particle size in the range of 3.0–5.0 μm. $ZnNb_2O_6$ powders were synthesized by the solid-state reaction of thoroughly ground mixtures of ZnO and Nb_2O_5 powders that were milled in the required stoichiometric ratio. Instead of employing a ball-milling procedure [1,13–15], a McCrone vibro-milling technique was used [17]. In order to combine mixing capacity with a significant time saving, the milling operation was carried out for 0.5 h with corundum cylindrical media in isopropyl alcohol (IPA). After drying at 120 °C for 2 h, the reaction of the uncalcined powders taking place during heat treatment was investigated by themogravimetric and differential thermal analysis (TG–DTA, Shimadzu), using a heating rate of 10 °C/min in air from room temperature up to 1000 °C. Based on the TG–DTA results, the mixture was calcined at various conditions, i.e. temperatures ranging from 500 to 900 °C, dwell times ranging from 0.5 to 8 h and heating/cooling rates ranging from 5 to 30 °C /min, in closed alumina crucible, in order to investigate the formation of zinc niobate.

Calcined powders were subsequently examined by room temperature X-ray diffraction (XRD; Siemens-D500 diffractometer), using Ni-filtered CuK_α radiation to identify the phases formed and optimum calcination conditions for the formation of ZN powders. Powder morphologies and particle sizes were directly imaged, using scanning electron microscopy (SEM; JEOL JSM-840A). The chemical compositions of the phase formed were elucidated by an energy-dispersive X-ray (EDX) analyzer with an ultra-thin window. EDX spectra were quantified with the virtual standard peaks supplied with the Oxford Instruments eXL software.

3. Results and discussion

The TG–DTA simultaneous analysis of a powder mixed in the stoichiometric proportions of $ZnNb_2O_6$ is displayed in Fig. 1. In the temperature range from room temperature to ~200 °C, the sample shows both exothermic and endothermic peaks in the DTA curve, consistent with the first weight loss. These observations can be attributed to the decomposition of the organic species from the milling process [17,18]. Increasing the temperature up to ~1000 °C, the solid-state reaction occurred between ZnO and Nb_2O_5 [2,5,13]. The broad exotherm with several small peaks in the DTA curve represents that reaction, which has a maximum at ~550 and 800 °C. These are supported by a second fall in sample weight over the same temperature range. However, it is to be noted that there is no obvious interpretation of these peaks, although it is likely to correspond to a phase transition reported by a number of workers [13–16]. These data were used to define the range of calcination temperatures for XRD investigation between 500 and 900 °C.

To further study the phase development with increasing calcination temperature in the powders, they were calcined for 2 h in air at various temperatures, up to 900 °C, followed by phase analysis using XRD. As shown in Fig. 2, for the uncalcined powder, only X-ray peaks of precursors ZnO (○) and Nb_2O_5 (●), which could be matched with JCPDS file numbers 89-1397 [19] and 3-873 [20], respectively, are present, indicating that no reaction had yet been triggered during the milling process. It is seen that fine $ZnNb_2O_6$ crystallites (▽) were developed in the powder at a calcination temperature as low as 500 °C, accompanying with ZnO and Nb_2O_5 as separated phases. This observation agrees well with those derived from the TG–DTA results and other workers [13,16]. As the temperature increased to 550 °C, the intensity of the columbite-like $ZnNb_2O_6$ peaks was further enhanced and became the predominant phase. Upon calcination at 600 °C, an essentially monophasic of $ZnNb_2O_6$ phase is obtained. This ZN phase was indexable according to an orthorhombic columbite-type structure with lattice parameters a=1426 pm, b=572 pm and c=504 pm, space group *Pbcn* (no. 60), in consistent with JCPDS file numbers 76-1827 [21]. This study also shows that orthorhombic ZN crystallite is the only detectable phase in the powders, after calcination in the range of

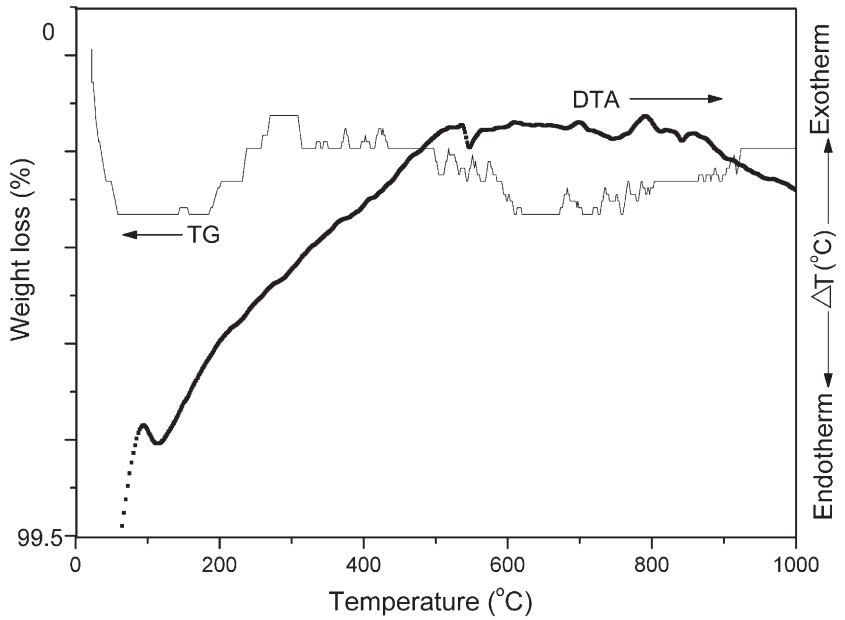

Fig. 1. TG–DTA curves for the mixture of ZnO–Nb_2O_5 powder.

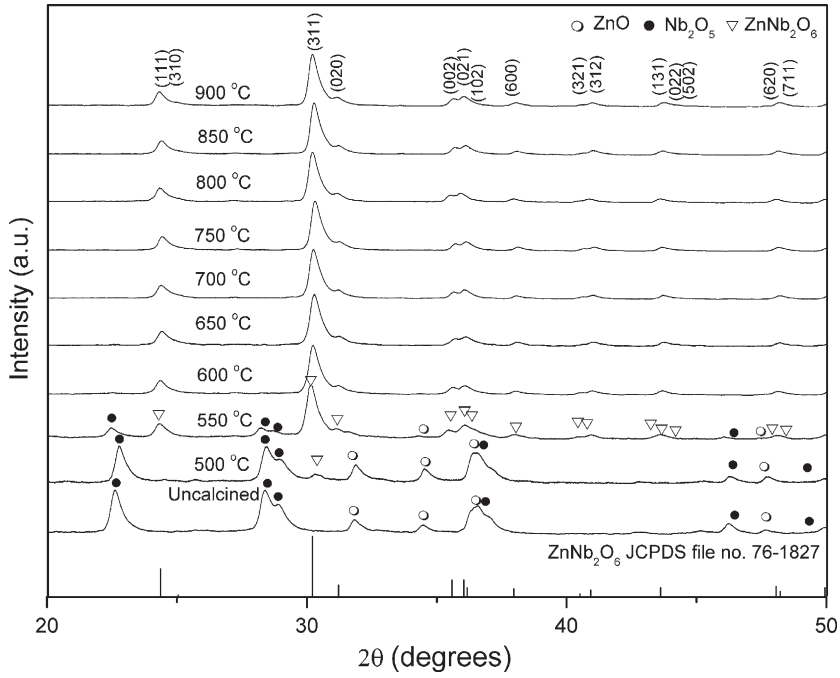

Fig. 2. XRD patterns of ZN powders calcined at various temperatures for 2 h with heating/cooling rates of 10 °C/min.

600–900 °C. In earlier works [12–16], long heat treatments at ~900–1000 °C for 2–8 h were proposed for the formation of $ZnNb_2O_6$ by a conventional mixed oxide synthetic route, although no details on phase formation were provided. However, in the present study, it was found that there are no significant differences between the powders calcined at 600 to 900 °C with dwell time of only 2 h, as shown in Fig. 2. This observation would clearly suggest the advantages of a rapid vibro-milling technique used in the present study.

Apart from the calcination temperature, the effect of dwell time was also found to be quite significant. From Fig. 3, it can be seen that the single phase of $ZnNb_2O_6$ (yield of 100% within the limitations of the XRD technique) was found to be possible in powders calcined at 600 °C with dwell time of 2 h or more. For the present work, there are no significant differences between the powders calcined at 600 °C with dwell times ranging from 2 to 8 h. This was apparently a consequence of the enhancement in crystallinity of the $ZnNb_2O_6$ phase with increasing dwell time. The appearance of ZnO and Nb_2O_5 phases indicated that full crystallization has not occurred at relatively short calcination times. However, in the work reported here, it is to be noted that single phase of $ZnNb_2O_6$ powder was also successfully obtained for a calcination temperature of 550 °C with dwell time of at least 6 h applied (Fig. 4). This is probably due to the effectiveness of vibro-milling and a carefully optimized reaction. The observation that the dwell time effect may also play an important role in obtaining a single-

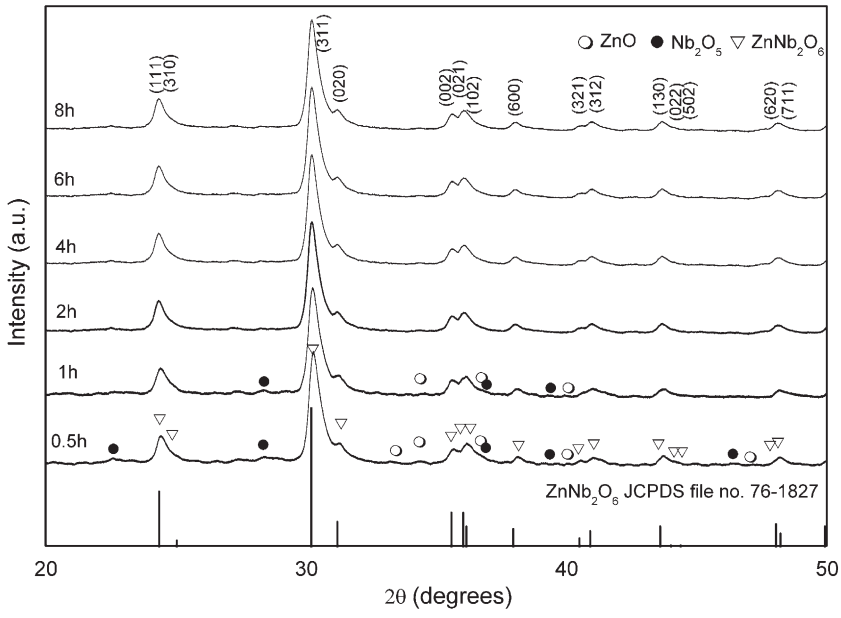

Fig. 3. XRD patterns of ZN powders calcined at 600 °C with heating/cooling rates of 10 °C/min for various dwell times.

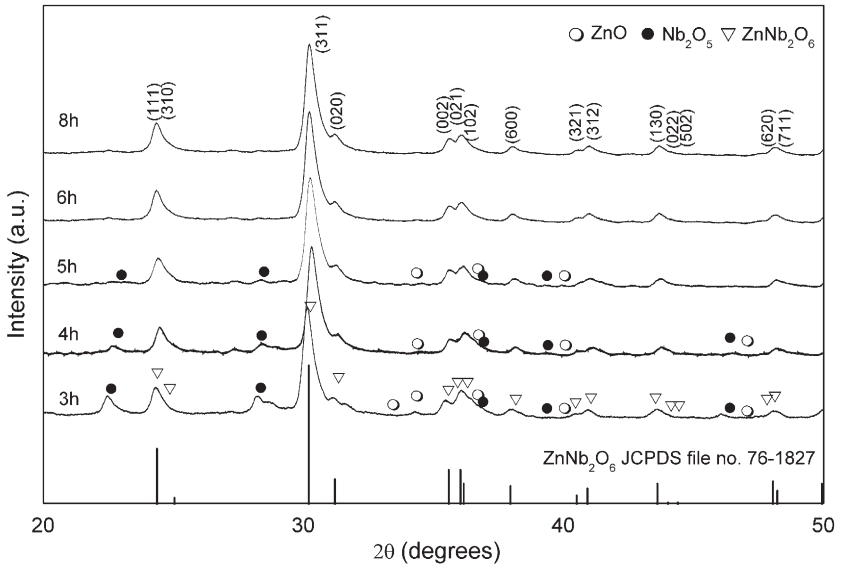

Fig. 4. XRD patterns of ZN powders calcined at 550 °C with heating/cooling rates of 10 °C/min for various dwell times.

phase columbite product is also consistent with other similar systems [22,23]. It is also very interesting to see that the on-set temperature is approximately 300–400 C lower than those reported earlier with a conventional ball-milling method [12–15]. The difference could be attributed to nano-sized mixed powders obtained from a rapid vibro-milling. Most importantly, this study suggests that a rapid vibro-milling method can significantly lower the optimum calcination temperature for formation of single-phase ZN powders.

In the present study, an attempt was also made to calcine ZN powders under various heating/cooling rates (Fig. 5). In this connection, it is shown that the yield of $ZnNb_2O_6$ phase did not vary significantly with different heating/cooling rates, ranging from 5 to 30 C/min, in good agreement with early results reported for the mixture of the two kinds of refractory oxides [17,23].

Based on the TG–DTA and XRD data, it may be concluded that, over a wide range of calcination conditions, single-phase $ZnNb_2O_6$ cannot be straightforwardly formed via a solid-state mixed oxide synthetic route, unless a careful design of calcination is performed. It is well documented that powders prepared by a conventional mixed oxide method have spatial fluctuations in their compositions. The extent of the fluctuation depends on the characteristics of the starting powders as well as the processing schedules [13,16,22]. The experimental work carried out here suggests that the optimal calcination conditions for single-phase $ZnNb_2O_6$ (with impurities undetected by XRD technique) is 600 °C for 2 h or 550 °C for 6 h, with heating/cooling rates as fast as 30 °C/min. Moreover, the formation temperature and dwell time for the production of $ZnNb_2O_6$ powders observed in this work are also much lower than those reported earlier [14–16]. This clearly emphasizes the advantages of a rapid vibro-milling technique.

Finally, the morphological changes in the $ZnNb_2O_6$ powders formed by a mixed oxide are illustrated in Fig. 6(a–f) as a function of calcination temperatures, dwell times and heating/cooling rates,

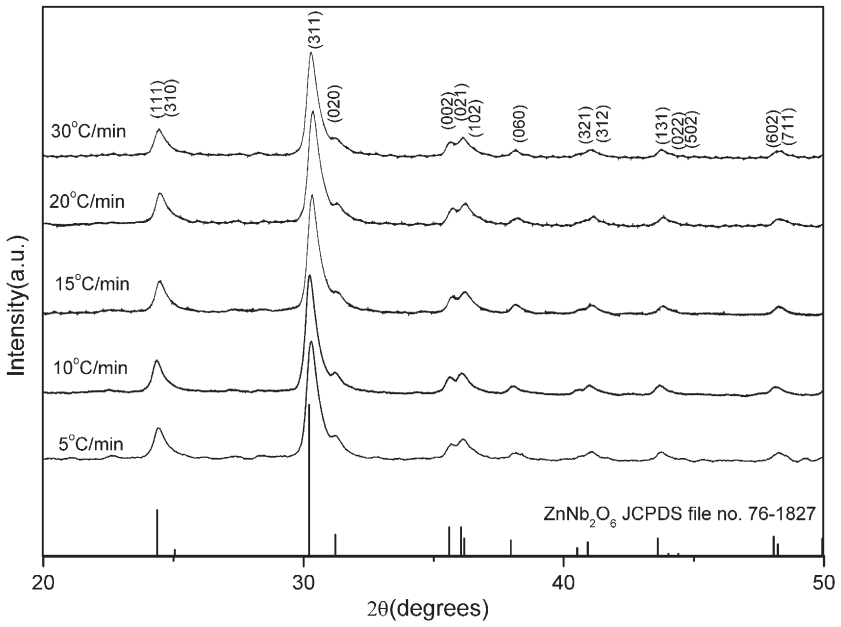

Fig. 5. XRD patterns of ZN powders calcined at 600 °C for 2 h with various heating/cooling rates.

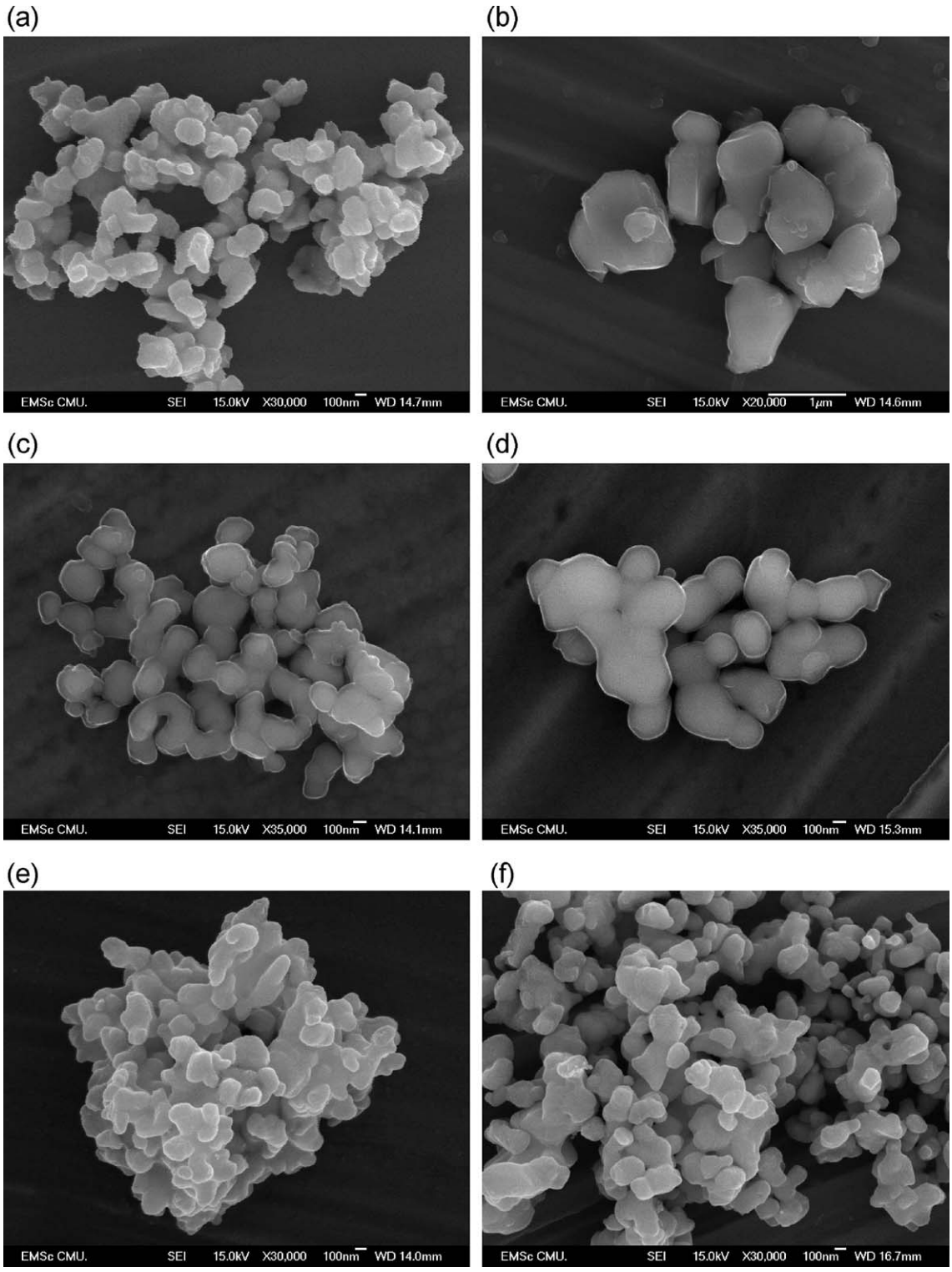

Fig. 6. SEM micrographs of the ZN powders calcined for 2 h with heating/cooling rates of 10 °C/min at (a) 600, (b) 900, and at 600 °C with heating/cooling rates of 10 °C/min for (c) 4, (d) 8 h, and at 600 °C for 2 h with heating/cooling rates of (e) 10 and (f) 30 °C/min.

respectively. The influence of calcination conditions on particle size is given in Table 1. In general, the particles are agglomerated and irregular in shape, with a substantial variation in particle size, particularly in samples calcined at high temperature (Fig. 6(b)) or with fast heating/cooling rates (Fig. 6(e,f)). This finding is also similar to that in $ZrTiO_4$ powders synthesized by Ananta et al. [17]. The results indicate that difference in particle size and degree of agglomeration tend to increase with calcination temperatures (Table 1). After calcinations at 900 °C (Fig. 6(b)), the powders seem to display a significant level of necking and bonding as if they were in the initial stages of sintering.

The effects of dwell time and heating/cooling rates on the morphology of the calcined powders were also found to be quite significant. As

Table 1
Particle size range of $ZnNb_2O_6$ powders calcined at various conditions

Calcination conditions			Particle size range (±10 nm)
Temperature (°C)	Dwell time (h)	Rates (°C/min)	
550	6	30	92–320
600	2	10	75–220
600	4	10	80–340
600	6	10	120–400
600	8	10	180–620
600	2	20	70–220
600	2	30	50–300
700	2	10	120–250
800	2	10	150–420
900	2	10	300–800

expected, it is seen that longer heat treatment leads to larger particle sizes and hard agglomeration (Fig. 6(c,d)). As shown in Fig. 6(e,f), by increasing the heating/cooling rates, averaged particle size tends to decrease whilst the degree of agglomeration tends to increase. This observation could be attributed to the mechanism of surface energy reduction of the ultrafine powders, i.e. the smaller the powder the higher the specific surface area [24]. To the author's knowledge, the present data are the first results for the morphology–calcination relationship of $ZnNb_2O_6$ powders prepared by the solid-state reaction. It is also of interest to point out that mass production of single-phase $ZnNb_2O_6$ nanopowders with the smallest particle size ~50 nm (estimated from SEM micrographs) can be achieved by employing a simple solid-state reaction combined with a rapid vibro-milling technique. In addition, EDX analysis using a 20 nm probe on a large number of particles of the calcined powders confirms that the parent composition is $ZnNb_2O_6$ powders, in good agreement with XRD results.

The results obtained in this study clearly suggest that a systematic study of the effect of milling parameters such as milling times and milling speed on the phase and morphology evolutions of the $ZnNb_2O_6$ powders are required for better understanding and verifying the attractiveness of the vibro-milling technique. Further investigation of this relationship is underway and will be reported in the future.

4. Conclusions

The solid-state mixed oxide method via a rapid vibro-milling technique is explored in the preparation of single phase ZN nanopowders. The calcination temperature and dwell time have been found to have a pronounced effect on phase formation and particle size of the calcined $ZnNb_2O_6$ powders. This work demonstrated that single-phase of zinc niobate powders with particle size ranging from 50–300 nm can be produced via this technique by using a calcination temperature of 600 °C for 2 h or 550 C for 6 h, with heating/cooling rates of 30 C/min. The resulting ZN powders consist of variety of agglomerated particle sizes, depending on calcination conditions.

Acknowledgements

We thank the Thailand Research Fund (TRF), Graduate School and Faculty of Science, Chiang Mai University, and Ministry of University Affairs of Thailand for all support.

References

[1] R.C. Pullar, J.D. Breeze, N.M. Alford, J. Am. Ceram. Soc. 88 (2005) 2466.
[2] H.J. Lee, S.J. Kim, I.T. Kim, Mater. Res. Bull. 32 (1997) 847.
[3] D.W. Kim, K.H. Ko, K.S. Hong, J. Am. Ceram. Soc. 84 (2001) 1286.
[4] Y.C. Zhang, Z.X. Yue, X. Qi, B. Li, Z.L. Gui, L.T. Li, Mater. Lett. 58 (2004) 1392.
[5] Y.C. Zhang, L.T. Li, Z.X. Yue, Z.L. Gui, Mater. Sci. Eng., B, Solid-State Mater. Adv. Technol. 99 (2003) 282.
[6] A.Z. Simoes, A.H.M. Gonzalez, A.A. Cavalheiro, M.A. Zaghete, B.D. Stojanovic, J.A. Varela, Ceram. Int. 28 (2002) 265.
[7] C. Zaldo, M.J. Martin, C. Coya, K. Polgar, A. Peter, J. Paitz, J. Phys., Condens. Matter 7 (1995) 2249.
[8] Y. Xu, Ferroelectric Materials and Their Applications, Elsevier Science, Amsterdam, The Netherlands, 1991.
[9] A.J. Moulson, J.M. Herbert, Electroceramics, 2nd ed.Wiley, New York, 2003.
[10] Y. Hou, M.K. Zhu, H. Wang, B. Wang, H. Yan, C.S. Tian, Mater. Lett. 58 (2004) 1508.
[11] W. Zhu, A.L. Kholkin, P.Q. Mantas, J.L. Baptista, J. Am. Ceram. Soc. 84 (2001) 1740.
[12] M. Villegas, A.C. Caballero, C. Moure, P. Durán, J.F. Fernández, R.E. Newnham, J. Am. Ceram. Soc. 83 (2000) 141.
[13] N. Vittayakorn, G. Rujijanagul, T. Tunkasiri, X. Tan, D.P. Cann, Mater. Sci. Eng., B, Solid-State Mater. Adv. Technol. 108 (2004) 258.
[14] X.J. Lu, X.M. Chen, J. Electroceram. 7 (2001) 127.
[15] C.L. Li, C.C. Chou, Int. Ferro. 55 (2003) 955.
[16] L.B. Kong, J. Ma, H. Huang, R.F. Zhang, T.S. Zhang, J. Alloys Compd. 347 (2002) 308.
[17] S. Ananta, R. Tipakontitikul, T. Tunkasiri, Mater. Lett. 57 (2003) 2637.
[18] S. Ananta, Mater. Lett. 58 (2004) 2834.
[19] Powder Diffraction File No. 89-1397. International Centre for Diffraction Data, Newton Square, PA, 2000.
[20] Powder Diffraction File No. 3-873. International Centre for Diffraction Data, Newton Square, PA, 2000.
[21] Powder Diffraction File No. 76-1827. International Centre for Diffraction Data, Newton Square, PA, 2000.
[22] S. Ananta, R. Brydson, N.W. Thomas, J. Eur. Ceram. Soc. 20 (2000) 2325.
[23] S. Ananta, Mater. Lett. 58 (2004) 2781.
[24] J.S. Reed, Principles of Ceramic Processing, 2nd ed.Wiley, New York, 1995.

International Journal of Modern Physics B
Vol. 20, No. 23 (2006) 3409–3417

World Scientific
www.worldscientific.com

CONTRIBUTIONS OF DOMAIN-RELATED PHENOMENA ON DIELECTRIC CONSTANT OF LEAD-BASED FERROELECTRIC CERAMICS UNDER UNIAXIAL COMPRESSIVE PRE-STRESS

RATTIKORN YIMNIRUN

Department of Physics, Faculty of Science, Chiang Mai University, Chiang Mai 50200, Thailand
rattikornyimnirun@yahoo.com

Received 15 February 2006

The dielectric constant of lead-based ferroelectric ceramics in three different systems, i.e. BT-PZT, PMN-PT and PMN-PZT, was measured under uniaxial compressive pre-stress to investigate the contributions of different domain-phenomena. The dielectric constant was observed at room temperature under the compressive pre-stress up to 15 MPa, 22 MPa and 5 MPa for BT-PZT, PMN-PT and PMN-PZT, respectively, using a homebuilt uniaxial compressometer. Dielectric constant of the BT-PZT ceramics increased significantly with increasing applied stress. Larger changes in the dielectric constant with the applied stress were observed in the PZT-rich compositions. However, for PMN-PT and PMN-PZT ceramic systems, changes in the dielectric constant with the stress were found to depend significantly on the ceramic compositions. The experimental results could be explained by both intrinsic and extrinsic domain-related mechanisms involving domain wall motions, as well as the de-aging phenomenon from the application of the compressive pre-stress. Roles of different types of domains, i.e. micro-domains and nano-domains, were also discussed.

Keywords: Domains; dielectric properties; ferroelectrics; uniaxial stress.

1. Introduction

Among perovskite ferroelectric materials, barium titanate ($BaTiO_3$ or BT), lead titanate ($PbTiO_3$ or PT), lead zirconate titanate ($Pb(Zr_{1-x}Ti_x)O_3$ or PZT) and lead magnesium niobate ($Pb(Mg_{1/3}Nb_{2/3})O_3$ or PMN) ceramics have been investigated extensively and continuously since the late 1940s.[1–4] BT and PT, PMN and PZT are representative perovskite normal ferroelectrics, relaxor ferroelectrics, and piezoelectric prototypes, respectively, because of their excellent electrical properties. These ceramics possess distinct characteristics that make each of them suitable for different applications. Forming a composite of these ferroelectrics has been one of the techniques employed to improve the properties of ferroelectric ceramics for specific requirements for each application.[2–4]

One of the most studied piezoelectric compounds, $Pb(Zr_{0.52}Ti_{0.48})O_3$, a morphotropic phase boundary (MPB) compound of PZT, has great piezoelectric properties with a high Curie temperature (T_C) of ∼390°C. BT exhibits high dielectric constant and superior electrostrictive responses with a lower T_C (∼120°C).[1–4] In addition, BT is mechanically superior to PZT, whereas PZT ceramics can be easily sintered at temperatures much lower than that in BT ceramics, which usually require as high sintering temperature as 1400°C.[5] With their complementary features, the composites between PZT and BT are expected to exhibit better properties than the single-phase PZT and BT.[1–3] Furthermore, the properties can also be tailored over a wider range by changing the compositions to meet the strict requirements for specific applications.[3–6]

PMN exhibits high dielectric constant and a broad range transition of dielectric constant, with temperature as a function of frequency.[3,6] In addition, PMN ceramics exhibit low loss and non-hysteretic characteristics. These make PMN a good candidate for a large number of applications, such as multilayer capacitors, sensors and actuators. However, it is difficult to form a single-phase PMN. It is widely accepted that forming a solid solution between PMN and PT results in ceramics with high dielectric constant and large electrostrictive coefficients.[7–9] In addition, PMN ceramics have relatively low electromechanical coupling coefficients, when compared with those of PZT, which are found in several actuator and transducer applications due to the latter's high electromechanical coupling coefficients and higher temperature of operation.[1,4] However, PZT ceramics also possess highly hysteretic behavior, which makes them unsuited for applications that require high delicacy and reliability. Furthermore, PZT ceramics normally have very high Curie temperature (T_C) in the vicinity of 400°C.[1,2] Usually many applications require that T_C be close to ambient temperature. Therefore, there is a general interest to reduce the T_C of PZT ceramics to optimize their uses. With the complementary features of PMN and PZT, the composites between PMN and PZT are expected to synergetically combine the properties of both ceramics, which could exhibit more desirable piezoelectric and dielectric properties for several technologically demanding applications than single-phase PMN and PZT.[10,11] With the reasons outlined above, it is therefore of interest to investigate the PMN-PT and PMN-PZT systems.

In many applications, these ferroelectric ceramics are often subjected to mechanical loading, either deliberately in the design of the device itself or because the device is used to change shapes as in many smart structure applications or when the device is used under environmental stresses.[6,12,13] Despite the fact, material constants used in any design calculations are often obtained from a stress-free measuring condition, which in turn, may lead to incorrect or inappropriate actuator and transducer designs. It is therefore important to determine the properties of these materials as a function of applied stress. Previous investigations on the stress-dependent dielectric and electrical properties of many ceramic systems have clearly emphasized the importance of the matter.[14,15] More importantly, since these

three ceramic systems possess very distinct dielectric characteristics, they display significantly different ranges of Curie temperature (T_C). BT-PZT has a range of T_C between 120°C and 400°C,[16] while the range extends from −10°C to 490°C for PMN-PT[7–9] and from −10°C to 400°C for PMN-PZT.[17,18] The experimental results of the uniaxial stress dependence of the room temperature dielectric properties of these ceramic systems will provide a tool in assessing the contributions of different domain-related mechanisms in these important ferroelectrics. Therefore, this study is undertaken to investigate the influences of the uniaxial compressive pre-stress on the dielectric properties of ceramics in BT-PZT, PMN-PT and PMN-PZT systems.

2. Materials and Methods

The ceramic composites with formula $BaTiO_3$–$Pb(Zr_{0.52}Ti_{0.48})O_3$ or BT-PZT, $Pb(Mg_{1/3}Nb_{2/3})O_3$–$PbTiO_3$ or PMN-PT and $Pb(Mg_{1/3}Nb_{2/3})O_3$–$Pb(Zr_{0.52}Ti_{0.48})O_3$ or PMN-PZT were prepared from the starting BT, PT, PZT and PMN powders by a mixed-oxide method. BT, PT and PZT powders were first prepared by a conventional mixed-oxide method. On the other hand, perovskite-phase PMN powders were obtained via a well-known columbite method.[19] Subsequently, the $(x)BaTiO_3$–$(1–x)Pb(Zr_{0.52}Ti_{0.48})O_3$ (when x = 0.0, 0.05, 0.15, 0.25, 0.35, 0.45, 0.55, 0.65, 0.75, 0.85, 0.95, and 1.0), the $(1-x)Pb(Mg_{1/3}Nb_{2/3})O_3$–$(x)Pb(Zr_{0.52}Ti_{0.48})O_3$ (when x = 0.1, 0.2, 0.3, 0.4, and 0.5) and the $(x)Pb(Mg_{1/3}Nb_{2/3})O_3$–$(1–x)Pb(Zr_{0.52}Ti_{0.48})O_3$ (when x = 0.0, 0.1, 0.3, 0.5, 0.7, 0.9, and 1.0) ceramic composites were then prepared from the starting BT, PT, PZT and PMN powders by the similar mixed-oxide method described above at various processing conditions. The detailed descriptions of powders and ceramics processing and characterizations were presented thoroughly in the earlier publications.[16–18]

For dielectric property characterizations, the sintered samples were lapped to obtain parallel faces, and the faces were then coated with silver paint as electrodes. The samples were heat-treated at 750°C for 12 min to ensure the contact between the electrodes and the ceramic surfaces. The samples were subsequently poled in a silicone oil bath at a temperature of 120°C by applying a dc field of 20 kV/cm for 30 min for BT-PZT ceramics, while for PMN-PT and PMN-PZT ceramics, the poling condition was 25 kV/cm for 30 min and field-cooled to room temperature. To study the effects of the uniaxial compressive pre-stress on the dielectric properties, the uniaxial compressometer was constructed. The uniaxial compressive pre-stress applied parallel to the electric field direction was supplied by the servohydraulic load frame and the applied stress was monitored with the pressure gauge of the load frame. The details of the system were described elsewhere.[20,21] The dielectric properties were measured through spring-loaded pins connected to the LCZ-meter (Hewlett Packard, Model 4276A). The capacitance was determined at a frequency of 1 kHz and room temperature (25°C). The dielectric constant was then calcu-

lated from a parallel-plate capacitor equation, e.g. $\varepsilon_r = Cd/\varepsilon_0 A$, where C is the capacitance of the sample, d and A are the thickness and the area of the electrode, respectively, and ε_0 is the dielectric permittivity of vacuum (8.854×10^{-12} F/m).

3. Results and Discussion

The experimental results of the uniaxial compressive pre-stress dependence of the dielectric constant of the ceramics in BT-PZT, PMN-PT and PMN-PZT systems are displayed in Figs. 1–3. For BT-PZT system (Fig. 1), there is a significant change of the dielectric constant of the ceramics when the applied stress increases from 0 MPa to 15 MPa. The changes of the dielectric constant with the applied stress can be divided into three different groups. For PZT ceramic, the dielectric constant increases exponentially with the applied stress. It can be seen that the dielectric constant is enhanced by approximately 8% at 15 MPa applied stress. For PZT-rich compositions (0.05BT-0.95PZT, 0.15BT-0.85PZT, 0.25BT-0.75PZT, 0.35BT-0.65PZT and 0.45BT-0.55PZT), the dielectric constant increases rather linearly with increasing applied stress. The changes in the dielectric constant between 2% to 4% at 15 MPa applied stress are obviously smaller than that observed in PZT. For BT-rich compositions (BT, 0.95BT-0.05PZT, 0.85BT-0.15PZT, 0.75BT-0.25PZT and 0.65BT-0.35PZT), the dielectric constant only rises slightly ($< 2\%$) and in

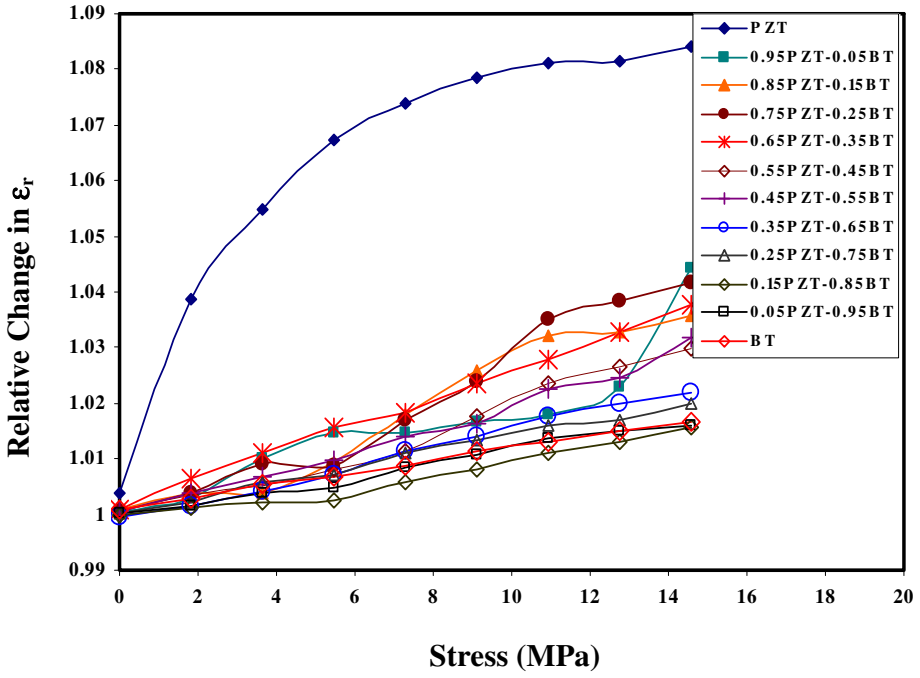

Fig. 1. Relative changes of dielectric constant (ε_r) as a function of compressive pre-stress for (x)BT–(1–x)PZT ceramics.

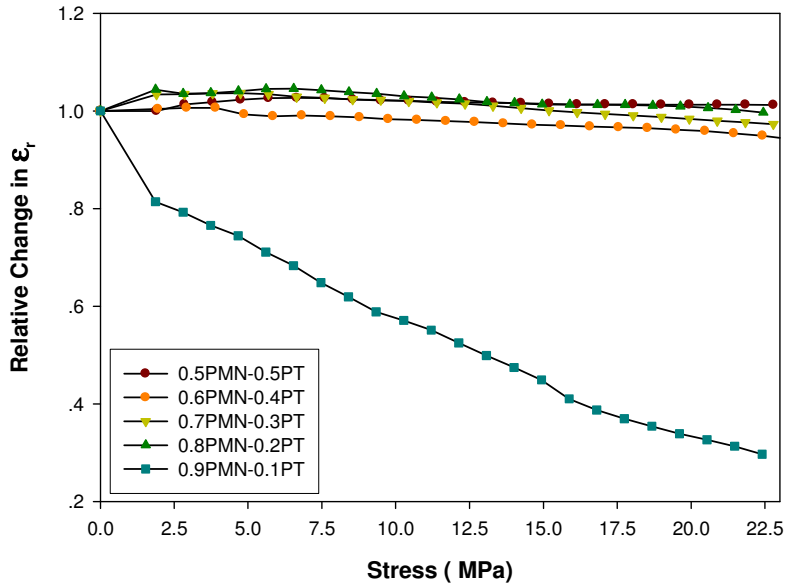

Fig. 2. Relative changes of dielectric constant (ε_r) as a function of compressive pre-stress for (x)PT–(1–x)PMN ceramics.

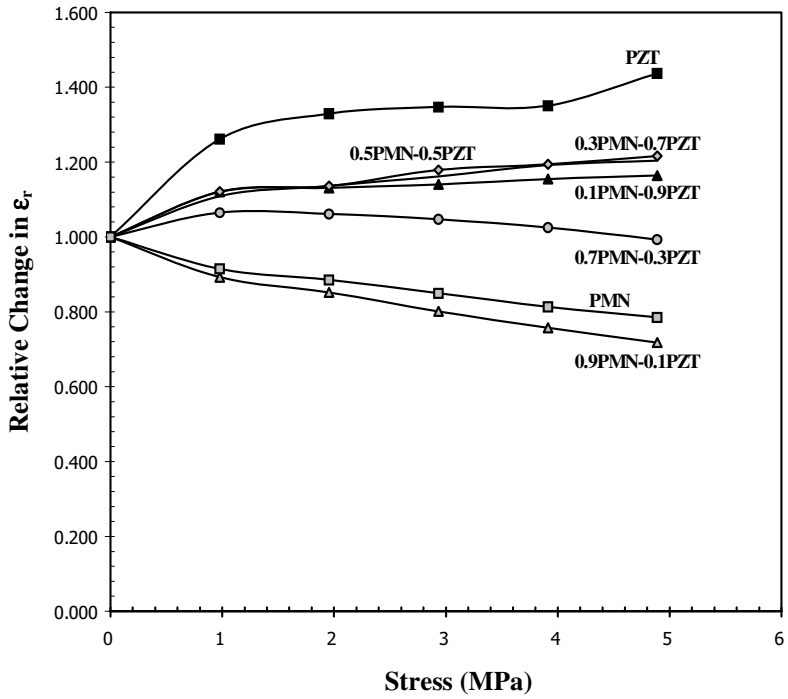

Fig. 3. Relative changes of dielectric constant (ε_r) as a function of compressive pre-stress for (x)PMN–(1–x)PZT ceramics.

a linear manner when the applied stress increases to the maximum amplitude. Similar experimental results have been reported previously for soft PZT[22,23] in which the dielectric properties are found to increase with increasing magnitude of the compressive pre-stress.

The experimental result for the PMN-PT ceramics is shown in Fig. 2. The changes of the dielectric constant with the applied stress can be divided into two groups. For 0.9PMN-0.1PT ceramic, the dielectric constant decreases drastically with the applied stress. The change is more than 70% decrease when the applied stress increases to 22 MPa. On the other hand, for other PMN-PT ceramics, i.e. with x values of 0.2–0.5, the change is minimal. The dielectric constant is actually rather stable within this range of the applied stress.

Figure 3 displays the experimental results for the PMN-PZT ceramics. To prevent mechanical failures usually occurring in PMN-PZT, the experiments are carried out at the compressive pre-stress only up to 5 MPa. However, there is already a significant change of the dielectric constant of the ceramics; even the maximum applied stress is only 5 MPa. The changes of the dielectric constant with the compressive pre-stress can be divided into two different groups. For PMN-rich compositions (PMN, 0.9PMN-0.1PZT, and 0.7PMN-0.3PZT), the dielectric constant generally decreases with increasing applied stress. However, it should be noticed that only PMN and 0.9PMN-0.1PZT compositions show definite decreases in the dielectric constant, while the dielectric constant of the 0.7PMN-0.3PZT composition initially increases, then decreases with very little difference in the dielectric constant between 0 MPa and 5 MPa. On the other hand, for PZT-rich compositions (PZT, 0.1PMN-0.9PZT, 0.3PMN-0.7PZT, and 0.5PMN-0.5PZT), the dielectric constant rises slightly when the compressive pre-stress increases from 0 MPa to 1 MPa, and becomes relatively constant when the pre-stress increases further.

To understand these experimental results, various effects will have to be considered. Normally, the properties of ferroelectric materials are derived from both the intrinsic contribution, which is the response from a single domain, and extrinsic contributions, which are from domain wall motions.[14,15,24–26] Intrinsically, these ferroelectric materials consist of different types of domains, depending upon composition and temperature. In normal ferroelectrics such as BT, PT and PZT, the domains called "micro-domain" are present when the temperature is below T_C, and the domains are non-existent above T_C. On the other hand, in a relaxor ferroelectric like PMN, the domain size gradually changes from nano-domain to micro-domain when the temperature decreases from far above temperature with maximum dielectric constant ($T_{\max}$) to below depolarization temperature (T_d).[6] Normally, the responses of nano-domains to the external compressive pre-stress result in the decrease in the dielectric constant with stress.[26] The extrinsic contribution is also very important. When a mechanical stress is applied to a ferroelectric material, the domain structure in the material will change to maintain the domain energy at a minimum; during this process some of the domains engulf other domains or change shape irreversibly. Under a uniaxial stress, the domain structure of ferroelectric

ceramics may undergo domain switching, clamping of domain walls, de-aging and de-poling.[25]

For the case of BT-PZT system, which exhibits normal ferroelectric behavior,[16] the results on the uniaxial compressive pre-stress dependence of the dielectric constant can easily be explained with the contribution from the extrinsic contribution because the range of T_C for these ceramics is far above the room temperature, at which the experiment was carried out. Therefore, the main contribution is from micro-domains and the domain walls. When the uniaxial compressive pre-stress is applied in the direction parallel to the poling direction, the stress will move some of the polarization away from the poling direction, resulting in a change in domain structures.[14,24,25] This change increases the non-180° domain wall density. Hence, the increase of the dielectric constant with the applied stress can be observed. The de-aging mechanism is also expected to play a role here. However, the stress clamping of domain walls and the de-poling mechanisms are not expected at this relatively-low stress level used in this study.[27] Therefore, a combination of the domain switching and the de-aging mechanism is believed to be a reason for the increase of the dielectric constant with increasing applied stress in the BT-PZT system, as shown in Fig. 1.

The situation for the PMN-PT system is a little more complex because this system is a mixing between the normal ferroelectric PT and the relaxor ferroelectric PMN. Therefore, there is a competing mechanism between the two types of materials, depending on temperature and composition. Since the $T_{\max}$ for 0.9PMN-0.1PT is ∼30°C[3,7−9] and the experiment was performed at ∼25°C, the nano-domains contribute greatly to the dielectric response; hence a significant decrease in dielectric constant with increasing stress is observed. For other compositions with higher $T_{\max}$ (110°C for 0.8PMN-0.2PT to 270°C for 0.5PMN-0.5PT),[7−9] since there are competing influences of the intrinsic contribution of domains, mainly micro-domains, and the extrinsic contribution of re-polarization and growth of micro-polar regions, with opposite responses, the dielectric constant of these compositions becomes rather stable with increasing applied stress, as seen in Fig. 2.

For the PMN-PZT system, the results for the case of PZT-rich compositions can easily be explained in the same way as in the BT-PZT system. Since PMN is a relaxor ferroelectric material, the situation is very different for PMN-rich compositions. The stress dependence of the dielectric constant of the compositions is attributed to competing influences of the domain contribution and the extrinsic contribution of re-polarization and growth of micro-polar regions.[14,27] Since the dielectric response of both contributions is affected by the applied stress in an opposite way, the behavior of the composites depends on the composition ratio between PMN and PZT. Since the measurements were carried out at room temperature (25°C), the nano-domains dominate the dielectric response of the composites.[27] Therefore, the dielectric constant of the PMN-rich compositions decreases with increasing applied stress, as seen in Fig. 3.

4. Conclusions

In this study, the dielectric constants under the uniaxial compressive pre-stress of the BT-PZT, PMN-PT and PMN-PZT ceramics are observed at stress up to 15 MPa, 22 MPa and 5 MPa, respectively, using a uniaxial compressometer. The dielectric constant of the BT-PZT ceramics increases significantly with increasing applied stress. Larger changes in the dielectric constant with the applied stress are observed in the PZT-rich compositions. For PMN-PT system, the dielectric constant of 0.9PMN-0.1PT decreases significantly with the applied stress, while that of other compositions is rather stable. For PMN-PZT system, the dielectric constant of the PMN-rich compositions decreases, while that of the PZT-rich compositions increases slightly with increasing applied stress. The experimental results are explained in terms of domains, domain walls and de-aging mechanisms. The contributions of different domain-related phenomena to the dielectric responses of these lead-based ferroelectric ceramics under the compressive pre-stress depend greatly on compositions and temperature. Finally, this study undoubtedly shows that the applied compressive pre-stress has significant influences on the dielectric properties of the lead-based ferroelectric ceramics.

Acknowledgments

The author would like to express his sincere gratitude for contributions from colleagues, S. Wongsaenmai, S. Chamunglap, M. Unruan and S. Ananta. This work was supported by the Thailand Research Fund (TRF).

References

1. B. Jaffe and W. R. Cook, *Piezoelectric Ceramics* (R.A.N. Inc., New York, 1971).
2. L. E. Cross, *Mater. Chem. Phys.* **43**, 108 (1996).
3. G. H. Haertling, *J. Am. Ceram. Soc.* **82**(4), 797 (1999).
4. A. J. Moulson and J. M. Herbert, *Electroceramics: Materials, Properties, Applications*, 2nd edn. (John Wiley, New York, 2003).
5. W. Chaisan, S. Ananta and T. Tunkasiri, *Cur. Appl. Phys.* **4**, 182 (2004).
6. L. E. Cross, *Ferroelectrics* **76**, 241 (1987).
7. M. Lejeune and J. P. Boilot, *Mater. Res. Bull.* **20**, 493 (1985).
8. S. W. Choi, T. R. Shrout, S. J. Jang and A. S. Bhalla, *Ferroelectrics* **100**, 29 (1989).
9. S. W. Choi, J. M. Tang and A. S. Bhalla, *Ferroelectrics* **189**, 27 (1996).
10. J. H. Yoo, H. S. Yoon, Y. H. Jeong and C. Y. Park, *Proc. IEEE Ultra. Symp.* **1**, 981 (1998).
11. A. V. Shilnikov, A. V. Sopit, A. I. Burkhanov and A. G. Luchaninov, *J. Eur. Ceram. Soc.* **19**, 1295 (1999).
12. Y. H. Xu, *Ferroelectric Materials and Their Applications* (North Holland, Los Angeles, 1991).
13. D. Viehland and J. Powers, *J. Appl. Phys.* **89**(3), 1820 (2001).
14. J. Zhao and Q. M. Zhang, *Proc. IEEE ISAF* **2**, 971 (1996).
15. J. Zhao, A. E. Glazounov and Q. M. Zhang, *Appl. Phys. Lett.* **74**, 436 (1999).
16. W. Chaisan, R. Yimnirun, S. Ananta and D. P. Cann, *Mater. Lett.* **59**, 3737 (2005).

17. R. Yimnirun, S. Ananta and P. Laoratanakul, *Mater. Sci. Eng. B* **112**, 79 (2004).
18. R. Yimnirun, S. Ananta and P. Laoratanakul, *J. Euro. Ceram. Soc.* **25**, 3225 (2005).
19. S. L. Swartz and T. R. Shrout, *Mater. Res. Bull.* **17**, 1245 (1982).
20. R. Yimnirun, P. Moses, R. J. Meyer and R. E. Newnham, *Rev. Sci. Instrum.* **74**, 3429 (2003).
21. R. Yimnirun, S. Ananta, E. Meechoowas and S. Wonsaenmai, *J. Phys. D: Appl. Phys.* **36**, 1615 (2003).
22. J. M. Calderon-Moreno, *Mater. Sci. Eng. A* **315**, 227 (2004).
23. D. Zhou, M. Kamlah and D. Munz, *J. Euro. Ceram. Soc.* **25**, 425 (2005).
24. G. Yang, W. Ren, S. F. Liu, A. J. Masys and B. K. Mukherjee, *Proc. IEEE Ultra. Symp.* **1**, 1005 (2000).
25. G. Yang, S. F. Liu, W. Ren and B. K. Mukherjee, *Proc. SPIE Symp. Smart Struct. Mats.* **3992**, 103 (2000).
26. O. Steiner, A. K. Tagantsev, E. L. Colla and N. Setter, *J. Euro. Ceram. Soc.* **19**, 1243 (1999).
27. Q. M. Zhang, J. Zhao, K. Uchino and J. Zheng, *J. Mater. Res.* **12**, 226 (1997).

Scaling behavior of dynamic hysteresis in soft lead zirconate titanate bulk ceramics

Rattikorn Yimnirun,[a] Yongyut Laosiritaworn, Supattra Wongsaenmai, and Supon Ananta
Department of Physics, Faculty of Science, Chiang Mai University, Chiang Mai 50200, Thailand

(Received 15 June 2006; accepted 2 September 2006; published online 16 October 2006)

The scaling behavior of the dynamic hysteresis of ferroelectric bulk system was investigated. The scaling relation of hysteresis area $\langle A\rangle$ against frequency f and field amplitude E_0 for the saturated loops of the soft lead zirconate titanate bulk ceramic takes the form of $\langle A\rangle \propto f^{-1/4}E_0$, which differs significantly from that of the theoretical prediction and that of the thin film. This indicates that the scaling relation is dimension dependent and that depolarizing effects in the interior must be taken into account to model bulk materials. Additionally, the scaling relation for the minor loops takes the form of $\langle A\rangle \propto f^{-1/3}E_0^3$, which is identical to that of the thin film as both cases contain similar 180° domain-reversal mechanism. © *2006 American Institute of Physics*. [DOI: 10.1063/1.2363143]

Lead zirconate titanate [$Pb(Zr_{1-x}Ti_x)O_3$ or PZT] ceramics have been employed extensively in sensors and actuators, particularly donor-doped PZT with "soft" piezoelectric behaviors.[1,2] In these applications, the dynamic hysteresis, i.e., hysteresis area $\langle A\rangle$ as a function of the field amplitude E_0 and frequency f, has become an important consideration.[1,3] Many theoretical studies have been focused on scaling law $\langle A\rangle \propto f^{\alpha}E_0^{\beta}$ (where α and β are exponents that depend on the dimensionality and symmetry of the system) of hysteresis curves in polarization systems.[4–7] The three-dimensional models [$(\Phi^2)^2$ and $(\Phi^2)^3$] by Rao *et al.*[4] and other investigators[7,8] proposed two scaling relations applicable to the low-f and high-f limits as follows:

$$\langle A\rangle \propto f^{1/3}E_0^{2/3} \quad \text{as } f\to 0, \tag{1}$$

$$\langle A\rangle \propto f^{-1}E_0^{2} \quad \text{as } f\to \infty. \tag{2}$$

Technologically, it is helpful to understand the scaling behavior so that the ultrahigh-frequency hysteresis can be predicted. Hence, there have been reports on the scaling behavior of the dynamic hysteresis in ferromagnetic and ferroelectric thin films, with some discrepancies between theoretical and experimental results.[6–13] In contrast to the theoretically predicted scaling relation at high-f limit in Eq. (2), the experimental investigation on PZT thin film[14] has resulted in a different relation, i.e.,

$$\langle A\rangle \propto f^{-1/3}E_0^{3} \quad \text{as } f\to \infty. \tag{3}$$

Interestingly, there has been no report on the scaling studies of ferroelectric hysteresis in bulk ceramics. Thus, we present in this letter the results on the scaling behavior of the dynamic hysteresis of soft PZT bulk ceramic.

The dynamic hysteresis (P-E) loops of commercial soft PZT ceramic disks (PKI-552, Piezo Kinetics Inc., USA) with diameter of 10 mm and thickness of 1 mm were characterized at room temperature (25 °C) by using a modified Sawyer-Tower circuit with f covering from 2 to 100 Hz and E_0 from 0 to 18 kV/cm. The electric field was applied to a sample by a high voltage ac amplifier (Trek 610D) with the input sinusoidal signal from a function generator (HP 3310A). The P-E loops were recorded by a digital oscilloscope (HP 54645A, 100 MHz). Each loop was obtained after 20 sampling cycles to average out the noise deformation. The details of the system were described elsewhere.[14] The hysteresis loop obtained was very consistent with that obtained by a standardized ferroelectric testing unit, RT66A (Radiant Technologies Inc., NM), which ensures the reliability of the measurements.

The hysteresis loops at different f but fixed E_0 (18 kV/cm) and at different E_0 but fixed f (100 Hz) are shown in Fig. 1. The loop area $\langle A\rangle$, remanent polarization (P_r), and coercive field (E_c) decrease with an increase of frequency, as shown in Fig. 1(a). The dependence of the hysteresis loop on E_0 is depicted in Fig. 1(b). For small fields (6 and 12 kV/cm), the loop does not saturate. With further increase in E_0, $\langle A\rangle$, P_r, and E_c increase until well saturated loop is achieved. Similar observations have been reported in thin films.[7,10,13]

To investigate the scaling behavior, we followed the theoretical predictions on the loop area[4,5,8] by plotting $\langle A\rangle$ against $f^{-1}E_0^2$. The data are shown in Fig. 2(a) and the dotted line represents a fitting in terms of $\langle A\rangle \propto f^{-1}E_0^2$. Clearly, the theoretically proposed scaling relation in Eq. (2) cannot be directly applied to the data obtained in this study. Moreover, earlier experimental work[13] on the PZT thin film showed a different relation, expressed in Eq. (3). To check the validity of the relation on the bulk ceramic, we plot $\langle A\rangle$ against $f^{-1/3}E_0^3$, as shown in Fig. 2(b) with the dotted line representing a fitting in terms of $\langle A\rangle \propto f^{-1/3}E_0^3$. Large deviation observed also implies that the experimentally obtained scaling relation for the thin film is not applicable to the bulk ceramic. However, a closer check shows that Eqs. (2) and (3) appear to yield reasonable fits to the low E-field data, as shown in Fig. 2. The discussion on this observation will be formulated later.

To obtain the suitable scaling relation for the bulk ceramic, one can fit the data with $\langle A\rangle \propto f^{m}E_0^{n}$, where m and n are exponents to be determined directly from the experimental data. By plotting $\langle A\rangle$ against f at fixed E_0, one obtains the exponent m. On the other hand, the exponent n can be obtained from plotting $\langle A\rangle$ against E_0 at fixed f. As plotted in

[a]Author to whom correspondence should addressed; electronic mail: rattikornyimnirun@yahoo.com

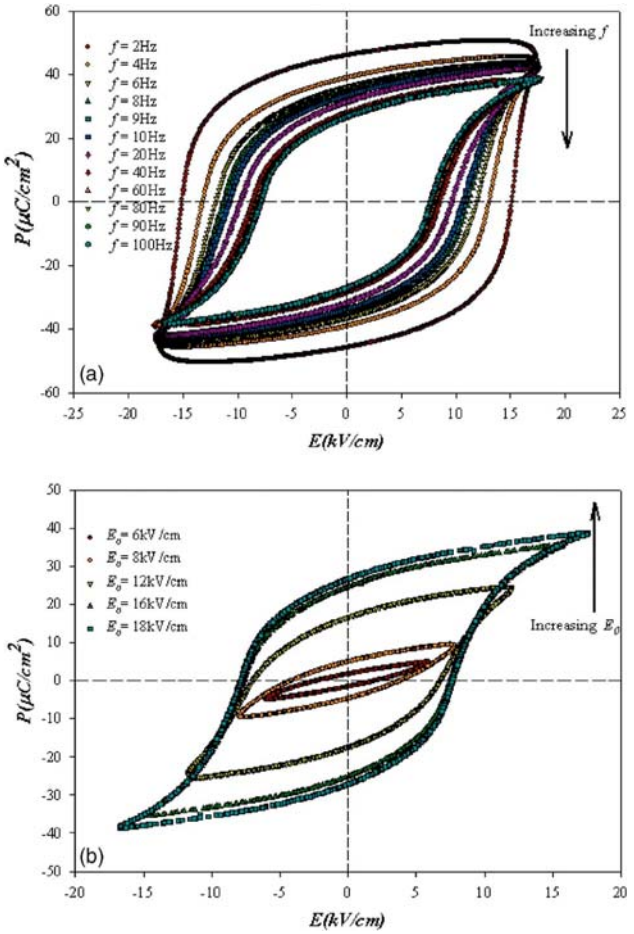

FIG. 1. (Color online) Hysteresis loops for soft PZT ceramic (a) at various f and $E_0=18$ kV/cm and (b) at various E_0 and $f=100$ Hz.

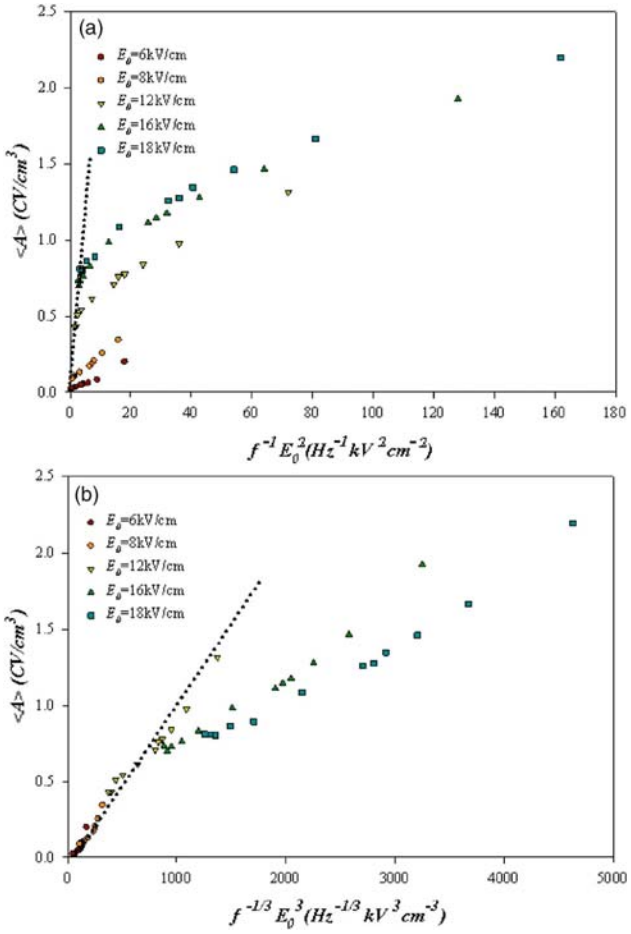

FIG. 2. (Color online) Scaling of hysteresis area $\langle A\rangle$ against (a) $f^{-1}E_0^2$ and (b) $f^{-1/3}E_0^3$ for soft PZT ceramic.

Fig. 3(a), it is revealed that the high E-field data can be much better fitted (with $R^2=0.97$), within the measured uncertainty, by

$$\langle A\rangle \propto f^{-1/4}E_0. \tag{4}$$

Though the minor loop data were excluded from the fitting reported in Eq. (4), it is possible that a different scaling behavior could be established for the low E-field region, as also reported in previous investigations.[11,12] More discussions on this will follow.

The scaling relation obtained in Eq. (4) indicates that $\langle A\rangle$ decays more slowly with f and grows more slowly with E_0 than the theoretical prediction, Eq. (2). $\langle A\rangle$ also decays slightly slower with f, but grows much more slowly with E than the PZT thin film, Eq. (3). An explanation for the difference may come from the polarization-interaction terms as considered in the $(\Phi^2)^2$ and $(\Phi^2)^3$ models, in which the polarization flip just has one contribution, i.e., polarization reversal.[4,5] This requires overcoming high energy barrier. The Potts model used by Liu *et al.*[13] also has the polarization orientation in various domains in directions not antiparallel to the direction of E, hence requires lower energy barrier for polarization flip to occur, which results in a higher exponent of 3 in the E_0 term, as compared to the exponent of 2 in the theoretical models. However, in ceramics, there are influences of many depolarizing effects, arisen from domain walls, grain boundaries, space charges, immobile defects, etc., which may retard the external field. Consequently, the energy barrier is very much higher, which leads to slower polarization-flip kinetics. Therefore, a low exponent for the E_0 term is expected from the ceramics.

In addition, the f term shows an exponent of $-1/4$, smaller in absolute value than that of PZT thin film (exponent is $-1/3$).[13] To explain the difference, one may need to consider not only the contribution from the domain switching and ionic type in thin films[13] but also additional contributions to hysteresis properties from space charges on grain boundaries, induced electric field from interface layers, immobile defects,[15] etc. Therefore, in a bulk-ceramic type these depolarizing effects, acting as a buffer to polarization-reversal mechanism, will be stronger than those in thin film structure. As a result, the hysteresis area must show a relatively weaker dependence on f than that observed in thin films.

Returning to the observation in Fig. 3(a), there are actually two slopes—one at low E fields (high frequencies) and a different slope at high E fields (low frequencies). Additionally, Eqs. (2) and (3) appear to yield reasonable fits to the low E-field data in Fig. 2. In contrast, Eq. (4) appears to fit the high E-field data to a reasonable extent. It is therefore important to explain the fundamental nature of the different slopes. Probable reasons lie in the complexities of the domain structure of PZT, which also depends on the dimensionality.[16,17] A number of recent studies have explored this behavior and reported that it is likely that different do-

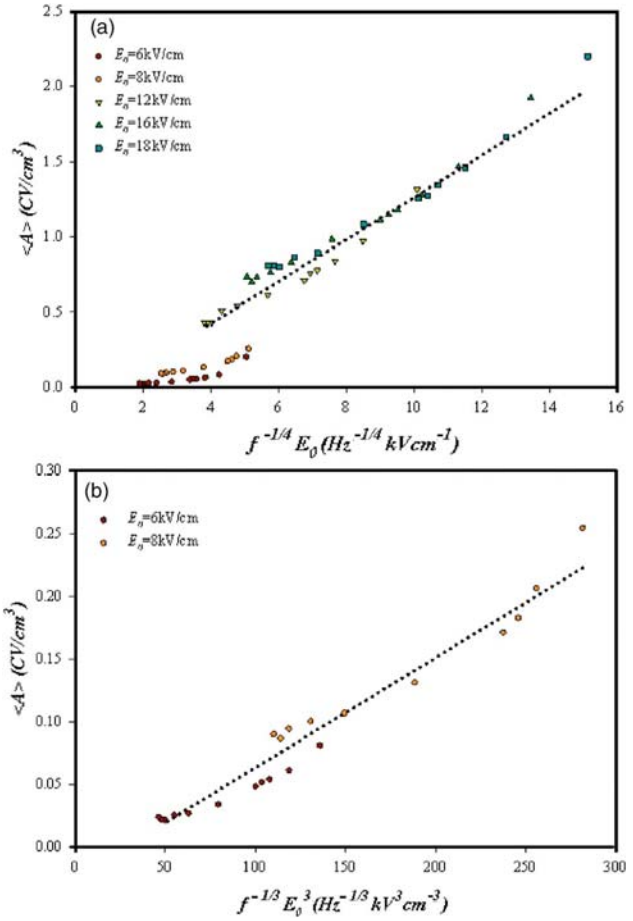

FIG. 3. (Color online) Scaling of hysteresis for soft PZT ceramic: (a) area $\langle A\rangle$ against $f^{-1/4}E_0$ for the saturated loops and (b) area $\langle A\rangle$ against $f^{-1/3}E_0^3$ for the minor loops.

main walls are being activated at different fields.[6,7,17–20] Generally, PZT ceramics have 180° and non-180° domain structures.[19,20] As the non-180° domain switching is normally accompanied with mechanical strain, it occurs at higher E field than the 180° domain reversal does.[18–20] Therefore, under low E fields, one would expect the 180° domain reversal to occur first. It is also well known that the non-180° domain wall motion is typically very heavily clamped in thin films.[17] Therefore, the main switching contribution in thin films would be from the 180° domain reversal. This explains why the scaling behavior of PZT bulk ceramics at low E fields is similar to that of thin films. This is further supported by the scaling relation of PZT bulk ceramics obtained for low E fields in the form of $\langle A\rangle \propto f^{-1/3}E_0^3$, as shown in Fig. 3(b). Considering the various domain types observed in PZT, it should be worthwhile to examine the scaling relation for a simpler ferroelectric with only one type of domain wall (e.g., $Bi_4Ti_3O_{12}$). Interestingly, a previous investigation[21] on Nd-doped $Bi_4Ti_3O_{12}$ yielded a scaling in the form of $\langle A\rangle \propto f^{-2/3}E_0^2$, which is closer to the theoretical prediction [Eq. (2)] and that for the $SrBi_2Ta_9O_4$ thick film.[12]

In summary, the scaling relation for the saturated hysteresis loops of the soft PZT ceramic takes the form of $\langle A\rangle \propto f^{-1/4}E_0$, which differs significantly from that of the theoretical prediction and that of the PZT thin film. Additionally, the scaling relation for the minor loops is identical to that of thin films, i.e., $\langle A\rangle \propto f^{-1/3}E_0^3$.

This work was supported by the Thailand Research Fund, Commission on Higher Education, Graduate School and Faculty of Science, Chiang Mai University.

[1]K. Uchino, *Ferroelectric Devices* (Dekker, New York, 2000), p. 145.
[2]B. Jaffe, W. R. Cook, and H. Jaffe, *Piezoelectric Ceramics* (Academic, New York, 1971), p. 271.
[3]J. F. Scott, Ferroelectr. Rev. **1**, 1 (1998).
[4]M. Rao, H. R. Krishnamurthy, and R. Pandit, Phys. Rev. B **42**, 856 (1990).
[5]M. Acharyya and B. K. Chakrabarti, Phys. Rev. B **52**, 6560 (1995).
[6]J.-M. Liu, H. L. W. Chan, C. L. Choy, and C. K. Ong, Phys. Rev. B **65**, 014416 (2001).
[7]J.-M. Liu, H. L. W. Chan, C. L. Choy, Y. Y. Zhu, S. N. Zhu, Z. G. Liu, and N. B. Ming, Appl. Phys. Lett. **79**, 236 (2001).
[8]M. Rao and R. Pandit, Phys. Rev. B **43**, 3373 (1991).
[9]Q. Jiang, H. N. Yang, and G. C. Wang, Phys. Rev. B **52**, 14911 (1995).
[10]B. Pan, H. Yu, D. Wu, X. H. Zhou, and J.-M. Liu, Appl. Phys. Lett. **83**, 1406 (2003).
[11]Y.-H. Kim and J.-J. Kim, Phys. Rev. B **55**, R11933 (1997).
[12]J.-H. Park, C.-S. Kim, B.-C. Choi, B. K. Moon, J. H. Jeong, and I. W. Kim, Appl. Phys. Lett. **83**, 536 (2003).
[13]J.-M. Liu, H. L. W. Chan, and C. L. Choy, Mater. Lett. **52**, 213 (2002).
[14]R. Yimnirun, Y. Laosiritaworn, and S. Wongsaenmai, J. Phys. D **39**, 759 (2006).
[15]D. Bolten, U. Böttger, and R. Waser, Appl. Phys. Lett. **84**, 2379 (2004).
[16]A. Gruverman, O. Auciello, and H. Tokumoto, Annu. Rev. Mater. Sci. **28**, 101 (1998).
[17]S. Trolier-McKinstry, N. B. Gharb, and D. Damjanovic, Appl. Phys. Lett. **88**, 202901 (2006).
[18]N. Uchida and T. Ikeda, Jpn. J. Appl. Phys. **4**, 867 (1965).
[19]T. Tsurumi, T. Sasaki, H. Kakemoto, T. Harigai, and S. Wada, Jpn. J. Appl. Phys., Part 1 **43**, 7618 (2004).
[20]K. Lee and S. Baik, Annu. Rev. Mater. Res. **36**, 81 (2006).
[21]J.-M. Liu, B. Pan, H. Yu, and S. T. Zhang, J. Phys.: Condens. Matter **16**, 1189 (2004).

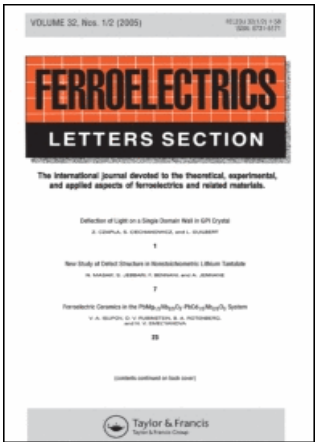

Ferroelectrics Letters Section
Publication details, including instructions for authors and subscription information:
http://www.informaworld.com/smpp/title~content=t713871498

Polarization Behavior in the Two Stage Sintered Lead Titanate Ceramics

R. Wongmaneerung [ab]; R. Yimnirun [a]; S. Ananta [a]; R. Guo [b]; A. S. Bhalla [b]
[a] Department of Physics, Faculty of Science, Chiang Mai University. Chiang Mai. Thailand
[b] Materials Research Laboratory, Pennsylvania State University. University Park, PA, 16802. USA

To cite this Article: R. Wongmaneerung, R. Yimnirun, S. Ananta, R. Guo and A. S. Bhalla , 'Polarization Behavior in the Two Stage Sintered Lead Titanate Ceramics', Ferroelectrics Letters Section, 33:5, 137 - 146
To link to this article: DOI: 10.1080/07315170601014984
URL: http://dx.doi.org/10.1080/07315170601014984

Ferroelectric Letters, 33:137–146, 2006

ISSN: 0731-5171 print / 1543-5288 online
DOI: 10.1080/07315170601014984

Taylor & Francis
Taylor & Francis Group

Polarization Behavior in the Two Stage Sintered Lead Titanate Ceramics

R. WONGMANEERUNG,[1,2] R. YIMNIRUN,[1] S. ANANTA,[1]
R. GUO,[2] and A. S. BHALLA[2]

[1]*Chiang Mai University, Department of Physics, Faculty of Science, Chiang Mai, Thailand*
[2]*Pennsylvania State University, Materials Research Laboratory, University Park, PA 16802, USA*

Communicated by Dr. George W. Taylor

(Received July 24, 2006)

Polarization behavior in lead titanate, prepared by the two stage sintering approach, is determined by using the dilatometer thermal expansion data. We report the temperature-dependent measurements of the strain, the magnitude of polarization, $\sqrt{\overline{P}_S^2}$, deduced from the sets of data gathered from the thermal expansion values. The calculated values of the electric polarization, P_S, on the two stage sintered lead titanate ceramics show the simple approach to determine the temperature dependence of the polarization below and around the transition temperature. Various aspects of our understanding of the polarization behavior and other effects in the ferroelectric are discussed.

Keywords: polarization behavior; thermal expansion; lead titanate

INTRODUCTION

The high Curie temperature of lead titanate, $PbTiO_3$, ceramics has long qualified these materials for potential high-temperature and high frequency applications [1–3]. For $PbTiO_3$, above the ferroelectric transition temperature, T_C, the structure is cubic and below T_C it becomes tetragonal with a spontaneous polarization P_S. In general, the value of P_S is difficult to measure due to its high coercive field and $T_C \approx 490^\circ C$ [1]. However, the change in polarization with temperature can be observed through thermal expansion (or strain) measurements and from the data, spontaneous polarization and

*Corresponding author. E-mail: asb2@psu.edu

its temperature dependence can be computed. Some authors [4, 5] suggest the value of P_S at room temperature to be greater than 50 μC/cm^2. Shirane [6] and Jona [7] give the value of $P_S = 80$ μC/cm^2.

It is always a challenge to measure the temperature-dependence of the polarization of the high T_C ferroelectric over the entire temperature range. In general with the increase in temperature and due to the increase in losses in the $PbTiO_3$ samples it hinders the real spontaneous polarization and its (P_S) temperature dependence measurements at higher temperature by using the hysteresis and pyroelectric techniques. Therefore, some alternate approaches have to be made in order to extract some useful data on $PbTiO_3$ for the polarization versus temperature behavior. From the phenomenological approach we know that the P_S values can be extracted by using the relation [8];

$$x_{ij} = \frac{\Delta l}{l} = Q_{ijkk} P_k^2 \tag{1}$$

where x_{ij} is the strain, $\Delta l/l$ is thermal expansion, Q_{ijkk} is the electrostrictive coefficient. Q coefficients are determined in paraelectric phase and considered constant. And P_k^2 is the polarization.

Also, by knowing the $\Delta l/l$ and its temperature dependence, P_k versus temperature as well as the transition temperature of $PbTiO_3$ and the nature of the transition can be studied.

In this paper, we report the P_S versus temperature behavior of $PbTiO_3$ samples prepared and sintered under various conditions. Thermal expansion versus temperature behavior has been measured and the values of polarization at various temperatures have been computed. Measurements have also been extended on the unpoled, poled and depoled samples and compared. As clear from the equation (1) that $\Delta l/l$ is directly related to the square of polarization and thus the measurements do not specifically require the poled samples.

EXPERIMENTAL PROCEDURE

Commercially available powders of PbO and TiO_2 (anatase form), (Fluka, >99% purity) were used as starting materials. $PbTiO_3$ powders were synthesized by a simple mixed oxide method. Ceramic fabrication was achieved by adding 3 wt% polyvinyl alcohol binder, prior to pressing as pellets in a pseudo-uniaxial die press at 100 MPa. Each pellet was placed in an alumina

crucible together with an atmosphere powder of identical chemical composition. Sintering was carried out with a dwell time of 2 h at each step, with constant heating/cooling rates of 1°C/min [9]. Three sets of the first sintering temperature were assigned for the two stage sintering [10] case: 700, 800 and 900°C. The second sintering temperature was set at 1200°C.

For thermal expansion measurement, the $PbTiO_3$ samples were cut in bar shapes (5 mm long and 1 mm thick). The sample was placed inside a fused silica holder and the thermal expansion was measured as a function of temperature using a linear voltage-differential transformer (LVDT) dilatometer. The samples were heated at a rate of 2°C/min from room temperature to 600°C. The LVDT has an advantage over the other transformer; it gives a linear output for every unit displacement.

RESULTS AND DISCUSSION

The thermal expansion behaviors of $PbTiO_3$ ceramics synthesized under various sintering condition and with unpoled, poled and depoled states were measured by a high-sensitivity dilatometer, Table I summarizes the various important features of these measurements. The results are shown in Figs. 1a, 1b and 1c, respectively. It should be noted that the thermal expansion measurements were made during the first heating from room temperature after poling. The results show the thermal expansion of $PbTiO_3$ ceramics sintered at 700/1200°C, 800/1200°C and 900/1200°C, respectively in Figs. 1a, b and c. The thermal expansion behaviors of these samples are linear at temperatures above 500°C, i.e., above Curie temperature.

The change of strain at the Curie point may be easily seen in the thermal contraction curves. The phase transition temperatures are in good agreement with the published values [11, 12]. The curves on the depoled samples are parallel to the curve for the unpoled sample, essentially restoring the sample

TABLE I Summary of the various important features of the thermal expansion measurements

	T_C (°C)			Calculates P_S at room temperature ($\mu C/cm^2$)		
Sample	Unpoled	Poled ll	Poled ⊥	Unpoled	Poled ll	Poled ⊥
1 $PbTiO_3$ 700/1200°C	489	482	489	74.99	75.76	69.47
2 $PbTiO_3$ 800/1200°C	481	478	482	75.49	72.28	72.06
3 $PbTiO_3$ 900/1200°C	478	477	476	76.85	74.62	75.81

dimension to the prepoled value. Effect of poling on thermal expansion properties was also determined. It can be noted that the strain values for both perpendicular and parallel (w.r.t. length direction) poled sampled can be reduced or changed by the surface charge. Moreover, it is indicated that the transition temperature is comparatively decreased from the Curie point of the unpoled ceramics.

The high temperature data in the cubic phase, above T_C, can be approximated by a straight line. The deviation from this linear high temperature behavior occurs at approximately the same temperature ($\sim$500°C). On analyzing the deviation of the strain from the high temperature linear behavior and by using Eq. (1) the P_S values can be obtained at various temperatures. Using the values of $Q_{11} = 8.9 \times 10^{-2}$ m^4/C^2 and $Q_{12} = -2.6 \times 10^{-2}$ m^4/C^2 [13], the P_S can be calculated. The results for various samples are plotted in

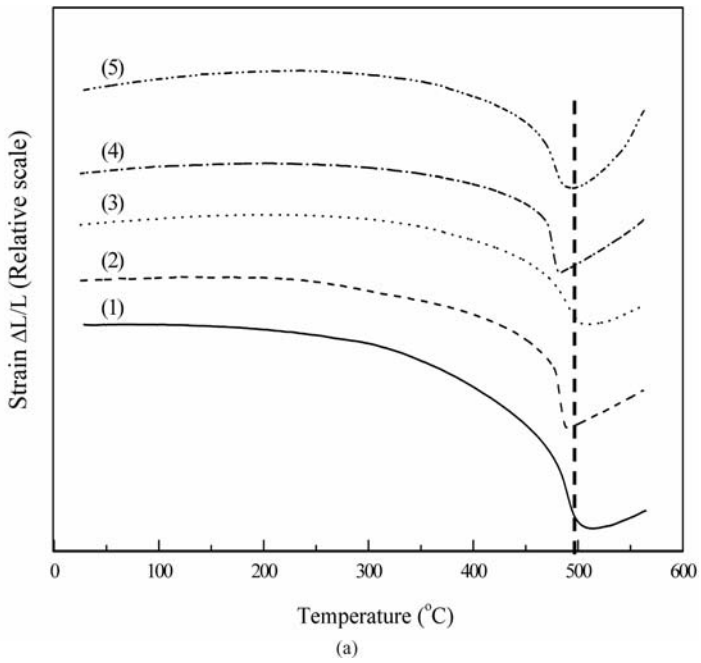

Figure 1. Strain as a function of temperature for $PbTiO_3$ ceramics and of different poling states: (1) unpoled, (2) poled parallel to the length direction, (3) poled perpendicular to the length direction, (4) depoled parallel to the length direction and (5) depoled perpendicular to the length direction (all measurements are in heating cycles and along the length direction); Figures a, b, c are for (a) sintered at 700/1200°C, (b) sintered at 800/1200°C and (c) sintered at 900/1200°C. *(Continued)*

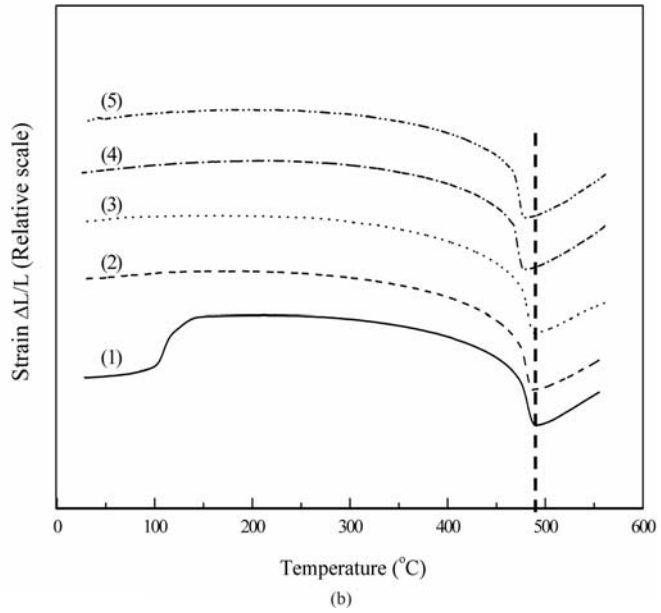

(b)

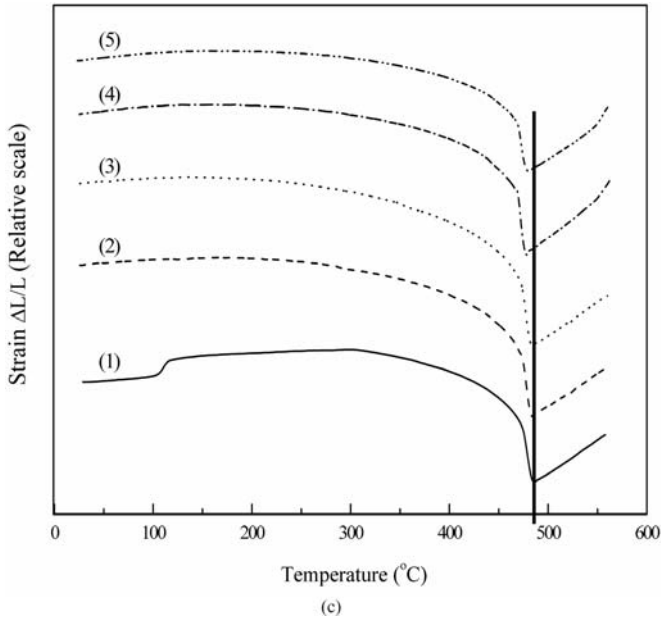

(c)

Figure 1. (Continued)

Figs. 2a, 2b and 2c, respectively. When calculating the spontaneous strains of the tetragonal at a particular temperature, the cubic cell constant should be extrapolated to that temperature accounting for the thermal expansion. A linear extrapolation from above the transition can be made over a narrow range with fairly good accuracy.

In Figures 2a, 2b and 2c are shown the $P_s = \sqrt{\bar{P}_S^2}$ values calculated from the thermal expansion data. The agreement in the P_S values is excellent. The values are also in good agreement not only in magnitude but also in the T_C values with the earlier reported results [6, 7]. Figure 2a, shows the P_S value versus temperature of $PbTiO_3$ ceramic sintered at 700/1200°C. The P_S value in the case of unpoled sample is slightly higher than those of both parallel and perpendicular poled samples in temperature range below Curie point, and is caused by the P_S of the poled ceramics. Also the P_S is smaller than the value in thermally depoled sample. Similar trends have

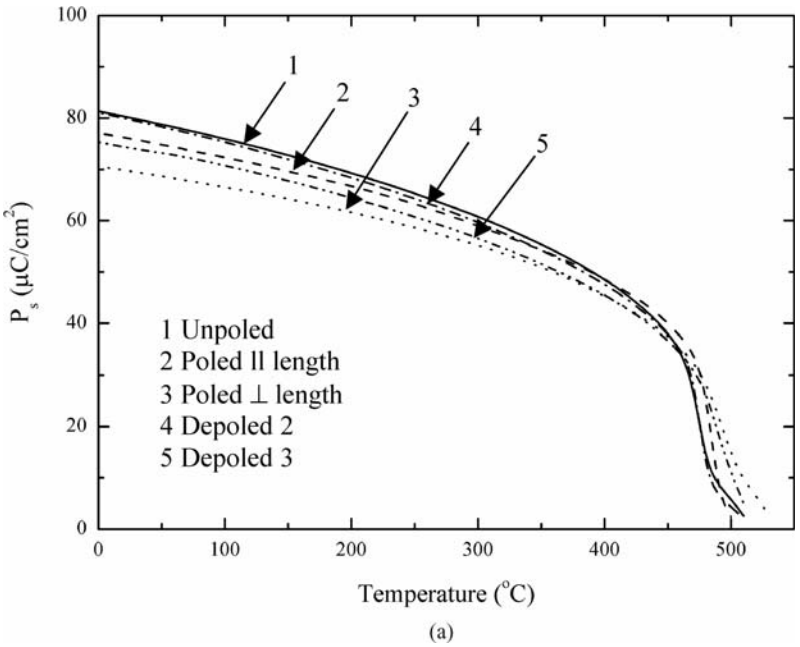

Figure 2. P_S as a function of temperature for $PbTiO_3$ ceramics with and without poling: (1) unpoled, (2) poled parallel to the length direction, (3) poled perpendicular to the length direction, (4) depoled parallel to the length direction and (5) depoled perpendicular to the length direction; figures a, b, c are for (a) sintered at 700/1200°C, (b) sintered at 800/1200°C and (c) sintered at 900/1200°C. *(Continued)*

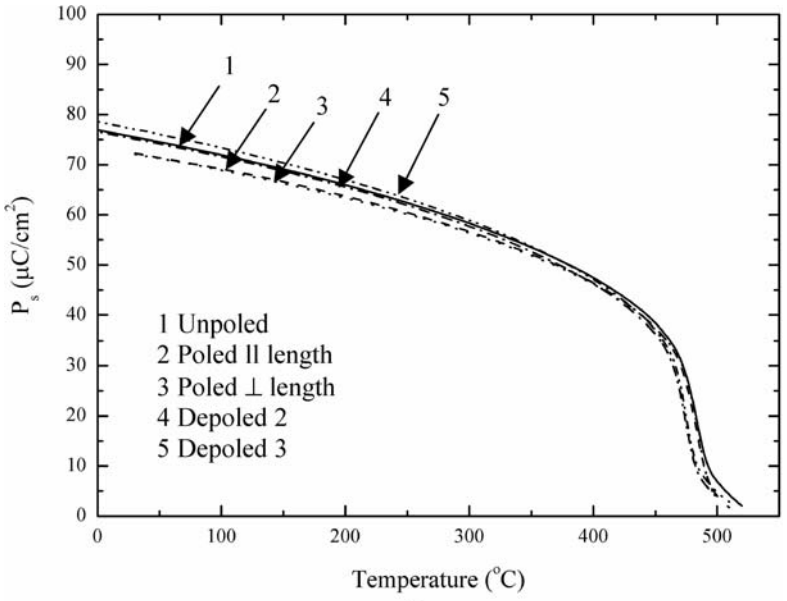

(b)

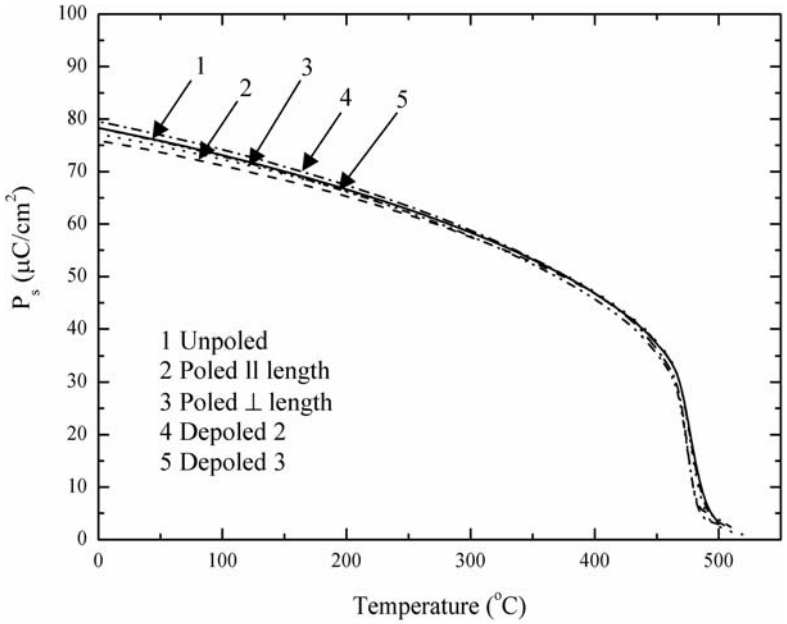

(c)

Figure 2. (Continued)

been noticed in the samples sintered under different processing conditions. There are a few factors which could be influencing the measurements. First, there are some sources of contributions to the strain in ferroelectrics, i.e., in addition to the structural component which is present at all temperatures, a component associated with the appearance of spontaneous polarization in the case of ferroelectric state is also present. The contribution of the spontaneous polarization to strain is due to electrostrictive coupling. Second, after poling it is also possible to have some residual surface charge on the surfaces which can affect the net strain. For perpendicular poling conditions, the net thermal strain might be more along the length due to the positive expansion of a-axis. Therefore, the strain along the length direction can be affected differently in the parallel and perpendicular poled samples. At temperature near T_C, it is seen that the P_S values of both poled samples are sharper compare to those of unpoled and depoled samples. For the other two samples sintered under different conditions, the polarization behaviors are slightly different, however, the magnitude of P_S and trend of polarization behavior are similar to that of 700/1200°C $PbTiO_3$ ceramic. The sharpness of the transition increases and the hyteresis space gradually decreases for the samples sintered at higher temperature in first step of the two stage sintering process.

CONCLUSIONS

We investigated the polarization behavior of $PbTiO_3$ ceramics in unpoled, poled and depoled states by using the thermal expansion data. The room temperature $P_S = 75\ \mu C/cm^2$ is in good agreement with the reported values and also suggesting that thermal strain data can be used for estimating the reliable polarization and its temperature dependence in the case of high T_C ferroelectrics or where the high conductivity of the samples interferes with the electrical measurements. Some important conclusions are made as follow:

(i) The temperature dependence of thermal strain of unpoled and poled ceramics showed nonlinearity and large anomalies resulting from polarization.
(ii) The unpoled and depoled samples synthesized under the different two stage sintering conditions exhibited similar behavior in strain versus temperature and the poled samples tend to increase the sharpness of the transition. The polarization behavior shows a sharp first-order phase transition.

(iii) Hysteresis of T_C in heating and cooling cycles is larger in the samples sintered at lower temperature (data not shown here).
(iv) On poling hysteresis of T_C (cooling and heating cycles) in general decreases.
(v) Transitions with parallel poled samples are sharper.
(vi) The polarization versus temperature and its decay, above T_C, is less dispersive for the high temperature sintered or the high density ceramics.
(vii) In the case of higher density samples, all the T_C (unpoled, poled and depoled) are approximately the same.

ACKNOWLEDGMENT

We thank the Thailand Research Fund (TRF), the Graduate School of Chiang Mai University and NSF Relaxor program, Materials Research Laboratory and MRI of Penn State University for all the support during this work.

REFERENCES

[1] B. Jaffe, W. R. Cook, and H. Jaffe, *Piezoelectric Ceramics* (New York, Academic Press, 1971).
[2] G. H. Haertling, Ferroelectric Ceramics: History and Ttechnology, *J. Am. Ceram. Soc*., **82**(4), 797–818 (1999).
[3] T. Takahashi, Lead Titanate Ceramics with Large Piezoelectric Anisotropy and Their Applications, *Am. Ceram. Soc. Bull.* **69**, 691–695 (1990).
[4] G. Burns and B.A. Scott, Lattice Modes in Ferroelectric Perovskite: $PbTiO_3$, *Phys. Rev. B* **7**, 3087–3101 (1973).
[5] F. G. Fesenko, V. G. Gavrilyachenko, and E. V. Zarochencev, *Izv, Akad. Nauk SSSR*, **34**, 2541 (1970).
[6] V. G. Gavrilyachenko, R. I. Spinko, M. A. Martynenko, and E. G. Fesenko, *Fiz. Tverd. Tela* **12**, 1532 (1970); *Sov. Phys. Solid State (English Transl.)* **12**, 1203 (1970).
[7] F. Jona and G. Shirane, *Ferroelectric Crystal* (Oxford, Pergamon Press, 1962).
[8] A. S. Bhalla, R. Guo, and L. E. Cross, Measurements of Strain and the Optical Indices in the Ferroelectric $Ba_{0.4}Sr_{0.6}Nb_2O_6$: Polarization Effects, *Phys. Rev. B.* **36**, 2030–2035 (1987).
[9] A. Udomporn, K. Pengpat, and S. Ananta, Highly Dense Lead Titanate Ceramics from Refined Processing, *J. Eur. Ceram. Soc.* **24**, 185–188 (2004).
[10] S. Ananta and N.W. Thomas, Fabrication of PMN and PFN Ceramics by a Two-Stage Sintering Technique, *J. Eur. Ceram. Soc.* **19**, 2917–2930 (1999).

[11] G. Shirane and S. Hoshino, On the Phase Transition in Lead Titanate, *J. Phys. Soc. Jpn*. **6**, 265–270 (1951).

[12] G. Shirane, R. Pepinsky, and B. C. Frazer, X-Ray and Neutron Diffraction Study of Ferroelectric $PbTiO_3$, *Acta Crystallogr*., **9**, 131–140 (1956).

[13] M. J. Huan, E. Furman, S. J. Jang, H. A. McKinstry and L. E. Cross, Thermodynamic Theory of $PbTiO_3$, *J. Appl. Phys.* **62**, 3331–3338 (1987).

Stress-dependent scaling behavior of dynamic hysteresis in bulk soft ferroelectric ceramic

Rattikorn Yimnirun,[a] Supattra Wongsaenmai, Supon Ananta, and Yongyut Laosiritaworn
Department of Physics, Faculty of Science, Chiang Mai University, Chiang Mai 50200, Thailand

(Received 12 September 2006; accepted 20 October 2006; published online 11 December 2006)

The effects of frequency f, field amplitude E_0, and mechanical stress σ on the hysteresis area $\langle A \rangle$ and their scaling relations were investigated on soft PZT bulk ceramics. The hysteresis area was found to depend on the frequency and field amplitude with a same set of exponents to the power-law scaling for both with and without stresses, indicating the universality. The inclusion of stresses into the power law was also obtained in the form of $\langle A - A_{\sigma=0} \rangle \propto f^{-0.25} E_0 \sigma^{0.44}$, which indicates the difference of the energy dissipation between the under stress and stress-free conditions and reveals how the hysteresis area decays with increasing stresses. © *2006 American Institute of Physics*. [DOI: 10.1063/1.2403182]

The dynamic hysteresis characteristics have become an important consideration since hysteresis area $\langle A \rangle$ as a function of the field amplitude E_0 and frequency f presents lots of information critical for many ferroelectric applications.[1,2] Theoretical studies have been carried out to understand the dynamic response of hysteresis curves in spin and polarization systems.[3–5] In particular, attention is focused on the scaling law $\langle A \rangle \propto f^m E_0^n$ (where m and n are exponents that depend on the dimensionality and symmetry of the system). Based on three-dimensional models, it has been suggested that $m=1/3$ and $n=2/3$ as $f \rightarrow 0$, whereas $m=-1$ and $n=2$ as $f \rightarrow \infty$.[3,5,6] Experimental investigations on a few thin-film systems have also been reported with variation in the scaling relations obtained.[5–11] On the contrary, there is only a single report on the scaling behavior studies of ferroelectric hysteresis loops of bulk ferroelectric ceramics.[12] More importantly, in many applications the ceramic specimens are often subjected to mechanical loading, either from the design of the device itself or from operating conditions which induce stresses.[1,13] Therefore, a prior knowledge of how the material properties change under different load conditions in materials is inevitably crucial for proper design of a device and for suitable selection of materials for a specific application. In many previous investigations the electrical properties of ceramics were found to depend strongly on stresses (σ).[14–18] Since f, E_0, and σ have been reported to impose significant influence on the dynamic hysteresis responses of ferroelectric ceramics, it is therefore the aim of this study to establish the scaling behavior of the dynamic hysteresis responses of bulk ceramics under the influence of the external stress.

Due to its commercial availability and many practical applications, a donor-doped or soft lead zirconate titanate (PZT) ceramic was used in this study. The disk-shaped samples of a commercially available soft PZT ceramic (PKI-552, Piezo Kinetics Inc., USA) with a diameter of 10 mm and a thickness of 1 mm were used in this study. Its basic properties are dielectric constant (1 kHz) $\varepsilon_r=3400$, Curie temperature $T_C=200\ ^\circ$C, piezoelectric strain constants $d_{33}=550$ pm/V and $d_{31}=-270$ pm/V, planar coupling factor $k_p=0.63$, mechanical quality factor $Q_m=75$, and coercive field (50 Hz) $E_c=7.5$ kV/cm. The dynamic hysteresis (P-E) loops were characterized at room temperature (25 °C) by using a modified Sawyer-Tower circuit with f covering from 2 to 100 Hz and E_0 from 0 to 18 kV/cm. The electric field was applied to a sample by a high voltage ac amplifier (Trek 610D) with the input sinusoidal signal from a function generator (HP 3310A). The P-E loops were recorded by a digital oscilloscope (HP 54645A, 100 MHz). The detailed descriptions of this system were explained elsewhere.[17] Effects of the external stress on the dynamic hysteresis were investigated with the compressometer, which was developed for simultaneous applications of the mechanical stress and the electric field.[18] The compressive stress, applying parallel to the electric field direction, was supplied by the servohydraulic load frame and monitored with the pressure gauge. The P-E loops were recorded as a function of mechanical stress applied discretely between 0 and 24 MPa for each applied field and frequency. At each constant stress, the loop was obtained after 20 sampling cycles to average out the noise deformation.

The hysteresis profiles for various frequencies f, field amplitude E_0, and stress σ are obtained. For a particular applied stress, as expected, the dependence of the loop pattern and area $\langle A \rangle$ on f and E is remarkable. At fixed E_0, the loop area $\langle A \rangle$, remnant polarization (P_r), and coercive field (E_c) decrease with an increase of frequency. For the dependence of the hysteresis loop on E_0, the loop does not saturate at small fields (6 and 8 kV/cm). With further increase in E_0, $\langle A \rangle$, P_r, and E_c increase until a well saturated loop is achieved. Similar stress-free observations have been reported in thin films and bulk ceramics.[5,9,12]

Figure 1 displays the hysteresis loops under different compressive stresses during loading at fixed f of 100 Hz and fixed E_0 of 18 kV/cm. The P-E loop area $\langle A \rangle$ is found to decrease steadily with increasing the stress. To investigate the scaling behavior under the effect of applied stresses, instead of including only the field amplitude E_0 and the frequency term f, the scaling relation should also include the stress (σ) term, i.e.,

$$\langle A \rangle \propto f^m E_0^n \sigma^p. \tag{1}$$

However, due to increasing number of exponents, to simplify the problem, the validity of the scaling law $\langle A \rangle(\sigma)$

[a]Author to whom correspondence should be addressed; electronic mail: rattikornyimnirun@yahoo.com

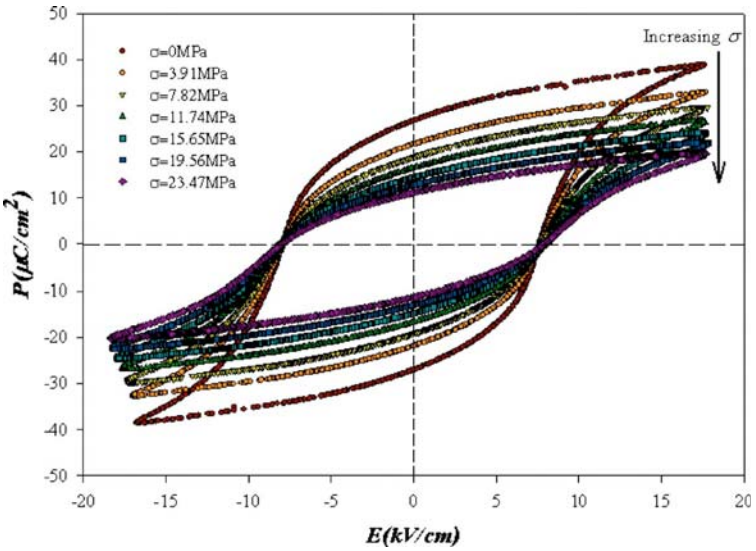

FIG. 1. (Color online) Hysteresis loops for soft PZT ceramic at various σ ($f=100$ Hz and $E_0=18$ kV/cm).

$\propto f^{-0.25}E_0$ is assumed, inspired by a stress-free investigation on bulk PZT,[12] for all applied stresses. Consequently, the area $\langle A\rangle$ for each stress is plotted against $f^{-0.25}E_0$, as shown in Fig. 2, and it can be seen from the least-squares linear fits that reasonably good linear relations can be found. As a result, the condition of universality having $m=-0.25$ and $n=1$ in soft PZT bulk ceramic systems is confirmed, whereas the proportional constant in Eq. (1) may still be a function of σ. Therefore, Eq. (1) is generalized by writing

$$\langle A\rangle = G(\sigma)f^{-0.25}E_0 + F(\sigma), \tag{2}$$

where both $G(\sigma)$ and $F(\sigma)$ are assumed to be a function of σ representing slope function and y-intercept function for a "linear relation" in Eq. (2), and their values are presented via linear-fit functions in Fig. 2. Next, to obtain the scaling form as indicated in Eq. (1), the slope function $G(\sigma)$ is assumed to take a form of power-law function, i.e., $G(\sigma)=a+b\sigma^c$, and a nonlinear fit for $G(\sigma)$ gives $a=0.136\pm0.021$, $b=-0.019\pm0.015$, and $c=0.439\pm0.173$ with $R^2\approx0.994$. However, for the y-intercept function $F(\sigma)$, the scattering data in $F(\sigma)$ do not follow a trivial power-law scaling form. Instead, the reasonably well-fitted function that suits $F(\sigma)$ in the current study is found to take a quadratic function. So $F(\sigma)=a_0+a_1\sigma+a_2\sigma^2$ is written and a least-squares fit is performed to give $a_0=-0.019\pm0.006$, $a_1=0.002\pm0.001$, and $a_2=-1.149\times10^{-4}\pm4.850\times10^{-4}$ with $R^2\approx0.878$. As a result, from Eq. (2), it is therefore possible to write the scaling area

$$\frac{\langle A\rangle - F(\sigma)}{G(\sigma)} = f^{-0.25}E_0, \tag{3}$$

and by plotting this scaling area $(\langle A\rangle - F(\sigma))/G(\sigma)$ against $f^{-0.25}E_0$ all the data should collapse onto a single linear line having a y intercept at zero. The data collapsing of the scaling area from all f, E_0, and σ was found to confirm Eq. (3) as evident in Fig. 3.

On the other hand, it is of interest if the scaling of $\langle A\rangle$ in a form given by Eq. (1) is allowed. Therefore, by discarding minor loops which usually occur at very low E_0, $F(\sigma)\equiv\langle A\rangle(E_0\to0)$ will be small in comparing to $\langle A\rangle$ and can be discarded in Eq. (3) at some intermediately high fields.[12] Consequently, $\langle A\rangle\propto(a+b\sigma^c)f^{-0.25}E_0$ may be written and by substituting the fitted parameters, it is found that

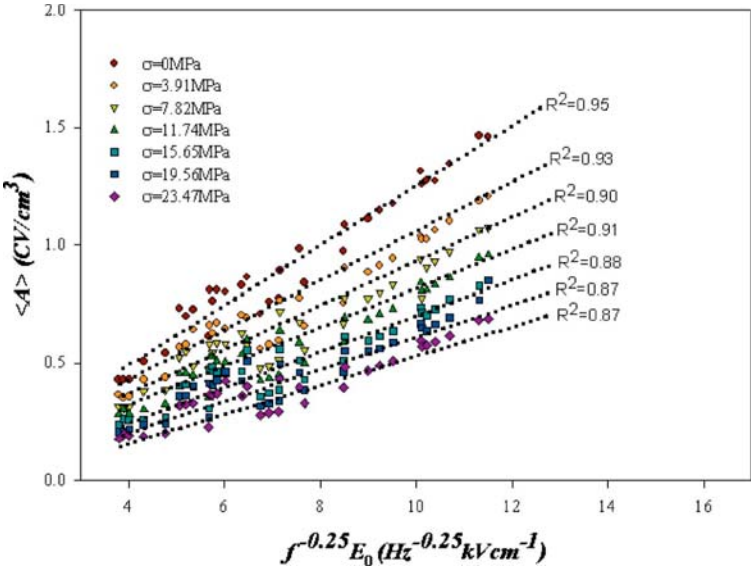

FIG. 2. (Color online) Scaling of hysteresis area $\langle A\rangle$ against $f^{-0.25}E_0$ for soft PZT ceramic at various σ.

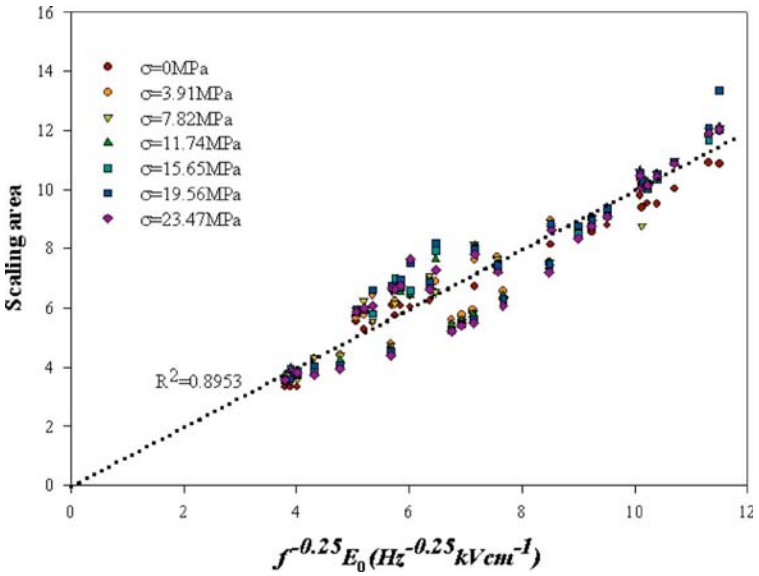

FIG. 3. (Color online) The collapse of the scaling area $(\langle A\rangle - F(\sigma))/(\sigma)$ against $f^{-0.25}E_0$ on a same linear line (with small fluctuation) for soft PZT ceramic.

$$\langle A\rangle - \langle A_{\sigma=0}\rangle = \langle A - A_{\sigma=0}\rangle \propto f^{-0.25}E_0\sigma^{0.44}, \tag{4}$$

where $\langle A_{\sigma=0}\rangle$ refers to the stress-free hysteresis area which will be a dominant term for zero stress. Note that from the appearance of stress σ, $\langle A - A_{\sigma=0}\rangle$, referring to the difference in energy dissipation between under stress and stress-free conditions, increases with increasing stress suggesting a decay of $\langle A\rangle$ with σ at a rate of $\sigma^{0.44}$ as observed in experiments. As a result, it can be concluded that the difference of the hysteresis area between under stress and stress-free conditions scales with frequency, field amplitude, and stress via exponents $m=-0.25$, $n=1$, and $p=0.44$. However, at a particular fixed stress, Eq. (4) gives $f^{-0.25}E_0$ which is the original form for how the area scales with the frequency and the field amplitude.[12]

To understand the scaling relation obtained, at least qualitatively, one needs to consider the following statements. Since the *P-E* loop area indicates the polarization dissipation energy subjected to one full cycle of electric field application, the loop area is therefore directly related to volume involved in the switching process during the application of electric field.[17–19] Hence, when the mechanical stress is applied, more and more ferroelectric domains are constrained by the applied stress and cannot be reoriented by the electric field so as to participate in the polarization reversal. Consequently, both the saturation and remnant polarizations become lower with increasing the compressive stress. The polarization dissipation energy is consequently found to decrease with increasing the applied stress, indicating that the sample volume contributing to polarization reversal decreases with the increasing stress. Similar observations have also been reported in other investigations.[14–18,20–22]

In summary, the scaling behavior of the dynamic hysteresis of the soft PZT bulk ceramics under the effect of mechanical stress has been investigated. With the presence of the external stress, the scaling law for the loop area yields the same set of exponents to frequency and field amplitude in stress-free condition which confirms the condition of universality in bulk system. Furthermore, the difference of the energy dissipation between the under stress and stress-free conditions is found to scale with $f^{-0.25}E_0\sigma^{0.44}$. As a result, the study provides a detailed understanding of how the energy dissipation of the hysteresis properties behaves in response to various conditions especially the mechanical stress.

Financial supports from the Thailand Research Fund (TRF), Commission on Higher Education (CHE), and Faculty of Science and Graduate School of Chiang Mai University are gratefully acknowledged.

[1] K. Uchino, *Ferroelectric Devices* (Dekker, New York, 2000), p. 145.
[2] O. Auciello, J. F. Scott, and R. Ramesh, Phys. Today **51**(7), 22 (1998).
[3] M. Rao, H. R. Krishnamurthy, and R. Pandit, Phys. Rev. B **42**, 856 (1990).
[4] M. Acharyya and B. K. Chakrabarti, Phys. Rev. B **52**, 6560 (1995).
[5] J.-M. Liu, H. L. W. Chan, C. L. Choy, Y. Y. Zhu, S. N. Zhu, Z. G. Liu, and N. B. Ming, Appl. Phys. Lett. **79**, 236 (2001).
[6] M. Rao and R. Pandit, Phys. Rev. B **43**, 3373 (1991).
[7] J.-M. Liu, H. L. W. Chan, C. L. Choy, and C. K. Ong, Phys. Rev. B **65**, 014416 (2001).
[8] Q. Jiang, H. N. Yang, and G. C. Wang, Phys. Rev. B **52**, 14911 (1995).
[9] B. Pan, H. Yu, D. Wu, X. H. Zhou, and J.-M. Liu, Appl. Phys. Lett. **83**, 1406 (2003).
[10] Y.-H. Kim and J.-J. Kim, Phys. Rev. B **55**, R11933 (1997).
[11] J.-H. Park, C.-S. Kim, B.-C. Choi, B. K. Moon, J. H. Jeong, and I. W. Kim, Appl. Phys. Lett. **83**, 536 (2003).
[12] R. Yimnirun, Y. Laosiritaworn, S. Wongsaenmai, and S. Ananta, Appl. Phys. Lett. **89**, 162901 (2006).
[13] K. Uchino, *Piezoelectric Actuators and Ultrasonic Motors* (Kluwer Academic, Boston, 1997), p. 129.
[14] J. Zhao, A. E. Glazounov, and Q. M. Zhang, Appl. Phys. Lett. **74**, 436 (1999).
[15] D. Viehland and J. Powers, J. Appl. Phys. **89**, 1820 (2001).
[16] D. Zhou, M. Kamlah, and D. Munz, J. Eur. Ceram. Soc. **25**, 425 (2005).
[17] R. Yimnirun, Y. Laosiritaworn, and S. Wongsaenmai, J. Phys. D **39**, 759 (2006).
[18] R. Yimnirun, S. Ananta, A. Ngamjarurojana, and S. Wongsaenmai, Appl. Phys. A: Mater. Sci. Process. **81**, 1227 (2005).
[19] M. E. Lines and A. M. Glass, *Principles and Applications of Ferroelectrics and Related Materials* (Clarendon, Oxford, 1977), p. 102.
[20] J. F. Shepard, Jr., F. Chu, B. Xu, and S. Trolier-McKinstry, Mater. Res. Soc. Symp. Proc. **493**, 81 (1997).
[21] T. Kumazawa, Y. Kumagai, H. Miura, M. Kitano, and K. Kushida, Appl. Phys. Lett. **72**, 608 (1998).
[22] X. Lu, J. Zhu, X. Li, Z. Zhang, X. Zhu, D. Wu, F. Yan, Y. Ding, and Y. Wang, Appl. Phys. Lett. **76**, 3103 (2000).

Appl. Phys. A 86, 249–255 (2007)
DOI: 10.1007/s00339-006-3753-3

Applied Physics A
Materials Science & Processing

R. WONGMANEERUNG
R. YIMNIRUN
S. ANANTA✉

Effects of sintering condition on phase formation, microstructure and dielectric properties of lead titanate ceramics

Department of Physics, Faculty of Science, Chiang Mai University, Chiang Mai 50200, Thailand

Received: 8 May 2006/Accepted: 4 October 2006
Published online: 17 November 2006 •

ABSTRACT Lead titanate ceramics have been prepared by two different processing methods: conventional (or single-stage) and two-stage sintering. Effects of designed sintering conditions on phase formation, densification, microstructure and dielectric properties of the ceramics were characterized via X-ray diffraction, Archimedes density measurement, scanning electron microscopy and dielectric measurement, respectively. The potentiality of a two-stage sintering technique as a simple ceramic fabrication method to obtain highly dense and pure lead titanate ceramics was demonstrated. It has been found that, under suitable two-stage sintering conditions, dense perovskite lead titanate ceramics can be successfully achieved with better dielectric properties than those of ceramics from a single-stage sintering technique.

PACS 77.22.-d; 77.84.-s; 77.84.Dy

1 Introduction

Being one of the lead-based perovskites, lead titanate ($PbTiO_3$ or PT) is of interest as a component in commercial electroceramic materials. In addition, PT when combined with other oxides can form a series of ferroelectric materials that exhibit many of the most desirable dielectric, piezoelectric and pyroelectric properties for use in electronic devices at high frequency and high temperature, such as infrared sensors, microactuators, capacitors and hydrophones [1–3]. The most important properties of perovskite PT ceramics are high Curie temperature ($\sim 490\,^{\circ}C$) and large mechanical-quality factor and pyroelectric coefficient [4, 5]. However, pure and dense PT ceramics are regarded to be one of the most difficult lead-based perovskite ferroelectric ceramics to produce [6]. PT ceramic is mechanically weak due to large distortion of the tetragonal phase at room temperature, which is characterized by the ratio between the lattice parameters (c/a, hereafter called tetragonality, ~ 1.06 [6, 7]). Apart from general problems of PbO volatilization and associated high porosity, the stress induced by cooling through the phase transition can create cracking in bulk ceramics. In addition, it is difficult to pole the ceramics with low resistivity (10^7–$10^8\ \Omega$ cm) [8].

✉ Fax: (6653) 943-445, E-mail: suponananta@yahoo.com

To overcome these problems, several techniques have been introduced, such as utilizing ultra-fine powders, using additives, employing spark-plasma sintering and carrying out appropriate milling and sintering conditions [8–13]. All these techniques are aimed at reducing the lattice tetragonality of the bulk ceramics, even though they inevitably affect the phase formation, structure and electrical properties of materials in different ways. Amongst all the approaches reported so far, most attention has been concentrated on the use of additives and powder processing, whereas investigations of modified sintering techniques have not been widely carried out [13, 14].

Therefore, in this work, a two-stage sintering method has been developed to resolve these problems. With this new scheme, instead of using a single, high firing temperature (of up to 1225 °C) [13] where the degree of PbO volatilization affects the stoichiometry of the product by forming a pyrochlore phase, in addition to a perovskite phase, two moderate temperatures (T_1 and T_2 with a constant dwell time of 2 h at each stage) were adopted. The aim of this study was to investigate the influence of these two ceramic processing methods (single- and two-stage sintering) on phase formation, densification, microstructure and dielectric properties of $PbTiO_3$ ceramics.

2 Materials and methods

Commercially available powders of PbO and TiO_2 (anatase form, Fluka, $> 99\%$ purity) were used as starting materials. A simple mixed oxide synthetic route was employed to synthesize $PbTiO_3$ powders. The mixing process was carried out by ball milling a mixture of raw materials for 24 h with corundum medium in isopropyl alcohol (IPA). After wet milling, the slurry was dried at 120 °C for 2 h, sieved and calcined in a closed alumina crucible, with the optimum calcination conditions determined by the X-ray diffraction (XRD) method (600 °C for 2 h with heating/cooling rates of 5 °C/min [15]). Ceramic fabrication was achieved by adding 3 wt % polyvinyl alcohol (PVA) binder, prior to pressing as pellets (15 mm in diameter and 1.0–1.3-mm thick) in a pseudo-uniaxial die press at 100 MPa. Each pellet was placed in an alumina crucible together with an atmosphere powder ($PbTiO_3$) of identical chemical composition. After the binder burn out at 500 °C for 1 h, sintering was carried out with a dwell time of 2 h at each step, with constant

heating/cooling rates of 1 °C/min [13] applied (Fig. 1). Variation of the firing temperature between 1150 and 1250 °C was carried out for the single-stage sintering samples. Three sets of the first sintering temperature (T_1) were assigned for the two-stage sintering case: 700, 800 and 900 °C. Variation of the second sintering temperature (T_2) between 1000 °C and 1250 °C was carried out for each case.

Densities of the final sintered products were determined by using the Archimedes principle. Sintered ceramics were examined by room-temperature X-ray diffraction (Siemens D500 diffractometer) using Cu K_α radiation to identify the phase formed. The lattice parameters and tetragonality factor (c/a) of the sintered ceramics were calculated from the XRD patterns [16]. The microstructural development was characterized using a JEOL JSM-840A scanning electron microscopy (SEM), equipped with an energy-dispersive X-ray (EDX) analyser. Mean grain sizes of the sintered ceramics were subsequently estimated by employing the linear intercept method [17]. In order to evaluate the dielectric properties, dense ceramics were polished to form flat, parallel faces (14 mm in diameter and 0.8-mm thick). The samples were then coated with silver-paste electrodes which were fired on both sides of the samples at 700 °C for 1 h. The dielectric properties were measured at a frequency of 1 MHz using a HIOKI 3532-50 LCR meter, on cooling through the transition range (500–25 °C) with a rate of 5 °C/min.

3 Results and discussion

X-ray diffraction patterns of the PT ceramics sintered at various conditions are displayed in Figs. 2 and 3, indicating the formation of both perovskite and impurity phases in each case. The strongest reflections in the majority of all XRD traces indicate the formation of the $PbTiO_3$ perovskite phase of lead titanate, which could be matched with JCPDS file no. 6-452, in agreement with other works [11–13]. To a first approximation, this major phase has a tetragonal perovskite-type structure in space group P4/mmm (no. 123) with cell parameters $a = 389.93$ pm and $c = 415.32$ pm [18]. For the singly sintered PT ceramics, additional weak reflections are found in the samples sintered above 1175 °C (marked by θ in Fig. 2), which correlate to the starting precursor PbO (JCPDS file no. 77-1971) [19]. This observation could be attributed mainly to the poor mixing of the employed powders derived from the ball-milling technique. The relative amounts of perovskite and minor phase present in each sintered ceramic were calculated from the intensities of the major X-ray reflections from the respective phases. In this connection, the following approximation was adopted, as in the earlier PMN ($Pb(Mg_{1/3}Nb_{2/3})O_3$) and PFN ($Pb(Fe_{1/2}Nb_{1/2})O_3$) studies [14]:

$$\text{perovskite phase (wt\%)} = I_P/(I_P + I_M) \times 100\,. \qquad (1)$$

Here I_P and I_M refer to the intensities of the {110} perovskite and {111} minor phase peaks, respectively, these being the most intense reflections in the XRD patterns of both phases. For the purposes of estimating the concentration of minor phase present, (1) has been applied to the diffraction patterns obtained (numerical data are presented in Tables 1 and 2).

More interestingly, a single phase of perovskite PT is found in all the doubly sintered samples (Fig. 3), in contrast to the observations for the singly sintered samples. No evidence of pyrochlore phase of $PbTi_3O_7$ composition earlier reported by Udomporn, Ananta and Tartaj et al. [15, 20] was found, nor was there any evidence of other second phases [21] being present. This could be due to the lower firing temperature of the doubly sintered samples as compared to the singly sintered ceramics, leading to a smaller degree of lead losses and consequently avoiding the pyrochlore formation, while a sufficient amount of energy required for ceramic densification still to be reached was provided by the longer holding time, in agreement with other works [14, 22, 23]. However, many other factors come into play, e.g. homogeneity of materials, reactivity of starting powders and processing variables. These XRD results clearly show that, in general, the different processing methods used for preparing PT ceramics gave rise to a different phase formation in the sintered materials. The absence of minor phase in doubly sintered samples was related to the more reactive process used [14].

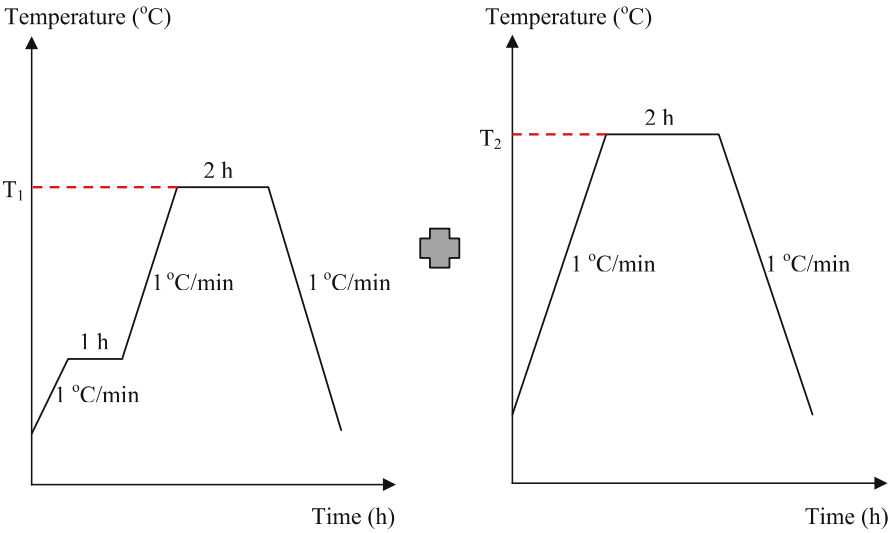

FIGURE 1 A two-stage method sintering profile

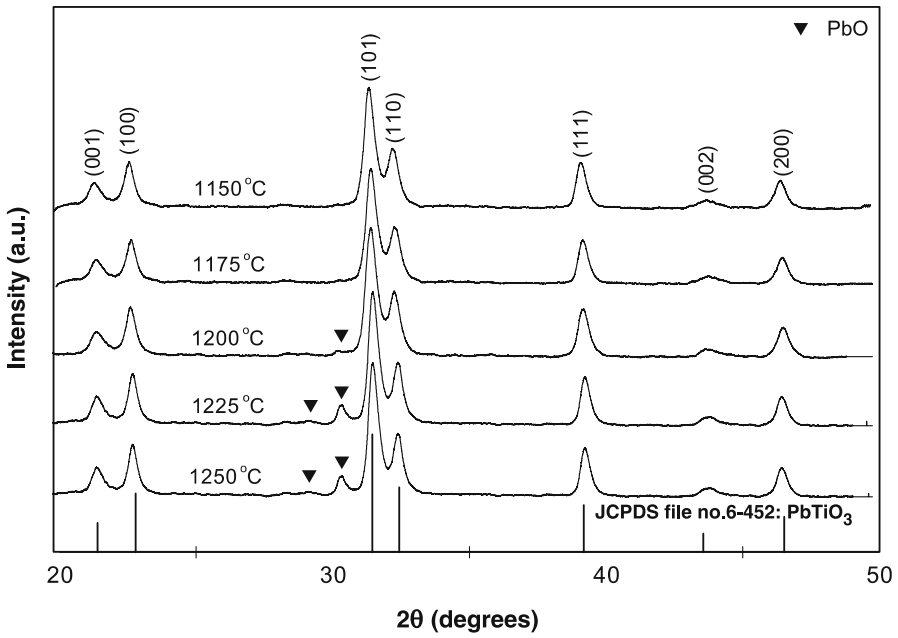

FIGURE 2 XRD patterns of PT ceramics singly sintered at various temperatures

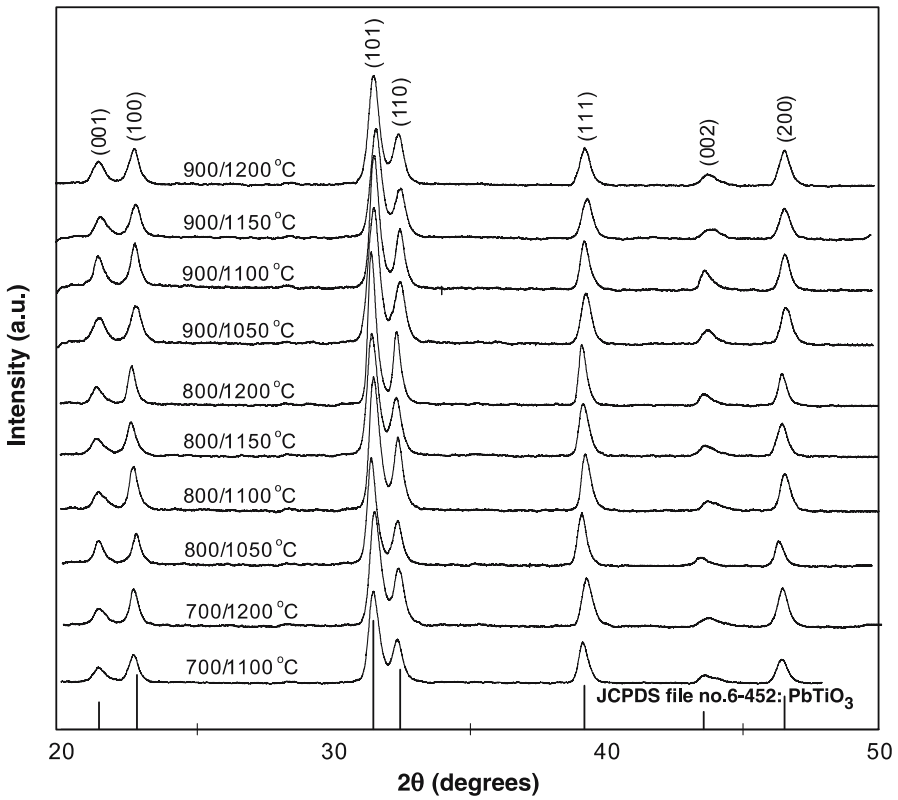

FIGURE 3 XRD patterns of PT ceramics doubly sintered at various conditions, with the first sintering temperature (T_1) at 700, 800 and 900 °C

Tables 1 and 2 also present the tetragonality factor (c/a), relative density and average grain size of singly and doubly sintered samples, respectively. Generally, it is evident that as the sintering temperature increases, the density of almost all the samples increases. However, it can be seen that the sintering behaviour of singly and doubly sintered PT ceramics was dissimilar. Doubly sintered ceramics reached a maximum density of $\sim 97\%$ at 900/1150 °C or 900/1200 °C. On the other hand, singly sintered samples exhibit less densification, and a temperature of 1225 °C was required to reach a densification level of $\sim 94\%$. The densification of all materials slightly decreased at temperatures higher than those of the maximum density, accompanied by a significant increase of weight loss ($\sim 2\%$–5%). By comparison with singly sintered PT ceramics, lower values of tetragonality (c/a) are found in all doubly sintered cases, indicating lower internal stress in these sintered samples.

Microstructural features of PT samples singly sintered at different temperatures for 2 h with heating/cooling rates of 1 °C/min are shown in Fig. 4. It was found that the samples